Kaon to Two Pion decay from Lattice QCD and CP violation

Daiqian Zhang

Submitted in partial fulfillment of the

requirements for the degree of

Doctor of Philosophy

in the Graduate School of Arts and Sciences

COLUMBIA UNIVERSITY

2015

Abstract

Kaon to Two Pion decay from Lattice QCD and CP violation

Daiqian Zhang

We report a direct lattice calculation of the K to $\pi\pi$ ($\Delta I = 1/2$) decay amplitude A_0 on a $32^3 \times 64$ ensemble, with 2+1 flavor Möbius Domain Wall Fermion, with $a^{-1} = 1.379(9)$ GeV. This is a complete and physical calculation: chiral symmetry breaking is controlled by the Möbius Domain Wall formalism; pion and kaon masses are simulated at their near-physical values, $m_K \approx 490$ MeV and $m_\pi \approx 140$ MeV. G-parity boundary conditions are used to realize correct kinematics for the final two-pion state and give $E_{\pi\pi(I=0)} \approx 498$ MeV, while keeping isospin symmetry; all 10 $\Delta S = 1$ operators are considered, each of which involve the notorious disconnected diagrams. With this setup, we are able to resolve, for the first time, the physical decay amplitudes $\mathrm{Re}(A_0)$ and $\mathrm{Im}(A_0)$ from 0. The $\mathrm{Re}(A_0)$ amplitude agrees with its experimental value, The result for $\mathrm{Im}(A_0)$ is used, in combination with the lattice calculated decay amplitude A_2, to compute $\mathrm{Re}(\epsilon'/\epsilon)$, which evaluates to $1.38(5.08) \times 10^{-4}$ and agrees at the 2σ level with the experimental value $1.66(0.23) \times 10^{-3}$. This is a major step towards understanding and testing CP violation in the standard model.

Several measurement techniques are used to increase computational efficiency. We use all-to-all propagators to construct finite sized mesons, which have a better overlap with the meson ground state and reducing statistical noise from the vacuum graphs. This also saves matrix-inversion overhead when constructing mesons with different momenta. The other technical improvements include the mixed-precision conjugate gradient algorithm, and optimized fast Fourier transformation. We also discuss the cross-checks on the use of G-parity boundary conditions, and estimate several important systematic errors.

Contents

List of Tables

List of Figures

ACKNOWLEDGMENTS

I would like to thank my advisor Prof. Norman Christ for his support and guidance through out this whole project. Without his crucial suggestions at many points, the project will be much more difficult, if not impossible, to finish.

I would also thank Prof. Robert Mawhinney for helpful discussions. I am very grateful to Chris Kelly for his work and enjoyed collaborating with him a lot.

I enjoyed and benefited from working with all my colleagues: Ziyuan Bai, Tom Blum, Peter Boyle, Xu Feng, Taku Izubuchi, Luchang Jin, Chulwoo Jung, Christoph Lehner, Zhongjie Lin, Qi Liu, Chris Sachrajda, Amarjit Soni, Akira Ukawa, Hantao Yin, Jianglei Yu.

Finally, I thank my family for their constant support; and my wife, Xiaoqian Gui, for her encouragement and caring about my thesis project during all these years.

Chapter 1

Introduction

Since the experimental discovery of Parity violation in 1956 and Charge-Parity (CP) violation in 1964, considerable progress has been made to understand the discrete symmetry breaking in nature. It's widely believed that the weak interaction in the standard model is the source of this discrete symmetry breaking. However an important quantity providing a measure of CP violation, $\mathrm{Re}(\epsilon'/\epsilon)$, is not directly accessible from theory, due to the non-perturbative nature of strong interaction. The quantity $\mathrm{Re}(\epsilon'/\epsilon)$ is small ($\approx 10^{-3}$) and highly sensitive to mechanisms that go beyond the standard model. In an effort to test the standard model, we make the first theoretical calculation of $\mathrm{Re}(\epsilon'/\epsilon)$ in this work, using the technique of lattice QCD to solve the problem raised by the non-perturbative strong interaction.

In particle physics, the standard model is now an accepted and experimentally well-tested theory, which uses quantum gauge theory to explain the interactions among subatomic particles. The discovery of $W^{\pm}$ and Z boson (1983), top quark (1995), and Higgs boson [3] (2012) show the great success of this theory in particle physics.

The gauge group in the standard model is U(1)×SU(2)×SU(3). Due to the Higgs mechanism, the U(1)×SU(2) part is spontaneous broken to a U(1) subgroup that is the basis of quantum electrodynamics (QED), while three massive bosons carry weak interaction. The remaining SU(3) group provides the strong interactions, described as quantum chromody-

namics (QCD). The interactions in QED are relatively easily calculated using perturbation theory and give many of the most accurate predictions of the standard model, for example the anomalous magnetic moment of electron agrees with experimental to 1 part in 10^{10}. QCD is an UV complete theory, the interaction (also known as strong interaction) becomes weaker at higher energy scales, which is the feature of a non-abelian gauge group; but on the low energy end, it's difficult to do analytic calculation because the coupling constant α_s is of order 1 and perturbation theory fails. Alternatively, lattice QCD provides the only known non-perturbative approach to solve QCD. As for the weak interaction, it is the least understood part in the standard model. The weak interaction contains most of the 19 adjustable parameters in the standard model, and it explicitly breaks parity symmetry since only left-handed fermions couple to weak isospin. The weak interaction breaks CP symmetry explicitly by the complex phase in CKM matrix.

Symmetry has always played an important role in theoretical physics, for example we often use it to distinguish states in quantum mechanics. The discovery of parity violation is motivated by the $\theta - \tau$ puzzle, in which two parity-different decay modes are found for two "identical" particles, raising the question of whether parity is truly a perfect symmetry. The experiment by Wu at the end of 1956 showed the violation of parity conservation in the beta decay of cobalt-60 [4], leading to the Nobel prize in 1957 (won by Lee and Yang). Later, the discovery of CP violation in neutral kaon decay became another milestone in particle physics and won the Nobel prize in 1980 [5]. Knowledge of the discrete symmetry breaking will help us understand fundamental questions about the universe, for example what's the nature of space and chiral (handed) objects, why do particles dominate over anti-particle?

Since CP violation is observed and quantitatively measured in experiment, one natural question is whether the standard model can predict it. A CP violating process typically involves a hadronic decay, in which both the weak and strong interaction contribute. The weak interaction, although it arises from a non-abelian gauge coupling, can be calculated

using perturbation theory. This is because the Higgs mechanism occurs at such a high energy scale that weak force carriers ($W^{\pm}$,Z boson) acquire much larger masses than the confinement scale of weak interaction, as a result the coupling constant is never strong enough to invalidate perturbation theory. As for the low energy QCD part, we'll use the only known non-perturbative treatment, lattice QCD.

As a standard procedure to combine weak interaction and strong interaction in hadronic decay, we first set an energy scale μ to split the high energy part ($> \mu$) and low energy part ($< \mu$). The low energy part appears as an effective theory with effective vertices and the corresponding renormalized coupling constants (also known as Wilson coefficients), it's put into lattice QCD and its interplay with the quarks and gluons is treated non-perturbatively. The effects of the high energy part are calculated by integrating out the heavy degrees of freedom, during which the propagators of those fields are approximated to a point, generating a collection of local operator products (which can be analysed by using the Operator Product Expansion, OPE). The OPE analysis ends up with effective vertices and their renormalized coupling constants that define the low energy part mentioned earlier.

In this work, we mainly study the CP-violating $K \to \pi\pi$ decay process. The goal is to calculate, from first principles and at the physical point, the $K \to \pi\pi$(I=0) decay amplitude A_0, and the real part of the ratio of CP-violating quantity $\mathrm{Re}(\epsilon'/\epsilon)$. We treat the $W^{\pm}$ and Z bosons and the top/bottom/charm quarks perturbatively and integrate them out; the up/down/strange quarks are simulated on lattice. In order to control chiral symmetry breaking in the lattice calculation and maintain the continuum operator mixing pattern, we use the Domain Wall Fermion (DWF) action which exponentially suppresses residual chiral symmetry breaking by introducing an extra 5th dimension. The DWF parameters are tuned to give physical pion and kaon masses. The newly developed G-parity boundary condition technique is used to force that pions carry physical relative momenta present in the actual $\pi\pi$ final state. Both DWF and G-parity boundary conditions introduce extra computational

cost, but it's still small compared to the huge advantage of simulating the kaon decay at physical point for the first time. Another challenge besides the physical point calculation is the disconnected graphs in $K \to \pi\pi(\mathrm{I}{=}0)$, which arises because of the non-zero coupling between the $\pi\pi(\mathrm{I}{=}0)$ and the vacuum and which degrades the signal badly. To reduce the fluctuations from the vacuum graphs, we have used the all-to-all propagators to construct pions with a more realistic size to avoid unnecessary coupling with vacuum.

While we don't consider several systematic errors in this work (e.g. finite volume, finite lattice spacing, and so on), because of the current large statistical error, we should begin to consider them to further sharpen the calculation as the available statistics increases and technology keeps advancing.

We organize this work as follows. In Chapter 2, we review the kaon decay in the standard model and the related measurement from experiments. In Chapter 3 we give an overview of the lattice QCD method and summarize the procedure of the lattice calculation of the kaon decay amplitude. In Chapter 4 we explain the measurement techniques used in this work, including G-parity boundary conditions and all-to-all propagators. In Chapter 5 and 6 we present the measurement results from several $16^3 \times 32$ ensembles and a $32^3 \times 64$ ensemble. In Chapter 7, we summarize our result and discuss possible improvements in the future.

Chapter 2

CP Violation in the Standard Model

In this Chapter we discuss the origin and measure of CP violation in neutral kaon decay, within the framework of the standard model. We will explain kaon mixing, which contributes most of the CP violation; then we work out the formulas for the two measures of CP violation; lastly we calculate the experimental indication for kaon decay amplitude from kaon branching ratio and lifetime, which are ingredients (but not all) of the CP violation measures and our lattice results could compare with.

2.1 CKM Matrix

In the standard model, the mixing between quark generations manifest itself in the quark charged weak currents:

$$\mathcal{L}_{int} = -\frac{g_2}{8}(W^+_\mu J^\mu_{\rm ch} + W^-_\mu J^{\mu\dagger}_{\rm ch}), \tag{2.1}$$

where g_2 is the weak coupling constant, $W^{\pm}$ are the fields that represent the $W^{\pm}$ bosons, and J^{μ}_{ch} is the quark charged weak current:

$$J^{\mu}_{\text{ch}} = 2(\ \bar{u}_L \quad \bar{c}_L \quad \bar{t}_L\ )\gamma^{\mu} V^{\text{CKM}} \begin{pmatrix} d_L \\ s_L \\ b_L \end{pmatrix} \tag{2.2}$$

$$V^{\text{CKM}} = \begin{pmatrix} V_{ud} & V_{us} & V_{ub} \\ V_{cd} & V_{cs} & V_{cb} \\ V_{td} & V_{ts} & V_{tb} \end{pmatrix}. \tag{2.3}$$

The CKM matrix V^{CKM} arises from transforming the quark fields from gauge eigenstates to mass eigenstates (more details are provided in Chapter II of [6]), and by definition it's a unitary matrix. An $n \times n$ unitary matrix contains $n(n-1)/2$ angle parameters and $n(n+1)/2$ phase parameters. For those phase parameters, some of them can be absorbed into the phases of the quark fields, for example the quark rephasing of

$$q_L \to e^{i\theta^q} q_L,\ \ (q \in \{u, d, c, s, t, b\}) \tag{2.4}$$

will have the effect of changing the CKM matrix:

$$V^{\text{CKM}}_{\alpha\beta} \to V^{\text{CKM}}_{\alpha\beta} e^{i(\theta^{\beta} - \theta^{\alpha})},\ \ (\alpha \in \{u, c, t\}, \beta \in \{d, s, b\}). \tag{2.5}$$

Since an overall common shift in θ^q does not affect V^{CKM}, only $(2n-1)$ transformations are effective in Equation 2.4, as a result there are only $n(n+1)/2 - (2n-1) = (n-1)(n-2)/2$ phases in V^{CKM}. These phases are the sources of CP-violation since they make the quark gauge coupling complex, and they are only present in theories with at least three generations of quarks ($n \geq 3$).

2.2 Kaon Mixing

The K^0 and $\overline{K}^0$ are related by CP transformation:

$$\mathrm{CP}|K^0\rangle = -|\overline{K}^0\rangle \tag{2.6}$$

$$\mathrm{CP}|\overline{K}^0\rangle = -|K^0\rangle \tag{2.7}$$

From these the CP eigenstates are:

$$|K^0_+\rangle = \frac{1}{\sqrt{2}}(|K^0\rangle - |\overline{K}^0\rangle) \tag{2.8}$$

$$|K^0_-\rangle = \frac{1}{\sqrt{2}}(|K^0\rangle + |\overline{K}^0\rangle), \tag{2.9}$$

where $|K^0_+\rangle$ is CP even and $|K^0_-\rangle$ is CP odd.

In experiment, the two observed neutral kaons are called K_L and K_S, the first one has much longer lifetime than the latter. Since CP violation is rather mild, K_L and K_S are both close to but not exact CP eigenstates. K_L is almost the CP odd state K^0_- as it mostly decays into $\pi\pi\pi$, K_S is almost the CP even state K^0_+ as it mostly decays into $\pi\pi$. Because the mass of three pion is so close to the kaon mass, the phase space for the final 3-pion is very limited in the $K_L \to \pi\pi\pi$ decay, as a result K_L has much longer lifetime than K_S.

From a phenomenological point of view, kaon mixing is described by the mixing matrix:

$$i\frac{d}{dt}\begin{pmatrix} K^0(t) \\ \overline{K}^0(t) \end{pmatrix} = \left(M - \frac{i}{2}\Gamma\right)\begin{pmatrix} K^0(t) \\ \overline{K}^0(t) \end{pmatrix} \tag{2.10}$$

where M and Γ are each a 2×2 Hermitian matrix. The imaginary $\frac{i}{2}\Gamma$ accounts for the decay

process of kaon. To second order in perturbation theory, M and Γ are:

$$M_{ij} = m_K^{(0)}\delta_{ij} + \frac{\langle i|H_W|j\rangle}{2m_K} + P\sum_n \frac{\langle i|H_W|n\rangle\langle n|H_W|j\rangle}{m_K - E_n} \tag{2.11}$$

$$\Gamma_{ij} = \frac{1}{2m_K}\sum_n \langle i|H_W|n\rangle\langle n|H_W|j\rangle 2\pi\delta(E_n - m_K) \tag{2.12}$$

CPT symmetry requires that $M_{11} = M_{22}$ and $\Gamma_{11} = \Gamma_{22}$, so the mixing matrix can be written as:

$$M - \frac{i}{2}\Gamma = \begin{pmatrix} A & p^2 \\ q^2 & A \end{pmatrix}, \tag{2.13}$$

where A, q^2, and p^2 can be complex. Diagonalizing the mixing matrix, we find:

$$|K_L\rangle = \frac{1}{\sqrt{1+|\bar{\epsilon}|^2}}\left(|K_-^0\rangle + \bar{\epsilon}|K_+^0\rangle\right) \tag{2.14a}$$

$$|K_S\rangle = \frac{1}{\sqrt{1+|\bar{\epsilon}|^2}}\left(|K_+^0\rangle + \bar{\epsilon}|K_-^0\rangle\right), \tag{2.14b}$$

where

$$\bar{\epsilon} = \frac{p-q}{p+q} \approx \frac{i}{2}\cdot\frac{\mathrm{Im}M_{12} - i\mathrm{Im}\Gamma_{12}/2}{\mathrm{Re}M_{12} - i\mathrm{Re}\Gamma_{12}/2} \tag{2.15}$$

The CP-violating $K_L \to \pi\pi$ decay receives contribution from two sources:

- The K_L contains a little K_+^0, which happily decays into $\pi\pi$. This is due to kaon mixing and is called indirect CP-violation.
- The major K_-^0 part in K_L can by itself decay into $\pi\pi$, this is called direct CP-violation.

In the next section, we will derive formulas describing each of the measures of these two sources of CP-violation.

2.3 Measures of CP Violation in Kaon Decay

The measures of indirect and direct CP-violation in $K_L \to \pi\pi$ are called ϵ and ϵ' respectively, they are defined in terms of the ratio of kaon decay amplitudes:

$$\frac{\langle \pi^+\pi^-|H_W|K^L\rangle}{\langle \pi^+\pi^-|H_W|K^S\rangle} \equiv \eta_{+-} \equiv \quad \epsilon + \epsilon' \tag{2.16a}$$

$$\frac{\langle \pi^0\pi^0|H_W|K^L\rangle}{\langle \pi^0\pi^0|H_W|K^S\rangle} \equiv \eta_{00} \equiv \quad \epsilon - 2\epsilon' \tag{2.16b}$$

ϵ is the contribution to $\eta_{+-/00}$ due to kaon mixing, while ϵ' is the contribution to $\eta_{+-/00}$ due to direct CP-violation. As can be seen from Equation 2.16, ϵ' will vanish if there is no direct CP-violation.

To derive the formulas for ϵ and ϵ', we define the quantity A_I as:

$$\langle \pi\pi(I)|H_W|K^0\rangle = \sqrt{2}A_I e^{i\delta_I} = (\sqrt{2}|A_I|e^{i\xi_I})e^{i\delta_I} \tag{2.17a}$$

$$\langle \pi\pi(I)|H_W|\overline{K}^0\rangle = -\sqrt{2}A_I^* e^{i\delta_I} = -(\sqrt{2}|A_I|e^{-i\xi_I})e^{i\delta_I} \tag{2.17b}$$

for $I = 0, 2$. The second equation above is simply the CPT transformation of the first one. If CP is an exact symmetry of H_W, A_I will be real number. The quantity δ_I are the pion-pion scattering phase shifts for $\pi\pi$ scattering in the $I = 0$ and 2 states. The quantity ξ_I are the complex phases of A_I which is also known as CP-violating phases since they will be zero if CP is an exact good symmetry [7]. The $|\pi\pi(I)\rangle$ are isospin eigenstates, in terms of which the more physical $\pi^+\pi^-$ and $\pi^0\pi^0$ states can be decomposed:

$$|\pi^+\pi^-\rangle = \frac{1}{\sqrt{3}}\Big(|\pi\pi(I=2)\rangle + \sqrt{2}|\pi\pi(I=0)\rangle\Big) \tag{2.18a}$$

$$|\pi^0\pi^0\rangle = \frac{1}{\sqrt{3}}\Big(-\sqrt{2}|\pi\pi(I=2)\rangle + |\pi\pi(I=0)\rangle\Big). \tag{2.18b}$$

Substituting Equations 2.17, 2.18, and 2.14 into 2.16, neglecting higher order terms in CP-

violating phase ξ_I and the ratio $\mathrm{Re}(A_2)/\mathrm{Re}(A_0)$, we can solve for ϵ and ϵ' with the result:

$$\epsilon = \bar{\epsilon} + i\xi_0 \tag{2.19a}$$

$$\epsilon' = \frac{ie^{i(\delta_2-\delta_0)}}{\sqrt{2}}\left|\frac{A_2}{A_0}\right|\left(\frac{\mathrm{Im}A_2}{\mathrm{Re}A_2} - \frac{\mathrm{Im}A_0}{\mathrm{Re}A_0}\right) \tag{2.19b}$$

The main object of this work is to test whether the standard model can quantitatively predict the experimental CP-violation quantity $\mathrm{Re}(\epsilon'/\epsilon) = (1.66 \pm 0.23) \times 10^{-3}$.

2.4 Kaon Decay from Experiment

The kaon decay amplitudes $A_{0,2}$ are important ingredients of ϵ and ϵ', we explain in this section how they are calculated from experimental data.

The general decay rate of an unstable particle into two particles is given by:

$$\Gamma = \iint_{\vec{p_1},\vec{p_2}} \frac{S|A(K \to \pi\pi)|^2}{2M}(2\pi)^4\delta^4(P - \sum_{i=1}^{2} p_i)\prod_{i=1}^{2}\frac{d^3p_i}{(2\pi)^3 2E_i}, \tag{2.20}$$

where

- A is the decay matrix element from quantum mechanics.
- S is the symmetry factor that accounts for the permutation symmetry of final two particles. S is 1 if the final two-particle state is unchanged under permutation of these two particles, otherwise S is 1/2. In the following derivation, I will use the convention that the $\pi\pi$ states are always symmetrized so that $S = 1/2$.
- M, P are the mass and four momentum of the initial particle.
- $E_i, \vec{p_i}$ are the energy and 3 momentum of particle i.

After integrating out the two-particle phase space,

$$\Gamma = \frac{1}{8\pi}\frac{1}{2}|A(K \to \pi\pi)|^2 \frac{|\vec{p_{1(2)}}|}{m_K^2}, \tag{2.21}$$

where $\vec{p_{1(2)}}$ is the 3 momentum of either of the final particle. This is also called Fermi's "golden rule". Applying this rule, the three kaon decay widths, corresponding to $K_s \to \pi^+\pi^-$, $K_s \to \pi^0\pi^0$, and $K^+ \to \pi^+\pi^0$, are given by:

$$\Gamma_{+-} = \frac{1}{8\pi}\frac{1}{2}|A_{+-}|^2 \frac{\sqrt{m_{K_s}^2/4 - m_{\pi^+}^2}}{m_{K^0}^2} \tag{2.22}$$

$$\Gamma_{00} = \frac{1}{8\pi}\frac{1}{2}|A_{00}|^2 \frac{\sqrt{m_{K_s}^2/4 - m_{\pi^0}^2}}{m_{K^0}^2} \tag{2.23}$$

$$\Gamma_{+0} = \frac{1}{8\pi}\frac{1}{2}|A_{+0}|^2 \frac{p_{+0}}{m_{K^+}^2}, \tag{2.24}$$

where

$$p_{+0} = \frac{\sqrt{(m_{K^+} - m_{\pi^+} - m_{\pi^0})(m_{K^+} + m_{\pi^+} + m_{\pi^0})(m_{K^+} - m_{\pi^+} + m_{\pi^0})(m_{K^+} + m_{\pi^+} - m_{\pi^0})}}{2m_{K^+}} \tag{2.25}$$

Using the experimental values given in Table A.2, the three decay amplitudes can be calculated:

$$\sqrt{\frac{1}{2}}|A_{+-}| = 3.92 \times 10^{-7} GeV \tag{2.26}$$

$$\sqrt{\frac{1}{2}}|A_{00}| = 2.59 \times 10^{-7} GeV \tag{2.27}$$

$$\sqrt{\frac{1}{2}}|A_{+0}| = 1.81 \times 10^{-8} GeV \tag{2.28}$$

Define A_0, A_2 to be (note there is now an overall factor of $\sqrt{2}$ difference from Equation 2.17,

this is the convention of our Collaborator and doesn't change the expression for ϵ and ϵ' in Equation 2.19):

$$\sqrt{2}A_0 e^{i\delta_0} = \langle \pi\pi(I=0, I_z=0)|H_w|K^0\rangle \quad (2.29)$$

$$\sqrt{2}A_2 e^{i\delta_2} = \langle \pi\pi(I=2, I_z=0)|H_w|K^0\rangle \quad (2.30)$$

A_0 and A_2 can then be derived from the previous three decay amplitudes:

$$\sqrt{2}A_2 e^{i\delta_2} = \sqrt{\frac{2}{3}}A_{+0} \quad (2.31)$$

$$\frac{1}{\sqrt{2}}A_{00} = \sqrt{\frac{1}{3}}(\sqrt{2}A_0 e^{i\delta_0}) - \sqrt{\frac{2}{3}}(\sqrt{2}A_2 e^{i\delta_2}) \quad (2.32)$$

$$\frac{1}{\sqrt{2}}A_{+-} = \sqrt{\frac{2}{3}}(\sqrt{2}A_0 e^{i\delta_0}) + \sqrt{\frac{1}{3}}(\sqrt{2}A_2 e^{i\delta_2}) \quad (2.33)$$

To check equation 2.31, note that A_{+0} and A_2 are related by isospin rotation on their initial and final states: A_{+0} is the decay amplitude from $K^+(I=\frac{1}{2}, I_z=\frac{1}{2})$ to $\pi\pi(I=2, I_z=1)$ through the weak Hamiltonian $H_W(I=\frac{2}{3}, I_z=\frac{1}{2})$. H_W has $I_z=\frac{1}{2}$ because of Wigner-Eckart theorem; also note that H_W contains 3 SU(2) isospin components (or u/d quarks) so it has $I=\frac{1}{2}$ or $I=\frac{3}{2}$, but only $I=\frac{3}{2}$ is allowed since the total I change from K^+ to $\pi\pi(I=2)$ is $\frac{3}{2}$. Then using Clebsch-Gordan coefficients:

$$\begin{aligned}\frac{\sqrt{2}A_2 e^{i\delta_2}}{A_{+0}} &= \frac{\langle \pi\pi(I=2, I_z=0)|H_w|K^0\rangle}{\langle \pi\pi(I=2, I_z=1)|H_w|K^+\rangle} \\ &= \frac{\langle I=2, I_z=0|I=\frac{3}{2}, I_z=\frac{1}{2}; I=\frac{1}{2}, I_z=\frac{-1}{2}\rangle}{\langle I=2, I_z=1|I=\frac{3}{2}, I_z=\frac{1}{2}; I=\frac{1}{2}, I_z=\frac{1}{2}\rangle} \\ &= \sqrt{\frac{2}{3}} \end{aligned} \quad (2.34)$$

Equation 2.32 and 2.33 are simply from decomposing the $\pi^0\pi^0(\pi^+\pi^-)$ state into different $\pi\pi$ isospin states. The factor $\frac{1}{\sqrt{2}}$ in front of A_{00} and A_{+-} is because the fact that $A_0(A_2)$

are the decay amplitudes for $|K^0\rangle$ while $A_{00}(A_{+-})$ are those for $|K_s\rangle(\approx \frac{1}{\sqrt{2}}(|K^0\rangle - |\overline{K^0}\rangle)$ and the $|K^0\rangle$ piece and $-|\overline{K^0}\rangle$ contributes almost the same amount due to CPT symmetry:

$$\begin{aligned}
\langle\pi\pi(I)|H_W|K_s\rangle &\approx \frac{1}{\sqrt{2}}\{\langle\pi\pi(I)|H_W|K^0\rangle - \{\langle\pi\pi(I)|H_W|\overline{K}^0\rangle\} \\
&= \{A_I + A_I^*\}e^{i\delta_I} \\
&\approx 2A_I e^{i\delta_I} \\
&\approx \sqrt{2}\langle\pi\pi(I)|H_W|K^0\rangle
\end{aligned} \tag{2.35}$$

Solving Equation 2.31, 2.32, and 2.33 for A_2, A_0, we get:

$$|A_2| = 1.479 \times 10^{-8}\text{GeV} \tag{2.36}$$

$$|A_0| = 3.320 \times 10^{-7}\text{GeV} \tag{2.37}$$

$$|\arg(A_0) - \arg(A_2)| = 44.56 \text{ degree} \tag{2.38}$$

These are the decay amplitudes result from basic experimental data, with which we can compare the lattice result. No error bars are included in the above numbers yet. Our most recent result for A_2 can be found in Ref. [8].

2.5 Effective $\Delta S = 1$ Hamiltonian

The standard model determination of ϵ' involves the $W^{\pm}$ boson and top quark, which are at a much higher energy scale than Lattice QCD could access. Their contribution are captured by the perturbative Wilson coefficients in a low energy effective theory:

$$H_W^{\Delta S=1} = \frac{G_F}{\sqrt{2}} V_{us}^* V_{ud} \sum_{i=1}^{10} C_i(\mu) Q_i(\mu), \tag{2.39}$$

where the superscript $\Delta S = 1$ means strangeness change of 1. G_F is the Fermi constant. $V_{q'q}$ is the Cabbibo-Kobayashi-Maskawa matrix element. $C_i(\mu)$ are the Wilson coefficients which contain the heavy degrees of freedom. Equation 2.39 is a generic form of the effective Hamiltonian. In a renormalized theory, for example using $\overline{\text{MS}}$ renormalization, both C_i and Q_i depend on a energy scale μ where the renormalization scheme is defined, in a such way that the sum of products $H_W^{\Delta S=1}$ doesn't depend on μ. In this work, we use the Wilson coefficients that are computed to next-to-leading order in the $\overline{\text{MS}}$ scheme (using QCD and electro-weak perturbation theory[9]). The ten operators Q_i are defined as:

$$Q_1 = (\bar{s}_\alpha d_\alpha)_L (\bar{u}_\beta u_\beta)_L, \tag{2.40a}$$

$$Q_2 = (\bar{s}_\alpha d_\beta)_L (\bar{u}_\beta u_\alpha)_L, \tag{2.40b}$$

$$Q_3 = (\bar{s}_\alpha d_\alpha)_L \sum_{q=u,d,s} (\bar{q}_\beta q_\beta)_L, \tag{2.40c}$$

$$Q_4 = (\bar{s}_\alpha d_\beta)_L \sum_{q=u,d,s} (\bar{q}_\beta q_\alpha)_L, \tag{2.40d}$$

$$Q_5 = (\bar{s}_\alpha d_\alpha)_L \sum_{q=u,d,s} (\bar{q}_\beta q_\beta)_R, \tag{2.40e}$$

$$Q_6 = (\bar{s}_\alpha d_\beta)_L \sum_{q=u,d,s} (\bar{q}_\beta q_\alpha)_R, \tag{2.40f}$$

$$Q_7 = \frac{3}{2} (\bar{s}_\alpha d_\alpha)_L \sum_{q=u,d,s} e_q (\bar{q}_\beta q_\beta)_R, \tag{2.40g}$$

$$Q_8 = \frac{3}{2} (\bar{s}_\alpha d_\beta)_L \sum_{q=u,d,s} e_q (\bar{q}_\beta q_\alpha)_R, \tag{2.40h}$$

$$Q_9 = \frac{3}{2} (\bar{s}_\alpha d_\alpha)_L \sum_{q=u,d,s} e_q (\bar{q}_\beta q_\beta)_L, \tag{2.40i}$$

$$Q_{10} = \frac{3}{2} (\bar{s}_\alpha d_\beta)_L \sum_{q=u,d,s} e_q (\bar{q}_\beta q_\alpha)_L, \tag{2.40j}$$

where α, β are color indices, the subscripts R and L of each quark bilinear $\bar{q}q'$ is for the corresponding vertices $\bar{q}\gamma_\mu(1 \pm \gamma_5)q'$. Spin indices are contracted in each parenthesis, while

color indices are contracted as shown explicitly.

These 10 operators are not all linearly independent, there are 3 linear relations:

$$Q_{10} - Q_9 = Q_4 - Q_3 \tag{2.41}$$

$$Q_4 - Q_3 = Q_2 - Q_1 \tag{2.42}$$

$$2Q_9 = 3Q_1 - Q_3 \tag{2.43}$$

The last equation is trivial to prove, while the first two equations can be proved using Fierz symmetry:

$$[\gamma^\mu(1-\gamma_5)]_{\alpha\beta}[\gamma_\mu(1-\gamma_5)]_{\gamma\delta} = -[\gamma^\mu(1-\gamma_5)]_{\alpha\delta}[\gamma_\mu(1-\gamma_5)]_{\gamma\beta}, \tag{2.44}$$

where the μ index needs to be summed over on both sides.

Chapter 3

Kaon Decay from Lattice QCD

In this chaper we discuss the procedure to calculate the $K \to \pi\pi$ decay amplitude using lattice QCD techniques. We first describe the general lattice approach to non-perturbatively compute quantity at low energy QCD, and then we discuss how the bare lattice decay matrix elements are determined, lastly the relation between the decay matrix elements in the continuum theory and those on lattice, so that this procedure of computing physical decay amplitude is complete.

3.1 General Lattice QCD Approach

In the path integral formulation of quantum mechanics, any Green function (in Minkowsky space) are written in the form:

$$\langle q_{\alpha_1}(t_1)\cdots q_{\alpha_l}(t_l)\rangle = \frac{\int [Dq] q_{\alpha_1}(t_1)\cdots q_{\alpha_l}(t_l) e^{iS[q]}}{\int [Dq] e^{iS[q]}}, \tag{3.1}$$

where q_{α_i} are the degrees of freedom and $S[q]$ is the classical action of a given configuration q. By doing the analytic continuation:

$$t \rightarrow -i\tau \tag{3.2}$$

$$q_{\alpha_i}(t_i) \rightarrow q_{\alpha_i}(\tau_i) \tag{3.3}$$

$$iS[q] \rightarrow -S_E[q], \tag{3.4}$$

the Euclidean Green function results:

$$\langle q_{\alpha_1}(\tau_1)\cdots q_{\alpha_l}(\tau_l)\rangle = \frac{\int [Dq] q_{\alpha_1}(\tau_1)\cdots q_{\alpha_l}(\tau_l) e^{-S_E[q]}}{\int [Dq] e^{-S_E[q]}} \tag{3.5}$$

When the variables q_{α_i} are those of a continuum field theory, then the techniques of lattice QCD come into play. The lattice formulation and subsequent Monte Carlo evaluation accomplish the following steps:

1. Regulate the path integral by using a grid of points (as well as the links of adjacent points) to represent the degrees of freedom q_α.

2. Generate a sequence of configurations $\{[q]_1, [q]_2 \cdots [q]_N\}$ with a probability distribution given by $e^{-S_E[q]}$. (This step is why we need analytic continuation to Euclidean space.)

3. Perform the ensemble average to evaluate the correlation function:

$$\langle q_{\alpha_1}(\tau_1)\cdots q_{\alpha_l}(\tau_l)\rangle \approx \frac{1}{N}\sum_{i=1}^{N} q_{\alpha_1}(\tau_1)\cdots q_{\alpha_l}(\tau_l)|_{[q]_i}, \tag{3.6}$$

which is straightforward to implement on computer.

Most of the configurations $[q]$ have large actions and only a small fraction of the $[q]$ have significant contribution to the integral. Thus, the average in Equation 3.6 will only be practical if we use importance sampling techniques. We typically obtain the samples $[q]_i$ from a Markov chain generated by the Hybrid Monte Carlo method [10] to efficiently sample

over all possible configurations.

If fermion fields are present in the action, Equation 3.6 for calculating Green function is no longer as simple as it looks. Because a computer can only handle c-numbers but not Grassmann numbers, we must integrate out the fermion degrees of freedom before sampling over the gauge configuration space:

$$\begin{aligned}
\langle O[q,\psi,\bar{\psi}]\rangle &= \frac{\int D[q]D[\bar{\psi}]D[\psi]\langle O\rangle e^{-S_G[q]-S_F[q,\psi,\bar{\psi}]}}{\int D[q]D[\bar{\psi}]D[\psi]e^{-S_G[q]-S_F[q,\psi,\bar{\psi}]}} \\
&= \frac{\int D[q]\left(\int D[\bar{\psi}]D[\psi]\langle O\rangle e^{S_F[q,\psi,\bar{\psi}]}\right)e^{-S_G[q]}}{\int D[q]\left(\int D[\bar{\psi}]D[\psi]e^{-S_F[q,\psi,\bar{\psi}]}\right)e^{-S_G[q]}} \\
&= \frac{\int D[q]\langle O\rangle_{S_F} e^{-S_{eff}[q]}}{\int D[q]e^{-S_{eff}[q]}}, \qquad (3.7)
\end{aligned}$$

where

$$\langle O\rangle_{S_F} = \frac{\int D[\bar{\psi}]D[\psi]O[q,\psi,\bar{\psi}]e^{-S_F[q,\psi,\bar{\psi}]}}{\int D[\bar{\psi}]D[\psi]e^{-S_F[q,\psi,\bar{\psi}]}} \qquad (3.8)$$

$$S_{eff}[q] = S_G[q] - \ln \det\tilde{K}[q] \qquad (3.9)$$

We have assumed a quadratic from $S_F = \bar{\psi}\tilde{K}\psi$ for the fermionic part of the action. $O[q,\psi,\bar{\psi}]$ is any Green function containing fermions and/or gauge variables, and we have used the Grassmann integral formula:

$$\int D[\bar{\psi}]D[\psi]e^{-\bar{\psi}\tilde{K}\psi} = \det\tilde{K}. \qquad (3.10)$$

After these transformations, the effective action S_{eff} contains no Grassmann variables and can be evaluated on a computer. The observable we need to average over those generated gauge configuration now becomes $\langle O\rangle_{S_F}$ as in Equation 3.8, which usually involves the matrix inversion $\tilde{K}^{-1}$ for each pair of fermion fields that appear in $O[q,\psi,\bar{\psi}]$.

For the rest of this section, we will discuss how the QCD action is discretized on lattice.

In lattice QCD, space-time is discretized into a 4-dimension grid, the fermion field is represented by Grassmann numbers on each grid site $\psi(n)$, the gauge field is represented by the SU(3) matrix $U_\mu(n)$ which is defined for each link joining two adjacent sites n and $n+\hat{\mu}$. The link variable $U_\mu(n)$ is related to the continuum gauge field $A_\mu(n)$ by:

$$U_\mu(n) = e^{ig_0 a A_\mu(n)}, \tag{3.11}$$

where a is the lattice spacing and g_0 is the bare coupling constant. With this definition, the field tensor $\mathcal{F}_{\mu\nu}(n)$ is related to the 1×1 plaquette by:

$$e^{ig_0 a^2 \mathcal{F}_{\mu\nu}(n)} = U_\mu(n) U_\nu(n+\hat{\mu}) U_\mu^\dagger(n+\hat{\nu}) U_\nu^\dagger(n) \equiv U_P(n,\mu,\nu) \tag{3.12}$$

This can be proved using the Baker-Campbell-Hausdorff formula: $e^A e^B = e^{A+B+\frac{1}{2}[A,B]+\ldots}$ and neglecting higher order terms in lattice spacing a.

The simplest lattice gauge action was proposed by Wilson [11]:

$$S_G^W(U) = \beta \sum_{x,\mu<\nu} \left(1 - \frac{1}{3}\mathrm{ReTr}\{U_P(x,\mu,\nu)\}\right), \tag{3.13}$$

where $\beta = \frac{6}{g_0^2}$. The Iwasaki gauge action [12][13] in an improved version of the Wilson action, which contains in addition the 1×2 rectangle plaquette:

$$S_G^R(U) = \beta \sum_{x,\mu<\nu} (1 - \frac{c_0}{3})\mathrm{ReTr}\{U_P(x,\mu,\nu)\} + \beta \sum_{x,\mu\neq\nu} (1 - \frac{c_1}{3})\mathrm{ReTr}\{U_R(x,\mu,\nu)\}, \tag{3.14}$$

where $U_R(x,\mu,\nu)$ is the rectangle plaquette:

$$U_R(x,\mu,\nu) = U_\mu(n) U_\mu(n+\hat{\mu}) U_\nu(n+2\hat{\mu}) U_\mu^\dagger(n+\hat{\mu}+\hat{\nu}) U_\mu^\dagger(n+\hat{\nu}) U_\nu^\dagger(n), \tag{3.15}$$

and c_0 and c_1 are two constants, $c_1 = -0.331$ and $c_0 = 1 - 8c_1$. For the fermion action, we

have used the Domain Wall Fermion (DWF) action [14]. It introduces an extra dimension labeled by s, and the action is written as:

$$S_F^{DWF} = -\sum_{n,s;n',s'} \bar{\psi}(n,s) D^{DWF}(n,s;n',s') \psi(n',s'), \tag{3.16}$$

where the 5-dimension Dirac operator D^{DWF} is (as in Ref. [15]):

$$D^{DWF}(n,s;n',s') = \delta_{s,s'} D^{\parallel}_{n,n'} + \delta_{n,n'} D^{\perp}_{s,s'} \ . \tag{3.17}$$

$D^{\parallel}$ is the Dirac operator for Wilson fermions:

$$D^{\parallel}_{n,n'} = \frac{1}{2} \sum_{\mu} \left((1-\gamma_\mu) U_\mu(n) \delta_{n+\hat{\mu},n'} + (1+\gamma_\mu) U^\dagger_\mu(n') \delta_{n-\hat{\mu},n'} \right) + (M-4)\delta_{n,n'}, \tag{3.18}$$

and $D^{\perp}_{n,n'}$ is:

$$\begin{aligned} D^{\perp}_{s,s'} \ &= \ \frac{1}{2}[(1-\gamma_5)\delta_{s+1,s'} + (1+\gamma_5)\delta_{s-1,s'} - 2\delta_{s,s'}] \\ &\quad -\frac{m}{2}[(1-\gamma_5)\delta_{s,L_s-1}\delta_{0,s'} + (1+\gamma_5)\delta_{s,0}\delta_{L_s-1,s'}], \end{aligned} \tag{3.19}$$

where s or s' lie in the range $0 \leq s, s' \leq L_s - 1$. The five-dimension mass M represents the height of domain wall in Kaplan's original language. With the choice of $0 < M < 2$, the fermion with left-hand chirality is exponentially bound to the $s = 0$ domain wall and the right-hand chirality to the $s = L_s - 1$ domain wall. These two domain walls are coupled by the mass m, which then represents the input bare quark mass. The DWF action solves the fermion doubling problem [16] while exponentially suppressing chiral symmetry as the fifth dimension goes, which ensures that the operator mixing pattern remains the same as in the continuum limit. All the $16^3 \times 32$ ensembles in this work use the DWF action, and the $32^3 \times 64$ ensemble uses the Möbius DWF action [17], an improved version of DWF that

reduces computational cost by reducing L_s while keeping chiral symmetry breaking effects the same.

3.2 Weak Matrix Elements in Lattice QCD

In section 2.5 the $\Delta S = 1$ effective weak Hamiltonian is decomposed into ten operators, so the next step is to evaluate each of the ten decay matrix elements $M_i \equiv \langle \pi\pi | Q_i | K \rangle$. To do this we first determine the bare lattice decay matrix elements M_i^{lat} from the Euclidean three-point function $\langle J_{\pi\pi}(t_{\pi\pi}) Q_i(t_Q) J_K(t_K) \rangle$:

$$\langle J_{\pi\pi}(t_{\pi\pi}) Q_i(t_Q) J_K(t_K) \rangle = \langle 0 | J_{\pi\pi}(t_{\pi\pi}) | \pi\pi \rangle \langle \pi\pi | Q_i(t_Q) | K \rangle \langle K | J_K(t_K) \rangle | 0 \rangle + \cdots \tag{3.20}$$

The dots are the excited states contributions above $\pi\pi$ and kaon ground states. In the limit of $t_{\pi\pi} \gg t_Q \gg t_K$, the ground states $E_{\pi\pi}$ and E_K dominates:

$$\langle J_{\pi\pi}(t_{\pi\pi}) Q_i(t_Q) J_K(t_K) \rangle = M_i^{lat} Z^{\pi\pi} Z^K e^{-E_{\pi\pi}(t_{\pi\pi} - t_Q) - E_K(t_Q - t_K)}. \tag{3.21}$$

The energy and normalization factor for $\pi\pi$ and kaon states, ($E_{\pi\pi}$, E_K, $Z^{\pi\pi}$, and Z^K) are determined from the time dependence of the two point functions:

$$\langle 0 | J_X^\dagger(t) J_X(0) | 0 \rangle = Z_X^2 (e^{-E_X t} + e^{-E_X(T-t)}), \tag{3.22}$$

for $T \gg t \gg 0$, $X \in \{\pi\pi, K\}$. T is the lattice size in time direction.

The phase convention for meson operators in this work is:

$$|\pi^+\rangle = i\bar{u}\gamma_5 d|0\rangle \qquad \langle\pi^+| = \langle 0|i\bar{d}\gamma_5 u \tag{3.23}$$

$$|\pi^-\rangle = -i\bar{d}\gamma_5 u|0\rangle \qquad \langle\pi^-| = -\langle 0|i\bar{u}\gamma_5 d \tag{3.24}$$

$$|\pi^0\rangle = \frac{i}{\sqrt{2}}(\bar{u}\gamma_5 u - \bar{d}\gamma_5 d)|0\rangle \qquad \langle\pi^0| = \langle 0|\frac{i}{\sqrt{2}}(\bar{u}\gamma_5 u - \bar{d}\gamma_5 d) \tag{3.25}$$

$$|K^0\rangle = i\bar{d}\gamma_5 s|0\rangle \qquad \langle K^0| = \langle 0|i\bar{s}\gamma_5 d \tag{3.26}$$

$$|\overline{K^0}\rangle = -i\bar{s}\gamma_5 d|0\rangle \qquad \langle\overline{K^0}| = -\langle 0|i\bar{d}\gamma_5 s \tag{3.27}$$

In the context of G-parity boundary condition, we use a two-component quark field for each SU(2) quark pair (more details about G-parity boundary conditions are given in Chapter 4):

$$\psi = \begin{pmatrix} \psi^{(0)} \\ \psi^{(1)} \end{pmatrix} = \begin{pmatrix} d \\ C\bar{u}^T \end{pmatrix} \tag{3.28}$$

$$\psi_H = \begin{pmatrix} \psi_H^{(0)} \\ \psi_H^{(1)} \end{pmatrix} = \begin{pmatrix} s \\ C\bar{s'}^T \end{pmatrix} \tag{3.29}$$

In this definition we have introduced the SU(2) isospin partner s' for strange quark s, to give correct kinematics to ground state kaon (which shall be clear soon). The boundary conditions for the ψ and ψ_H fields are:

$$\psi(L_z + z) = i\sigma_2\psi(z) \tag{3.30}$$

$$\bar{\psi}(L_z + z) = -i\bar{\psi}(z)\sigma_2, \tag{3.31}$$

σ_2 is the second Pauli matrix and $\hat{z}$ is the direction with the G-parity boundary. The same condition is true for the ψ_H field. The pion and kaon operators in Equation 3.27 can be

rewritten using the two-component ψ and ψ_H fields:

$$|\pi^+\rangle = \frac{i}{2}\psi^T(\gamma_5\sigma_1 C)\psi|0\rangle \qquad \langle\pi^+| = \langle 0|\frac{i}{2}\bar{\psi}(\gamma_5\sigma_1 C)\bar{\psi}^T \tag{3.32}$$

$$|\pi^-\rangle = -\frac{i}{2}\bar{\psi}(\gamma_5\sigma_1 C)\bar{\psi}^T|0\rangle \qquad \langle\pi^-| = -\langle 0|\frac{i}{2}\psi^T(\gamma_5\sigma_1 C)\psi \tag{3.33}$$

$$|\pi^0\rangle = -\frac{i}{\sqrt{2}}\bar{\psi}\sigma_3\gamma_5\psi|0\rangle \qquad \langle\pi^0| = -\langle 0|\frac{i}{\sqrt{2}}\bar{\psi}\sigma_3\gamma_5\psi \tag{3.34}$$

$$|K^{0\prime}\rangle = \frac{i}{\sqrt{2}}(\bar{\psi}\gamma_5\psi_H)|0\rangle \qquad \langle K^{0\prime}| = \langle 0|\frac{i}{\sqrt{2}}(\bar{\psi}_H\gamma_5\psi) \tag{3.35}$$

$$|\overline{K^{0\prime}}\rangle = -\frac{i}{\sqrt{2}}(\bar{\psi}_H\gamma_5\psi)|0\rangle \qquad \langle\overline{K^{0\prime}}| = -\langle 0|\frac{i}{\sqrt{2}}(\bar{\psi}\gamma_5\psi_H) \tag{3.36}$$

The $K^{0\prime}$ operator is different from the usual kaon since we now have to include the G-parity counterpart of the usual $i\bar{d}\gamma_5 s$ to make the kaon operator translational invariant:

$$\begin{aligned} |K^{0\prime}\rangle &= \frac{i}{\sqrt{2}}(\bar{d}\gamma_5 s + \bar{s}'\gamma_5 u)|0\rangle \\ &= \frac{i}{\sqrt{2}}(\bar{\psi}F_0\gamma_5 F_0\psi_H + \psi_H^T F_1 C\gamma_5 C F_1\bar{\psi}^T)|0\rangle \\ &= \frac{i}{\sqrt{2}}(\bar{\psi}\gamma_5\psi_H)|0\rangle, \end{aligned} \tag{3.37}$$

where F_0, F_1 are shorthand for $\begin{pmatrix} 1 & 0 \\ 0 & 0 \end{pmatrix}$ and $\begin{pmatrix} 0 & 0 \\ 0 & 1 \end{pmatrix}$.

Another example of this procedure is the derivation of Equation 3.32:

$$\begin{aligned} |\pi^+\rangle &= i\bar{u}\gamma_5 d|0\rangle \\ &= \frac{i}{2}(\bar{u}\gamma_5 d - d^T\gamma_5\bar{u}^T)|0\rangle \\ &= \frac{i}{2}(\psi^T F_1\gamma_5\sigma_1 C F_0\psi + \psi^T F_0\gamma_5\sigma_1 C F_1\psi)|0\rangle \\ &= \frac{i}{2}\psi^T(\gamma_5\sigma_1 C)\psi|0\rangle, \end{aligned} \tag{3.38}$$

Now we can check the boundary conditions obeyed by the pion and kaon operators:

$$\begin{aligned}\pi^+(L_z+z) &= \frac{i}{2}\psi^T(L_z+z)(\gamma_5\sigma_1 C)\psi(L_z+z)\\ &= \frac{i}{2}\psi^T(z)(i\sigma_2^T)(\gamma_5\sigma_1 C)(i\sigma_2)\psi(z)\\ &= -\pi^+(z)\end{aligned} \tag{3.39}$$

This shows the π^+ operator satisfies anti-periodic boundary conditions and the allowed momenta can only be $p_z = (\frac{1}{2}+n)\frac{\pi}{L},\ n \in Z$. A similar relation can be derived for π^- and π^0. For $K^{0\prime}$ we find:

$$\begin{aligned}K^{0\prime}(L_z+z) &= \frac{i}{\sqrt{2}}\bar{\psi}(L_z+z)\gamma_5\psi_H(L_z+z)\\ &= \frac{i}{\sqrt{2}}\bar{\psi}(z)(-i\sigma_2)\gamma_5(i\sigma_2)\psi_H(z)\\ &= K^{0\prime}(z)\end{aligned} \tag{3.40}$$

This shows the $K^{0\prime}$ operator satisfies periodic boundary condition and that the corresponding ground state is a static kaon. We can now see the reason to introduce the fictional s' quark field. With this setup, the mesons' kinematics are just what's needed in $K \to \pi\pi$ decay.

For future convenience, we define two matrices

$$\begin{aligned}S_1 &= \gamma_5\sigma_1 C\\ S_2 &= \sigma_3\gamma_5,\end{aligned} \tag{3.41}$$

where the σ_i are the standard Pauli matrices.

3.2.1 $\pi - \pi$ scattering

Under G-parity boundary condition, kaon's ground state carries zero momentum, which is unchanged under cubic rotation. As a result, kaon in this setup only couples to $\pi\pi$ state which is also symmetrical under cubic rotation, namely in the A_2 representation of cubic group.

We will label the four s-wave $\pi\pi$ states as $|II_z\rangle$, where I and I_z are the two isospin quantum numbers. The notation "s-wave" indicate a state in the A_2 representation of the cubic group, the representation which is found in the $l = 0$ representation of the rotation group.

$$|22(\text{s-wave})\rangle = \frac{1}{2^{n_{tw}}}\sum_{i=1}^{2^{n_{tw}}}|\pi^+(p_i)\rangle|\pi^+(-p_i)\rangle \tag{3.42}$$

$$|21(\text{s-wave})\rangle = \frac{1}{2^{n_{tw}}}\sum_{i=1}^{2^{n_{tw}}}\frac{1}{\sqrt{2}}\{|\pi^+(p_i)\rangle|\pi^0(-p_i)\rangle + |\pi^+(p_i)\rangle|\pi^0(-p_i)\rangle\} \tag{3.43}$$

$$|20(\text{s-wave})\rangle = \frac{1}{2^{n_{tw}}}\sum_{i=1}^{2^{n_{tw}}}\frac{1}{\sqrt{6}}\{|\pi^+(p_i)\rangle|\pi^-(-p_i)\rangle + 2|\pi^0(p_i)\rangle|\pi^0(-p_i)\rangle + |\pi^-(p_i)\rangle|\pi^+(-p_i)\rangle\} \tag{3.44}$$

$$|00(\text{s-wave})\rangle = \frac{1}{2^{n_{tw}}}\sum_{i=1}^{2^{n_{tw}}}\frac{1}{\sqrt{3}}\{|\pi^+(p_i)\rangle|\pi^-(-p_i)\rangle - |\pi^0(p_i)\rangle|\pi^0(-p_i)\rangle + |\pi^-(p_i)\rangle|\pi^+(-p_i)\rangle\}, \tag{3.45}$$

where n_{tw} is the number of G-parity twists, which could vary from 1 to 3. $2^{n_{tw}}$ is the degeneracy of ground state pion momentum. Depending on the isospin quantum number I, the $\pi\pi$ correlation functions involves different Wick contractions, which can be categorized into four graphs, each corresponding to a particular choice of contractions, as in Table 3.1.

In Table 3.1, $t_i (i = 1, 2, 3, 4)$ are the time coordinates of the $\pi\pi$ source and sink interpolating operators as in Figure 3.1 In this work, we have used a non-zero time separation between the two pions in the source $\pi\pi$ as well as in sink, in order to suppress fluctuation

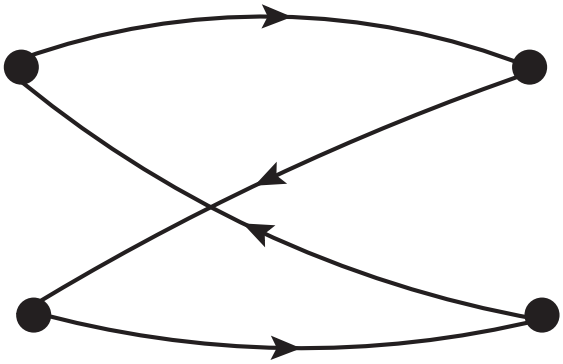	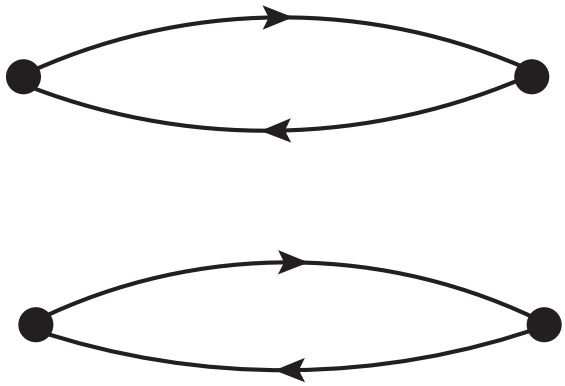
$C = \frac{1}{2}Tr\{\mathcal{G}_{t_1,t_3}S_2\mathcal{G}_{t_3,t_2}S_2\mathcal{G}_{t_2,t_4}S_2\mathcal{G}_{t_4,t_1}S_2\}$	$D = \frac{1}{2}[(\frac{1}{2}Tr\{\mathcal{G}_{t_1,t_3}S_2\mathcal{G}_{t_3,t_1}S_2\}) \cdot (\frac{1}{2}Tr\{\mathcal{G}_{t_2,t_4}S_2\mathcal{G}_{t_4,t_2}S_2\}) + (t_3 \leftrightarrow t_4)]$
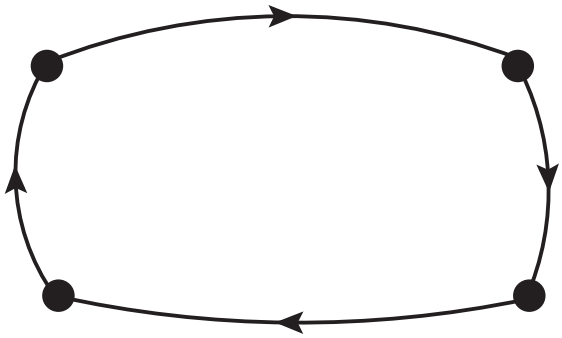	
$R = \frac{1}{2}[\frac{1}{2}Tr\{\mathcal{G}_{t_1,t_2}S_2\mathcal{G}_{t_2,t_3}S_2\mathcal{G}_{t_3,t_4}S_2\mathcal{G}_{t_4,t_1}S_2\} + (t_3 \leftrightarrow t_4)]$	$V = (\frac{1}{2}Tr\{\mathcal{G}_{t_1,t_2}S_2\mathcal{G}_{t_2,t_1}S_2\}) \cdot (\frac{1}{2}Tr\{\mathcal{G}_{t_3,t_3}S_2\mathcal{G}_{t_4,t_4}S_2\})$

Table 3.1: Wick contractions in $\pi\pi$ correlation function.

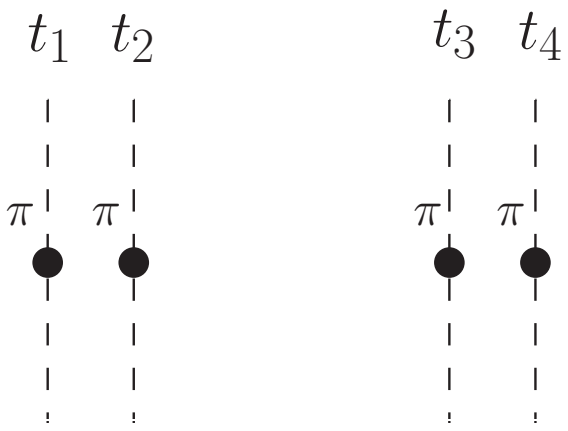

Figure 3.1: Time coordinates in pion-pion scattering. Left: source $\pi\pi$. Right: sink $\pi\pi$.

from the vacuum graph [18] and to avoid an unwanted contraction arising from the use of all-to-all propagators (see Chapter 4). The quark propagator $\mathcal{G}_{t_1,t_2}$ in Table 3.1 is the wall-source propagator from time slice t_2 to time slice t_1, and for simplicity I haven't written out the momentum quantum number. But it should be understood that $\pi\pi$ state carries momentum and a more general form is:

The $\pi\pi$ correlation functions are linear combinations of these four graphs. Taking into consideration of Grassmann algebra as well as the imaginary number i in pion creation/annihilation operators, we can work out the formula:

$$\langle 20(\text{s-wave})|20(\text{s-wave})\rangle = \frac{1}{2^{n_{tw}}}\sum_{i=1}^{2^{n_{tw}}}\frac{1}{2^{n_{tw}}}\sum_{j=1}^{2^{n_{tw}}}(2D_{p_i,-p_i;p_j,-p_j} - 2C_{p_i,-p_i;p_j,-p_j}) \tag{3.46}$$

$$\langle 00(\text{s-wave})|00(\text{s-wave})\rangle = \frac{1}{2^{n_{tw}}}\sum_{i=1}^{2^{n_{tw}}}\frac{1}{2^{n_{tw}}}\sum_{j=1}^{2^{n_{tw}}}\cdot (2D_{p_i,-p_i;p_j,-p_j} + C_{p_i,-p_i;p_j,-p_j} - 6R_{p_i,-p_i;p_j,-p_j} + 3V_{p_i,-p_i;p_j,-p_j}) \tag{3.47}$$

where the contractions now carry four three-momentum quantum numbers, corresponding to the four pions in Figure 3.1. Expressed by quark wall-source propagators, these

contractions are:

$$C_{\vec{p}_1,\vec{p}_2;\vec{p}_3,\vec{p}_4} = \frac{1}{2}Tr\{\mathcal{G}_{t_1,\vec{k}_1;t_2,\vec{k}_6}S_2\mathcal{G}_{t_2,\vec{k}_5;t_1,\vec{k}_4}S_2\mathcal{G}_{t_1,\vec{k}_3,t_2,\vec{k}_8}S_2\mathcal{G}_{t_2,\vec{k}_7,t_1,\vec{k}_2}S_2\} \tag{3.48a}$$

$$\begin{aligned} D_{\vec{p}_1,\vec{p}_2;\vec{p}_3,\vec{p}_4} = & \frac{1}{2}[\frac{1}{2}Tr\{\mathcal{G}_{t_1,\vec{k}_1;t_2,\vec{k}_6}S_2\mathcal{G}_{t_2,\vec{k}_5;t_1,\vec{k}_2}S_2\}\cdot\frac{1}{2}Tr\{\mathcal{G}_{t_1,\vec{k}_3;t_2,\vec{k}_8}S_2\mathcal{G}_{t_2,\vec{k}_7;t_1,\vec{k}_4}S_2\} \\ & +\frac{1}{2}Tr\{\mathcal{G}_{t_1,\vec{k}_1;t_2\vec{k}_8}S_2\mathcal{G}_{t_2,\vec{k}_7;t_1,\vec{k}_2}S_2\}\cdot\frac{1}{2}Tr\{\mathcal{G}_{t_1,\vec{k}_3;t_2,\vec{k}_6}S_2\mathcal{G}_{t_2,\vec{k}_5;t_1,\vec{k}_4}S_2\}] \end{aligned} \tag{3.48b}$$

$$\begin{aligned} R_{\vec{p}_1,\vec{p}_2;\vec{p}_3,\vec{p}_4} = & \frac{1}{2}[\frac{1}{2}Tr\{\mathcal{G}_{t_1,\vec{k}_1;t_1,\vec{k}_4}S_2\mathcal{G}_{t_1,\vec{k}_3;t_2,\vec{k}_6}S_2\mathcal{G}_{t_2,\vec{k}_5;t_2,\vec{k}_8}S_2\mathcal{G}_{t_2,\vec{k}_7,t_1,\vec{k}_2}S_2\} \\ & +\frac{1}{2}Tr\{\mathcal{G}_{t_1,\vec{k}_1;t_1,\vec{k}_4}S_2\mathcal{G}_{t_1,\vec{k}_3;t_2,\vec{k}_8}S_2\mathcal{G}_{t_2,\vec{k}_7;t_2,\vec{k}_6}S_2\mathcal{G}_{t_2,\vec{k}_5,t_1,\vec{k}_2}S_2\}] \end{aligned} \tag{3.48c}$$

$$V_{\vec{p}_1,\vec{p}_2;\vec{p}_3,\vec{p}_4} = (\frac{1}{2}Tr\{\mathcal{G}_{t_1,\vec{k}_1;t_1,\vec{k}_4}S_2\mathcal{G}_{t_1,\vec{k}_3;t_1,\vec{k}_2}S_2\})\cdot(\frac{1}{2}Tr\{\mathcal{G}_{t_2,\vec{k}_5;t_2,\vec{k}_8}S_2\mathcal{G}_{t_2,\vec{k}_7;t_2,\vec{k}_6}S_2\}), \tag{3.48d}$$

where the momentum index $\vec{k}_i$ specifies the momentum given to the ith quark momenta in each pion:

$$\vec{p}_1 = \vec{k}_1 + \vec{k}_2 \tag{3.49}$$

$$\vec{p}_2 = \vec{k}_3 + \vec{k}_4 \tag{3.50}$$

$$\vec{p}_3 = \vec{k}_5 + \vec{k}_6 \tag{3.51}$$

$$\vec{p}_4 = \vec{k}_7 + \vec{k}_8 \tag{3.52}$$

If using all-to-all propagators (see Chapter 4) instead of wall-source propagators, Equa-

tion 3.48 is written as:

$$C_{\vec{p}_1,\vec{p}_2;\vec{p}_3,\vec{p}_4} = \frac{1}{2}\sum_{i,j,k,l}\Pi^{ij}_{t_1,p_1}\Pi^{jk}_{t_3,p_3}\Pi^{kl}_{t_2,p_2}\Pi^{li}_{t_4,p_4} \tag{3.53a}$$

$$D_{\vec{p}_1,\vec{p}_2;\vec{p}_3,\vec{p}_4} = \frac{1}{8}\sum_{i,j,k,l}(\Pi^{ij}_{t_1,p_1}\Pi^{ji}_{t_3,p_3}\Pi^{kl}_{t_2,p_2}\Pi^{lk}_{t_4,p_4} + \Pi^{ij}_{t_1,p_1}\Pi^{ji}_{t_4,p_4}\Pi^{kl}_{t_2,p_2}\Pi^{lk}_{t_3,p_3}) \tag{3.53b}$$

$$R_{\vec{p}_1,\vec{p}_2;\vec{p}_3,\vec{p}_4} = \frac{1}{4}\sum_{i,j,k,l}(\Pi^{ij}_{t_1,p_1}\Pi^{jk}_{t_2,p_2}\Pi^{kl}_{t_3,p_3}\Pi^{li}_{t_4,p_4} + \Pi^{ij}_{t_1,p_1}\Pi^{jk}_{t_2,p_2}\Pi^{kl}_{t_4,p_4}\Pi^{li}_{t_3,p_3}) \tag{3.53c}$$

$$V_{\vec{p}_1,\vec{p}_2;\vec{p}_3,\vec{p}_4} = \frac{1}{4}\sum_{i,j,k,l}\Pi^{ij}_{t_1,p_1}\Pi^{ji}_{t_2,p_2}\Pi^{kl}_{t_3,p_3}\Pi^{lk}_{t_4,p_4} \tag{3.53d}$$

The meson field $\Pi^{ij}_{t_n,p_n}$ arises from the use of all-to-all propagators and it represents the nth meson with time coordinate t_n and momentum p_n. There are multiple ways that a pion's momentum can be decomposed into quarks' momenta, in this work we use Table 4.1.

3.2.2 $K \to \pi\pi$

Using the G-parity two-component field notation (Equation 3.29), the ten $\Delta S = 1$ operators are written as:

$$
\begin{aligned}
Q_1 &= (\bar{\psi}_{H,\alpha} M_{0,V-A} \psi_\alpha)(\bar{\psi}_\beta M_{1,V+A} \psi_\beta) \\
Q_2 &= (\bar{\psi}_{H,\alpha} M_{0,V-A} \psi_\beta)(\bar{\psi}_\alpha M_{1,V+A} \psi_\beta) \\
Q_3 &= (\bar{\psi}_{H,\alpha} M_{0,V-A} \psi_\alpha)[(\bar{\psi}_\beta M_{1,V+A} \psi_\beta) + (\bar{\psi}_\beta M_{0,V-A} \psi_\beta) + (\bar{\psi}_{H,\beta} M_{0,V-A} \psi_{H,\beta})] \\
Q_4 &= (\bar{\psi}_{H,\alpha} M_{0,V-A} \psi_\beta)[(\bar{\psi}_\alpha M_{1,V+A} \psi_\beta) + (\bar{\psi}_\beta M_{0,V-A} \psi_\alpha) + (\bar{\psi}_{H,\beta} M_{0,V-A} \psi_{H,\alpha})] \\
Q_5 &= (\bar{\psi}_{H,\alpha} M_{0,V-A} \psi_\alpha)[(\bar{\psi}_\beta M_{1,V-A} \psi_\beta) + (\bar{\psi}_\beta M_{0,V+A} \psi_\beta) + (\bar{\psi}_{H,\beta} M_{0,V+A} \psi_{H,\beta})] \\
Q_6 &= (\bar{\psi}_{H,\alpha} M_{0,V-A} \psi_\beta)[(\bar{\psi}_\alpha M_{1,V-A} \psi_\beta) + (\bar{\psi}_\beta M_{0,V+A} \psi_\alpha) + (\bar{\psi}_{H,\beta} M_{0,V+A} \psi_{H,\alpha})] \\
Q_7 &= \frac{3}{2}(\bar{\psi}_{H,\alpha} M_{0,V-A} \psi_\alpha)[\frac{2}{3}(\bar{\psi}_\beta M_{1,V-A} \psi_\beta) + \frac{-1}{3}(\bar{\psi}_\beta M_{0,V+A} \psi_\beta) + \frac{-1}{3}(\bar{\psi}_{H,\beta} M_{0,V+A} \psi_{H,\beta})] \\
Q_8 &= \frac{3}{2}(\bar{\psi}_{H,\alpha} M_{0,V-A} \psi_\beta)[\frac{2}{3}(\bar{\psi}_\alpha M_{1,V-A} \psi_\beta) + \frac{-1}{3}(\bar{\psi}_\beta M_{0,V+A} \psi_\alpha) + \frac{-1}{3}(\bar{\psi}_{H,\beta} M_{0,V+A} \psi_{H,\alpha})] \\
Q_9 &= \frac{3}{2}(\bar{\psi}_{H,\alpha} M_{0,V-A} \psi_\alpha)[\frac{2}{3}(\bar{\psi}_\beta M_{1,V+A} \psi_\beta) + \frac{-1}{3}(\bar{\psi}_\beta M_{0,V-A} \psi_\beta) + \frac{-1}{3}(\bar{\psi}_{H,\beta} M_{0,V-A} \psi_{H,\beta})] \\
Q_{10} &= \frac{3}{2}(\bar{\psi}_{H,\alpha} M_{0,V-A} \psi_\beta)[\frac{2}{3}(\bar{\psi}_\alpha M_{1,V+A} \psi_\beta) + \frac{-1}{3}(\bar{\psi}_\beta M_{0,V-A} \psi_\alpha) + \frac{-1}{3}(\bar{\psi}_{H,\beta} M_{0,V-A} \psi_{H,\alpha})],
\end{aligned}
$$

where α, β are color indices and the spin-flavor matrices $M_{i,V\pm A}$ are defined as:

$$
\begin{aligned}
M_{1,V-A} &= -F_1 \gamma_u (1 - \gamma_5) && \text{(3.54a)} \\
M_{1,V+A} &= -F_1 \gamma_u (1 + \gamma_5) && \text{(3.54b)} \\
M_{0,V-A} &= F_0 \gamma_u (1 - \gamma_5) && \text{(3.54c)} \\
M_{0,V+A} &= F_0 \gamma_u (1 + \gamma_5) && \text{(3.54d)} \\
F_0 &= \begin{pmatrix} 1 & 0 \\ 0 & 0 \end{pmatrix} && \text{(3.54e)} \\
F_1 &= \begin{pmatrix} 0 & 0 \\ 0 & 1 \end{pmatrix} && \text{(3.54f)}
\end{aligned}
$$

Let $A_{I,i}$ represent the correlation function $\langle J_I^{\pi\pi}(x_{\pi_1}, x_{\pi_2}) Q_i(x_{op}) J^K(x_K)\rangle$. Similar to $\pi\pi$ scattering, all the Wick contractions are categorized graphically as in Appendix B. The correlation function $\langle J_I^{\pi\pi}(x_{\pi_1}, x_{\pi_2}) Q_i(x_{op}) J^K(x_K)\rangle$ is a linear combination of all those contractions, which are summarized as follows:

$\Delta I = 3/2$ part:

$$
\begin{aligned}
A_{2,1} &= \frac{i}{\sqrt{3}}\{C1(-M_{1,V+A}, M_{0,V-A}) - C4(M_{0,V-A}, M_{0,V-A} - M_{1,V+A})\} \\
A_{2,2} &= A_{2,1} \\
A_{2,3} &= 0 \\
A_{2,4} &= 0 \\
A_{2,5} &= 0 \\
A_{2,6} &= 0 \\
A_{2,7} &= \frac{\sqrt{3}i}{2}\{C1(-M_{1,V-A}, M_{0,V-A}) - C4(M_{0,V-A}, M_{0,V+A} - M_{1,V-A})\} \\
A_{2,8} &= \frac{\sqrt{3}i}{2}\{C3(M_{0,V+A}, M_{0,V-A}) - C6(M_{0,V-A}, M_{0,V+A}) + C5(M_{0,V-A}, M_{1,V-A})\} \\
A_{2,9} &= \frac{3}{2}A_{2,1} \\
A_{2,10} &= \frac{3}{2}A_{2,2}
\end{aligned}
$$

$\Delta I = 1/2$ part:

$$
\begin{aligned}
A_{0,1} &= \frac{i}{\sqrt{6}}\{C1(M_{1,V+A}, M_{0,V-A}) - C4(M_{0,V-A}, M_{1,V+A}) - 2\cdot C4(M_{0,V-A}, M_{0,V-A}) \\
&\quad +3\cdot C7(M_{0,V-A}, M_{1,V+A}) - 3\cdot C10(M_{1,V+A}, M_{0,V-A}) + 3\cdot C13(M_{0,V-A}, M_{1,V+A}) \\
&\quad -3\cdot C16(M_{1,V+A}, M_{0,V-A}) + 3\cdot C23(M_{0,V-A}, M_{1,V+A}) - 3\cdot C26(M_{1,V+A}, M_{0,V-A})\} \\
A_{0,2} &= \frac{i}{\sqrt{6}}\{C2(M_{1,V+A}, M_{0,V-A}) - C5(M_{0,V-A}, M_{1,V+A}) - 2\cdot C6(M_{0,V-A}, M_{0,V-A}) \\
&\quad +3\cdot C8(M_{0,V-A}, M_{1,V+A}) - 3\cdot C11(M_{1,V+A}, M_{0,V-A}) + 3\cdot C14(M_{0,V-A}, M_{1,V+A}) \\
&\quad -3\cdot C17(M_{1,V+A}, M_{0,V-A}) + 3\cdot C24(M_{0,V-A}, M_{1,V+A}) - 3\cdot C27(M_{1,V+A}, M_{0,V-A})\}
\end{aligned}
$$

$$
\begin{aligned}
A_{0,3} &= \frac{i}{\sqrt{6}}\{-3\cdot C4(M_{0,V-A},M_{1,V+A})-3\cdot C4(M_{0,V-A},M_{0,V-A})+3\cdot C7(M_{0,V-A},M_{1,V+A})\\
&\quad +3\cdot C7(M_{0,V-A},M_{0,V-A})-3\cdot C10(M_{1,V+A},M_{0,V-A})-3\cdot C10(M_{0,V-A},M_{0,V-A})\\
&\quad +3\cdot C13(M_{0,V-A},M_{1,V+A})+3\cdot C13(M_{0,V-A},M_{0,V-A})-3\cdot C16(M_{1,V+A},M_{0,V-A})\\
&\quad -3\cdot C16(M_{0,V-A},M_{0,V-A})+3\cdot C19(M_{0,V-A},M_{0,V-A})-3\cdot C21(M_{0,V-A},M_{0,V-A})\\
&\quad +3\cdot C23(M_{0,V-A},M_{1,V+A})+3\cdot C23(M_{0,V-A},M_{0,V-A})-3\cdot C26(M_{1,V+A},M_{0,V-A})\\
&\quad -3\cdot C26(M_{0,V-A},M_{0,V-A})+3\cdot C29(M_{0,V-A},M_{0,V-A})-3\cdot C31(M_{0,V-A},M_{0,V-A})\}\\
A_{0,4} &= \frac{i}{\sqrt{6}}\{C3(M_{0,V-A},M_{0,V-A})-3\cdot C6(M_{0,V-A},M_{0,V-A})+C2(M_{1,V+A},M_{0,V-A})\\
&\quad -3\cdot C5(M_{0,V-A},M_{1,V+A})+3\cdot C8(M_{0,V-A},M_{1,V+A})+3\cdot C9(M_{0,V-A},M_{0,V-A})\\
&\quad -3\cdot C11(M_{1,V+A},M_{0,V-A})-3\cdot C12(M_{0,V-A},M_{0,V-A})+3\cdot C14(M_{0,V-A},M_{1,V+A})\\
&\quad +3\cdot C15(M_{0,V-A},M_{0,V-A})-3\cdot C17(M_{1,V+A},M_{0,V-A})-3\cdot C18(M_{0,V-A},M_{0,V-A})\\
&\quad +3\cdot C20(M_{0,V-A},M_{0,V-A})-3\cdot C22(M_{0,V-A},M_{0,V-A})+3\cdot C24(M_{0,V-A},M_{1,V+A})\\
&\quad +3\cdot C25(M_{0,V-A},M_{0,V-A})-3\cdot C27(M_{1,V+A},M_{0,V-A})-3\cdot C28(M_{0,V-A},M_{0,V-A})\\
&\quad +3\cdot C30(M_{0,V-A},M_{0,V-A})-3\cdot C32(M_{0,V-A},M_{0,V-A})\}\\
A_{0,5} &= \frac{i}{\sqrt{6}}\{-3\cdot C4(M_{0,V-A},M_{1,V-A})-3\cdot C4(M_{0,V-A},M_{0,V+A})+3\cdot C7(M_{0,V-A},M_{1,V-A})\\
&\quad +3\cdot C7(M_{0,V-A},M_{0,V+A})-3\cdot C10(M_{1,V-A},M_{0,V-A})-3\cdot C10(M_{0,V+A},M_{0,V-A})\\
&\quad +3\cdot C13(M_{0,V-A},M_{1,V-A})+3\cdot C13(M_{0,V-A},M_{0,V+A})-3\cdot C16(M_{1,V-A},M_{0,V-A})\\
&\quad -3\cdot C16(M_{0,V+A},M_{0,V-A})+3\cdot C19(M_{0,V-A},M_{0,V+A})-3\cdot C21(M_{0,V-A},M_{0,V+A})\\
&\quad +3\cdot C23(M_{0,V-A},M_{1,V-A})+3\cdot C23(M_{0,V-A},M_{0,V+A})-3\cdot C26(M_{1,V-A},M_{0,V-A})\\
&\quad -3\cdot C26(M_{0,V+A},M_{0,V-A})+3\cdot C29(M_{0,V-A},M_{0,V+A})-3\cdot C31(M_{0,V-A},M_{0,V+A})\}\\
A_{0,6} &= \frac{i}{\sqrt{6}}\{C3(M_{0,V+A},M_{0,V-A})-3\cdot C6(M_{0,V-A},M_{0,V+A})+C2(M_{1,V-A},M_{0,V-A})\\
&\quad -3\cdot C5(M_{0,V-A},M_{1,V-A})+3\cdot C8(M_{0,V-A},M_{1,V-A})+3\cdot C9(M_{0,V-A},M_{0,V+A})\\
&\quad -3\cdot C11(M_{1,V-A},M_{0,V-A})-3\cdot C12(M_{0,V+A},M_{0,V-A})+3\cdot C14(M_{0,V-A},M_{1,V-A})\\
&\quad +3\cdot C15(M_{0,V-A},M_{0,V+A})-3\cdot C17(M_{1,V-A},M_{0,V-A})-3\cdot C18(M_{0,V+A},M_{0,V-A})
\end{aligned}
$$

$$
\begin{aligned}
&+3\cdot C20(M_{0,V-A},M_{0,V+A})-3\cdot C22(M_{0,V-A},M_{0,V+A})+3\cdot C24(M_{0,V-A},M_{1,V-A})\\
&+3\cdot C25(M_{0,V-A},M_{0,V+A})-3\cdot C27(M_{1,V-A},M_{0,V-A})-3\cdot C28(M_{0,V+A},M_{0,V-A})\\
&+3\cdot C30(M_{0,V-A},M_{0,V+A})-3\cdot C32(M_{0,V-A},M_{0,V+A})\}\\
A_{0,7} &= \frac{i}{\sqrt{6}}\{C1(M_{1,V-A},M_{0,V-A})-\frac{1}{2}\cdot C1(M_{0,V+A},M_{0,V-A})-\frac{3}{2}\cdot C4(M_{0,V-A},M_{0,V+A})\\
&+3\cdot C7(M_{0,V-A},M_{1,V-A})-\frac{3}{2}\cdot C7(M_{0,V-A},M_{0,V+A})-3\cdot C10(M_{1,V-A},M_{0,V-A})\\
&+\frac{3}{2}\cdot C10(M_{0,V+A},M_{0,V-A})+3\cdot C13(M_{0,V-A},M_{1,V-A})-\frac{3}{2}\cdot C13(M_{0,V-A},M_{0,V+A})\\
&-3\cdot C16(M_{1,V-A},M_{0,V-A})+\frac{3}{2}\cdot C16(M_{0,V+A},M_{0,V-A})-\frac{3}{2}\cdot C19(M_{0,V-A},M_{0,V+A})\\
&+\frac{3}{2}\cdot C21(M_{0,V-A},M_{0,V+A})+3\cdot C23(M_{0,V-A},M_{1,V-A})-\frac{3}{2}\cdot C23(M_{0,V-A},M_{0,V+A})\\
&-3\cdot C26(M_{1,V-A},M_{0,V-A})+\frac{3}{2}\cdot C26(M_{0,V+A},M_{0,V-A})-\frac{3}{2}\cdot C29(M_{0,V-A},M_{0,V+A})\\
&+\frac{3}{2}\cdot C31(M_{0,V-A},M_{0,V+A})\}\\
A_{0,8} &= \frac{i}{\sqrt{6}}\{-\frac{1}{2}\cdot C3(M_{0,V+A},M_{0,V-A})-\frac{3}{2}\cdot C6(M_{0,V-A},M_{0,V+A})+C2(M_{1,V-A},M_{0,V-A})\\
&+3\cdot C8(M_{0,V-A},M_{1,V-A})-\frac{3}{2}\cdot C9(M_{0,V-A},M_{0,V+A})-3\cdot C11(M_{1,V-A},M_{0,V-A})\\
&+\frac{3}{2}\cdot C12(M_{0,V+A},M_{0,V-A})+3\cdot C14(M_{0,V-A},M_{1,V-A})-\frac{3}{2}\cdot C15(M_{0,V-A},M_{0,V+A})\\
&-3\cdot C17(M_{1,V-A},M_{0,V-A})+\frac{3}{2}\cdot C18(M_{0,V+A},M_{0,V-A})-\frac{3}{2}\cdot C20(M_{0,V-A},M_{0,V+A})\\
&+\frac{3}{2}\cdot C22(M_{0,V-A},M_{0,V+A})+3\cdot C24(M_{0,V-A},M_{1,V-A})-\frac{3}{2}\cdot C25(M_{0,V-A},M_{0,V+A})\\
&-3\cdot C27(M_{1,V-A},M_{0,V-A})+\frac{3}{2}\cdot C28(M_{0,V+A},M_{0,V-A})-\frac{3}{2}\cdot C30(M_{0,V-A},M_{0,V+A})\\
&+\frac{3}{2}\cdot C32(M_{0,V-A},M_{0,V+A})\}\\
A_{0,9} &= \frac{i}{\sqrt{6}}\{C1(M_{1,V+A},M_{0,V-A})-\frac{1}{2}\cdot C1(M_{0,V-A},M_{0,V-A})-\frac{3}{2}\cdot C4(M_{0,V-A},M_{0,V-A})\\
&+3\cdot C7(M_{0,V-A},M_{1,V+A})-\frac{3}{2}\cdot C7(M_{0,V-A},M_{0,V-A})-3\cdot C10(M_{1,V+A},M_{0,V-A})\\
&+\frac{3}{2}\cdot C10(M_{0,V-A},M_{0,V-A})+3\cdot C13(M_{0,V-A},M_{1,V+A})-\frac{3}{2}\cdot C13(M_{0,V-A},M_{0,V-A})\\
&-3\cdot C16(M_{1,V+A},M_{0,V-A})+\frac{3}{2}\cdot C16(M_{0,V-A},M_{0,V-A})-\frac{3}{2}\cdot C19(M_{0,V-A},M_{0,V-A})\\
&+\frac{3}{2}\cdot C21(M_{0,V-A},M_{0,V-A})+3\cdot C23(M_{0,V-A},M_{1,V+A})-\frac{3}{2}\cdot C23(M_{0,V-A},M_{0,V-A})
\end{aligned}
$$

$$
\begin{aligned}
& -3\cdot C26(M_{1,V+A},M_{0,V-A})+\frac{3}{2}\cdot C26(M_{0,V-A},M_{0,V-A})-\frac{3}{2}C29(M_{0,V-A},M_{0,V-A}) \\
& +\frac{3}{2}\cdot C31(M_{0,V-A},M_{0,V-A})\} \\
A_{0,10} \;=\; & \frac{i}{\sqrt{6}}\{-\frac{1}{2}\cdot C3(M_{0,V-A},M_{0,V-A})-\frac{3}{2}\cdot C6(M_{0,V-A},M_{0,V-A})+C2(M_{1,V+A},M_{0,V-A}) \\
& +3\cdot C8(M_{0,V-A},M_{1,V+A})-\frac{3}{2}\cdot C9(M_{0,V-A},M_{0,V-A})-3\cdot C11(M_{1,V+A},M_{0,V-A}) \\
& +\frac{3}{2}\cdot C12(M_{0,V-A},M_{0,V-A})+3\cdot C14(M_{0,V-A},M_{1,V+A})-\frac{3}{2}\cdot C15(M_{0,V-A},M_{0,V-A}) \\
& -3\cdot C17(M_{1,V+A},M_{0,V-A})+\frac{3}{2}\cdot C18(M_{0,V-A},M_{0,V-A})-\frac{3}{2}\cdot C20(M_{0,V-A},M_{0,V-A}) \\
& +\frac{3}{2}\cdot C22(M_{0,V-A},M_{0,V-A})+3\cdot C24(M_{0,V-A},M_{1,V+A})-\frac{3}{2}\cdot C25(M_{0,V-A},M_{0,V-A}) \\
& -3\cdot C27(M_{1,V+A},M_{0,V-A})+\frac{3}{2}\cdot C28(M_{0,V-A},M_{0,V-A})-\frac{3}{2}\cdot C30(M_{0,V-A},M_{0,V-A}) \\
& +\frac{3}{2}\cdot C32(M_{0,V-A},M_{0,V-A})\}
\end{aligned}
$$

3.3 From Bare M_i on Lattice to M_i in $\overline{\rm MS}$ Scheme

Since the effective Hamiltonian is defined in the $\overline{\rm MS}$ scheme which is different from a bare lattice QCD formulation, these decay matrix elements are not directly accessible on lattice. The transformation is needed from $\langle\pi\pi|Q_i^{Lat}|K\rangle$ to $\langle\pi\pi|Q_i^{\overline{\rm MS}}|K\rangle$ (which will be described in later section).

The general procedure to obtain M_i in $\overline{\rm MS}$ scheme is summarized as in Table 3.2 (and will be explained in the following sub-sections):

M_i^{lat} (Bare M_i on finite volume Lattice)	
$\Downarrow$	LL Factor[19]
M_i in infinite volume, Minkowski space.	
$\Downarrow$	Lat$\rightarrow$RI/SMOM NPR matrix
M_i in RI/SMOM scheme	
$\Downarrow$	RI/SMOM$\rightarrow$ $\overline{\text{MS}}$ matching matrix
M_i in $\overline{\text{MS}}$ scheme	

Table 3.2: Work flow from bare lattice matrix elements to $\overline{\text{MS}}$ decay matrix elements.

3.3.1 LL factor

Though the bare decay matrix elements M_i^{lat} can be determined from The Euclidean three-point function $\langle J_{\pi\pi}(t_{\pi\pi})Q_i(t_Q)J_K(t_K)\rangle$, the *Maiani-Testa no-go theorem* states that M_i^{lat} is not equivalent to the corresponding infinite-volume Minkowski-space decay matrix elements[20]. Then Lellouch and Lüscher showed that there does exist a linear relation between these two quantities (this factor being LL factor), given that the calculation is done on a finite lattice and $\pi\pi$ energies are well separated.

To show the derivation of LL factor, let's first consider the $\pi\pi$ scattering without weak interaction and we assume the kaon state is degenerate with one $\pi\pi$ state with energy $E_{\pi\pi} = m_K$. According to Lüscher's quantization condition[21], the $\pi\pi$ scattering phase shift $\delta(p)$ is:

$$\delta(p) + \phi(q) = n\pi, \tag{3.55}$$

where the $\phi(q)$ function is analytic function that will be explained in Chapter 5, and p and

q are determined from:

$$E_{\pi\pi} = 2\sqrt{m_\pi + p^2} \tag{3.56}$$

$$q = \frac{pL}{2\pi} \tag{3.57}$$

If the weak interaction is turned on, it will make two changes to equation 3.55:

- The value of p changes because $\pi\pi$ now mixes with kaon.
- The phase shift function $\delta(p)$ changes because kaon is now a new resonance state in $\pi\pi$ scattering (i.e the process of $\pi\pi \to K \to \pi\pi$).

According to first order perturbation theory, the new energy eigenstates have energies of:

$$W = m_K \pm |M|, \tag{3.58}$$

where M is the weak matrix element on lattice. So the change in p is:

$$\Delta p = \frac{m_K}{4p}|M| \tag{3.59}$$

Now we can replace the $\delta(p)$ function by $\delta'(p)$, p by $p + \Delta p$ in equation 3.55, and then expand all terms in power of weak interaction. The leading terms will cancel, leaving only the first order terms:

$$\Delta p \frac{\partial \delta(k)}{\partial k}|_{k=p} - \frac{p|A|^2}{32\pi m_K^2 |M|} = -\Delta p \frac{\partial \phi(kL/2\pi)}{\partial k}|_{k=p} \tag{3.60}$$

So the infinite-volume Minkowski decay amplitude is related to the lattice matrix element by:

$$|A|^2 = 8\pi\{\frac{kL}{2\pi}\frac{\partial\phi(kL/2\pi)}{\partial(kL/2\pi)} + k\frac{\partial\delta(k)}{\partial k}\}|_{k=p}\left(\frac{m_K}{p}\right)^3 |M|^2 \tag{3.61}$$

To write it in a more concise way:

$$A = \frac{1}{\pi q}\sqrt{\frac{\partial\phi}{\partial q} + \frac{\partial\delta}{\partial q}}\sqrt{m_K}E_{\pi\pi}L^{2/3}M \tag{3.62}$$

It's understood that the partial derivative in above equation is evaluated at the kinematic point as in Equation 3.57. The factor in front of M is the Lellouch-Lüscher (LL) factor [19][22]. To get the LL factor, we evaluate the ϕ function and its derivative numerically, and we used a linear approximation to evaluate the partial derivative of δ: $\partial\delta/\partial p \approx \delta/p$ at small p.

Although the LL factor relates the matrix elements in finite and infinite volume, it's not the complete finite volume correction. The latter is about examining the effect of replacing the momentum integration by Poisson summation, which is a separate topic. While the LL factor gives the leading $1/L^2$ corrections, there are also exponential corrections $\sim e^{-m_\pi L}$ which can be estimated using chiral perturbation theory.

3.3.2 Non-perturbative Renormalization (NPR)

After we have calculated the lattice matrix elements in infinite volume, the next step is to build the decay amplitude $\langle\pi\pi|H_W|K\rangle$ from those matrix elements. This is not trivial because we don't know the Wilson coefficient needed to multiply each of the bare lattice $\Delta S = 1$ operator. Instead we must use the Wilson coefficients that have been calculated in the $\overline{\text{MS}}$[9], and then determine the conversion relation which transforms the operators from lattice theory to those in the $\overline{\text{MS}}$ scheme, at the same energy scale where the Wilson coefficients are calculated.

In order to determine the conversion relation, we use an intermediate renormalization scheme (the regularization-independent scheme, or RI scheme):

$$Q_i^{\overline{\text{MS}}} = Z_{ij}^{RI\to\overline{\text{MS}}}Q_j^{RI} = Z_{ij}^{RI\to\overline{\text{MS}}}Z_{jk}^{Lat\to RI}Q_k^{Lat}, \tag{3.63}$$

where Q_k^{Lat} is the bare lattice matrix operator (in the following text, Q_k stands for Q_k^{Lat} by default). The conversion matrix $Z^{RI\to\overline{\rm MS}}$ is worked out in [23]. The other matrix $Z^{Lat\to RI}$ is obtained from an additional lattice calculation. The renormalization condition of RI scheme requires that the amputated Green's function containing the RI operators with given external momentum eigenstates take on their tree level values:

$$P_j\Gamma^{RI}(Q_i^{RI}) = P_j\Gamma^{tree}(Q_i), \tag{3.64}$$

where the P_j are projector operators in spin, color, and flavor space; $\Gamma(Q_i)$ is the amputated Green's function Γ containing the operator Q_i, and the superscript *tree* means evaluated at tree level or in the $\alpha_s \to 0$ limit. The renormalized amputated Green's function Γ^{RI} is related to the bare amputated Green's function Γ by:

$$\Gamma^{RI}(Q_i^{RI}) = \frac{1}{(Z_q)^2} Z_{ij}^{Lat\to RI}\Gamma(Q_j), \tag{3.65}$$

where Z_q is the quark wave function renormalization constant. Combining equation (3.64) and (3.65), the $Z^{Lat\to RI}$ matrix is:

$$Z_{ij}^{Lat\to RI} = \sum_k (Z_q)^2 (P_k\Gamma^{tree}(Q_i))(M^{-1})_{kj}, \tag{3.66}$$

where

$$M_{ij} \;=\; P_j\Gamma(Q_i) \tag{3.67}$$

The matrix $(P_k\Gamma^{tree}(Q_i))$ can be worked out by hand, while Z_q and the matrix M are calculated on the lattice. The tree level results are in Table 3.3 and 3.4.

3072	3072	0	0	0	0	0
537.6	-230.4	1152	0	0	0	0
-230.4	537.6	384	0	0	0	0
0	0	0	1152	384	3456	1152
0	0	0	384	1152	1152	3456
0	0	0	1152	384	0	0
0	0	0	384	1152	0	0

Table 3.3: Tree level mixing matrix (parity-even or parity-odd) $F_{ij} = P_j\Gamma^{tree}(Q_i)$, using γ_μ projectors $\{P_j\}$.

768						
	134.4	-57.6	0	0		
	-57.6	134.4	0	0		
	0	0	288	96		
	0	0	96	288		
					288	96
					96	288

Table 3.4: Tree level mixing matrix (parity-even or parity-odd) $F_{ij} = P_j\Gamma^{tree}(Q_i)$, using $\not{q}$ projectors $\{P_j\}$. The elements outside the three sub-blocks are not considered since the NPR is done separately for the three sub-blocks.

The set of operators used are the chiral basis Q'_{1-7}:

$$Q'_1 = 3Q_1 + 2Q_2 - Q_3 \tag{3.68a}$$

$$Q'_2 = (2Q_1 - 2Q_2 + Q_3)/5 \tag{3.68b}$$

$$Q'_3 = (-3Q_1 + 3Q_2 + Q_3)/5 \tag{3.68c}$$

$$Q'_4 = Q_5 \tag{3.68d}$$

$$Q'_5 = Q_6 \tag{3.68e}$$

$$Q'_6 = Q_7 \tag{3.68f}$$

$$Q'_7 = Q_8 \tag{3.68g}$$

where the right hand side Q_{1-10} are from Equation 2.40. These 7 operators are in three irreducible representations of the chiral flavor-symmetry group $SU(3)_L \otimes SU(3)_R$:

$$\begin{array}{cc} (27,1) & Q'_1 \\ (8,1) & Q'_{2,3,4,5} \\ (8,8) & Q'_{6,7} \end{array}$$

QCD interaction doesn't mix these three groups with each other in the chiral limit. Depending on the projectors used to define Z_q and matrix M, there are four different RI schemes: (γ_μ, γ_μ), $(\gamma_\mu, \not{q})$, $(\not{q}, \gamma_\mu)$, $(\not{q}, \not{q})$, where the first $\gamma_\mu/\not{q}$ corresponds to the set of projectors P_i and second $\gamma_\mu/\not{q}$ denotes the scheme for wave function renormalization.

Parity transformation can be used to show that the projectors P_i can be defined using either the parity even part or equivalently the parity odd part. For simplicity, all the projectors are expressed in terms of:

$$P^{VV\pm AA,\gamma_\mu}_{(1),f'} = \delta_{ff'}\delta_{ij}\delta_{kl} \times [(\gamma_\nu)_{\beta\alpha}(\gamma^\nu)_{\delta\gamma} \pm (\gamma_5\gamma_\nu)_{\beta\alpha}(\gamma_5\gamma^\nu)_{\delta\gamma}] \tag{3.69a}$$

$$P^{VV\pm AA,\gamma_\mu}_{(2),f'} = \delta_{ff'}\delta_{il}\delta_{kj} \times [(\gamma_\nu)_{\beta\alpha}(\gamma^\nu)_{\delta\gamma} \pm (\gamma_5\gamma_\nu)_{\beta\alpha}(\gamma_5\gamma_\nu)_{\delta\gamma}] \tag{3.69b}$$

$$P^{\pm VA-AV,\gamma_\mu}_{(1),f'} = \delta_{ff'}\delta_{ij}\delta_{kl} \times [\pm(\gamma_\nu)_{\beta\alpha}(\gamma_5\gamma_\nu)_{\delta\gamma} - (\gamma_5\gamma_\nu)_{\beta\alpha}(\gamma_\nu)_{\delta\gamma}] \tag{3.69c}$$

$$P^{\pm VA-AV,\gamma_\mu}_{(2),f'} = \delta_{ff'}\delta_{il}\delta_{kj} \times [\pm(\gamma_\nu)_{\beta\alpha}(\gamma_5\gamma_\nu)_{\delta\gamma} - (\gamma_5\gamma_\nu)_{\beta\alpha}(\gamma_\nu)_{\delta\gamma}] \tag{3.69d}$$

$$P^{VV\pm AA,\not{q}}_{(1),f'} = \delta_{ff'}\delta_{ij}\delta_{kl} \times [(\not{q})_{\beta\alpha}(\not{q})_{\delta\gamma} \pm (\gamma_5\not{q})_{\beta\alpha}(\gamma_5\not{q})_{\delta\gamma}]/q^2 \tag{3.69e}$$

$$P^{VV\pm AA,\not{q}}_{(2),f'} = \delta_{ff'}\delta_{il}\delta_{kj} \times [(\not{q})_{\beta\alpha}(\not{q})_{\delta\gamma} \pm (\gamma_5\not{q})_{\beta\alpha}(\gamma_5\not{q})_{\delta\gamma}]/q^2 \tag{3.69f}$$

$$P^{\pm VA-AV,\not{q}}_{(1),f'} = \delta_{ff'}\delta_{ij}\delta_{kl} \times [\pm(\not{q})_{\beta\alpha}(\gamma_5\not{q})_{\delta\gamma} - (\gamma_5\not{q})_{\beta\alpha}(\not{q})_{\delta\gamma}]/q^2 \tag{3.69g}$$

$$P^{\pm VA-AV,\not{q}}_{(2),f'} = \delta_{ff'}\delta_{il}\delta_{kj} \times [\pm(\not{q})_{\beta\alpha}(\gamma_5\not{q})_{\delta\gamma} - (\gamma_5\not{q})_{\beta\alpha}(\not{q})_{\delta\gamma}]/q^2, \tag{3.69h}$$

where the $\alpha, \beta, \delta, \gamma$ are the 4 spin indices, i, j, k, l are the corresponding 4 color indices. These indices are to be contracted with the amputated Green's function, shown in Figure (3.2).

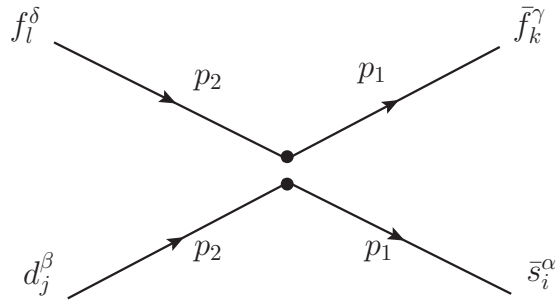

Figure 3.2: Open indices for the four-quark Green's function Γ.

The P_i in $RI(\gamma_\mu, *)$ schemes are:

$$P_1^{even,\gamma_\mu} = P_{(1),u}^{VV+AA,\gamma_\mu} \tag{3.70a}$$

$$P_2^{even,\gamma_\mu} = P_{(2),u}^{VV+AA,\gamma_\mu} \tag{3.70b}$$

$$P_3^{even,\gamma_\mu} = P_{(1),u}^{VV+AA,\gamma_\mu} + P_{(1),d}^{VV+AA,\gamma_\mu} + P_{(1),s}^{VV+AA,\gamma_\mu} \tag{3.70c}$$

$$P_4^{even,\gamma_\mu} = P_{(1),u}^{VV-AA,\gamma_\mu} \tag{3.70d}$$

$$P_5^{even,\gamma_\mu} = P_{(2),u}^{VV-AA,\gamma_\mu} \tag{3.70e}$$

$$P_6^{even,\gamma_\mu} = P_{(1),u}^{VV-AA,\gamma_\mu} + P_{(1),d}^{VV-AA,\gamma_\mu} + P_{(1),s}^{VV-AA,\gamma_\mu} \tag{3.70f}$$

$$P_7^{even,\gamma_\mu} = P_{(2),u}^{VV-AA,\gamma_\mu} + P_{(2),d}^{VV-AA,\gamma_\mu} + P_{(2),s}^{VV-AA,\gamma_\mu}, \tag{3.70g}$$

for the parity even part and

$$P_1^{odd,\gamma_\mu} = P_{(1),u}^{-VA-AV,\gamma_\mu} \tag{3.71a}$$

$$P_2^{odd,\gamma_\mu} = P_{(2),u}^{-VA-AV,\gamma_\mu} \tag{3.71b}$$

$$P_3^{odd,\gamma_\mu} = P_{(1),u}^{-VA-AV,\gamma_\mu} + P_{(1),d}^{-VA-AV,\gamma_\mu} + P_{(1),s}^{-VA-AV,\gamma_\mu} \tag{3.71c}$$

$$P_4^{odd,\gamma_\mu} = P_{(1),u}^{VA-AV,\gamma_\mu} \tag{3.71d}$$

$$P_5^{odd,\gamma_\mu} = P_{(2),u}^{VA-AV,\gamma_\mu} \tag{3.71e}$$

$$P_6^{odd,\gamma_\mu} = P_{(1),u}^{VA-AV,\gamma_\mu} + P_{(1),d}^{VA-AV,\gamma_\mu} + P_{(1),s}^{VA-AV,\gamma_\mu} \tag{3.71f}$$

$$P_7^{odd,\gamma_\mu} = P_{(2),u}^{VA-AV,\gamma_\mu} + P_{(2),d}^{VA-AV,\gamma_\mu} + P_{(2),s}^{VA-AV,\gamma_\mu}, \tag{3.71g}$$

for the parity odd part. The P_i in $RI(\not{q},*)$ schemes are:

$$P_1^{even,\not{q}} = P_{(1),u}^{VV+AA,\not{q}} \tag{3.72a}$$

$$P_2^{even,\not{q}} = P_{(1),u}^{VV+AA,\not{q}} \tag{3.72b}$$

$$P_3^{even,\not{q}} = P_{(2),u}^{VV+AA,\not{q}} \tag{3.72c}$$

$$P_4^{even,\not{q}} = P_{(1),u}^{VV-AA,\not{q}} \tag{3.72d}$$

$$P_5^{even,\not{q}} = P_{(2),u}^{VV-AA,\not{q}} \tag{3.72e}$$

$$P_6^{even,\not{q}} = P_{(1),u}^{VV-AA,\not{q}} \tag{3.72f}$$

$$P_7^{even,\not{q}} = P_{(2),u}^{VV-AA,\not{q}}, \tag{3.72g}$$

for the parity even part and

$$P_1^{odd,\not{q}} = P_{(1),u}^{-VA-AV,\not{q}} \tag{3.73a}$$
$$P_2^{odd,\not{q}} = P_{(1),u}^{-VA-AV,\not{q}} \tag{3.73b}$$
$$P_3^{odd,\not{q}} = P_{(2),u}^{-VA-AV,\not{q}} \tag{3.73c}$$
$$P_4^{odd,\not{q}} = P_{(1),u}^{VA-AV,\not{q}} \tag{3.73d}$$
$$P_5^{odd,\not{q}} = P_{(2),u}^{VA-AV,\not{q}} \tag{3.73e}$$
$$P_6^{odd,\not{q}} = P_{(1),u}^{VA-AV,\not{q}} \tag{3.73f}$$
$$P_7^{odd,\not{q}} = P_{(2),u}^{VA-AV,\not{q}}, \tag{3.73g}$$

for the parity odd part. As an example, when calculating the matrix element M_{11} in the parity-even $(\gamma_\mu, *)$ scheme, we first evaluate the correlation function:

$$\langle A\rangle^{\alpha\beta\gamma\delta,ijkl} = \langle Q_1'(x)e^{-i2(p_2-p_1)x}s_i^\alpha(p_1)\bar{d}_j^\beta(p_2)u_k^\gamma(p_1)\bar{u}_l^\delta(p_2)\rangle. \tag{3.74}$$

Note that we only need the parity-even part of Q_1' because the projectors are parity-even and the lattice formulation preserves parity. Then the amputated Green's function is:

$$[\langle A\rangle]_{amp}^{\alpha\beta\gamma\delta,ijkl} = \langle A\rangle^{\alpha'\beta'\gamma'\delta',i'j'k'l'}(\gamma_5 S^\dagger(p_1)\gamma_5)^{-1}_{\alpha'i',\alpha i}(\gamma_5 S^\dagger(p_1)\gamma_5)^{-1}_{\gamma'k',\gamma k}(S(p_2))^{-1}_{\beta'j',\beta j}(S(p_2))^{-1}_{\delta'l',\delta l}, \tag{3.75}$$

note that γ_5-Hermiticity:

$$S(x;y)^\dagger = \gamma_5 S(y;x)\gamma_5, \tag{3.76}$$

has been used to switch the source and sink. $S(p)$ is the momentum-source-momentum-sink

propagator, with momentum p. Finally the matrix elements M_{11} is:

$$M_{11} = P_1\Gamma(Q_1') = [\langle A\rangle]^{\alpha\beta\gamma\delta,ijkl}_{amp} \times \delta_{ij}\delta_{kl} \times [(\gamma_\nu)_{\beta\alpha}(\gamma^\nu)_{\delta\gamma} + (\gamma_5\gamma_\nu)_{\beta\alpha}(\gamma_5\gamma^\nu)_{\delta\gamma}]. \tag{3.77}$$

Until now we haven't considered the mixing between the dimension-6 operator and other lower dimension operator. In this work, we considered the following dimension-3 and dimension-4 operators:

$$\begin{aligned} B_1 &= \bar{s}d + \bar{s}\gamma_5 d & (3.78)\\ B_2 &= \bar{s}(-\overleftarrow{\not{D}} + \overrightarrow{\not{D}})d + \bar{s}(-\overleftarrow{\not{D}} + \overrightarrow{\not{D}})\gamma_5 d & (3.79)\\ B_3 &= \bar{s}(\overleftarrow{\not{D}} + \overrightarrow{\not{D}})d + \bar{s}(\overleftarrow{\not{D}} + \overrightarrow{\not{D}})\gamma_5 d & (3.80) \end{aligned}$$

The choice is from Ref [18]. We use three renormalization parameters for each of the subtracted dimension-6 operator:

$$Q_i^{'sub} = Q_i' + C_{i1}B_1 + C_{i2}B_2 + C_{i3}B_3 \tag{3.81}$$

The three subtraction coefficients are determined from the three renormalization conditions:

$$\begin{aligned} \Big(\langle Q_k^{'sub}(x)e^{-i(p_2-p_1)x}s(p_1)\bar{d}(p_2)\rangle_{amp}\Big)^{\alpha\beta,ij} \times \delta_{ij} \times \Gamma_{\alpha\beta} &= 0 & (3.82)\\ \Big((\not{p}_1' + \not{p}_2')\langle Q_k^{'sub}(x)e^{-i(p_2-p_1)x}s(p_1)\bar{d}(p_2)\rangle_{amp}\Big)^{\alpha\beta,ij} \times \delta_{ij} \times \Gamma_{\alpha\beta} &= 0 & (3.83)\\ \Big((\not{p}_1' - \not{p}_2')\langle Q_k^{'sub}(x)e^{-i(p_2-p_1)x}s(p_1)\bar{d}(p_2)\rangle_{amp}\Big)^{\alpha\beta,ij} \times \delta_{ij} \times \Gamma_{\alpha\beta} &= 0, & (3.84) \end{aligned}$$

where $\Gamma = \mathbb{1}_{4\times4}$ if we are using parity-even projectors and $\Gamma = \gamma_5$ if we are using parity-odd projectors.

The wave function renormalization constant Z_q is computed by imposing the RI renormalization condition on the quark bilinear operator [24] (take Z_q in the γ_μ scheme with a

parity-even projector, as an example):

$$\frac{1}{48}Tr[\Lambda^{\mu}_{V,R}(p_1,p_2)\gamma_{\mu}] = 1 \tag{3.85}$$

$$\Lambda^{\mu}_{V,R}(p_1,p_2) = \frac{Z_V}{Z_q}\Lambda^{\mu}_{V,B}(p_1,p_2), \tag{3.86}$$

where $\Lambda^{\mu}_{V,B}(p_1,p_2)$ is the amputated Green function for bare vector current operator:

$$[\Lambda^{\mu}_{V,B}(p_1,p_2)]^{\alpha\beta,ij} = \langle \bar{f}(x)\gamma^{\mu}f(x)e^{-i(p_2-p_1)x}f(p_1)\bar{f}(p_2)\rangle^{\alpha'\beta',i'j'}(\gamma_5 S^{\dagger}(p_1)\gamma_5)^{-1}_{\alpha'i',\alpha i}(S(p_2))^{-1}_{\beta'j',\beta j},$$

and the index B and R denote the bare quantity and the renormalized quantity respectively, and Z_V is the renormalization constant for the local vector current (and Z_A for axial-vector current similarly). Combining Equations 3.85 and 3.86, Z_q is:

$$Z_q = Z_V * (\frac{1}{48}Tr[\Lambda^{\mu}_{V,B}(p_1,p_2)\gamma_{\mu}]) \equiv Z_V * \Lambda_V \tag{3.87}$$

Similarly Z_q could be defined using Z_A and axial-vector quark bilinear operator:

$$Z_q = Z_A * (\frac{1}{48}Tr[\Lambda^{\mu}_{A,B}(p_1,p_2)\gamma_{\mu}]) \equiv Z_A * \Lambda_A \tag{3.88}$$

In this work, I take the average of the two parity components to compute Z_q:

$$Z_q = \frac{1}{2}(Z_V * \Lambda_V + Z_A * \Lambda_A), \tag{3.89}$$

where the Z_V and Z_A value are taken from [25]. The full NPR results in this work are measured on 100 configurations from the 2+1 flavor ensemble, with lattice size $32^3 \times 64$ and the IDSDR gauge action at $\beta = 1.75$ [1]. The results are given in Tables C.1 and C.2

As can be seen from the procedure, the 7-by-7 $Z^{Lat\to RI} = (Z_q)^2(P\Gamma^{tree}(Q))(M^{-1})$ matrix depends on the set of projectors we use. However the $Z^{RI\to\overline{\text{MS}}}$ matching matrix also depends

on the set of projectors and the net effect is that the matching matrix from lattice to $\overline{\rm MS}$, $Z_{ij}^{Lat\to\overline{\rm MS}} = Z_{ij}^{RI\to\overline{\rm MS}} Z_{jk}^{Lat\to RI}$, is independent of our choice of projectors, up to the higher order terms that are neglected in the perturbation theory calculation of the $Z^{RI\to\overline{\rm MS}}$ matrix.

To evaluate the systematic error in the NPR matching procedure, we computed the set of 7 bare lattice Wilson coefficients C_i^{Lat} in front of the 7 linear-independent operators:

$$H_W^{\Delta S=1} = \frac{G_F}{\sqrt{2}} V_{us}^* V_{ud} \sum_{i=1} C_i^{Lat} Q_i^{Lat},\ i \in \{1,2,3,5,6,7,8\}, \tag{3.90}$$

using the four different intermediate RI schemes. Note that the set $\{Q_i | i = 1,2,3,5,6,7,8\}$ is not the chiral basis, it is related to the 7-operator chiral basis by Equation 3.68. The results for all four schemes C_i^{Lat} are given in Table C.4 and C.5. In Table C.6 we give the difference between the (γ_μ, γ_μ) and $(\not{q}, \not{q})$ schemes with jackknife errors which we use to estimate the systematic error in the $Lat \to \overline{\rm MS}$ operator matching procedure.

3.4 Computing Wilson Coefficients

The Wilson coefficients in the $\overline{\rm MS}$ scheme are calculated in [9]. The procedure is complicated and it needs special care to properly omit terms of higher order terms in α, α_s. Here we just show the procedure of calculating α_s using the two-loop running coupling formula in [9]:

$$\alpha_s^{(f)}(\mu) = \frac{4\pi}{\beta_0^{(f)} \ln(\mu^2/\Lambda_f^2)} [1 - \frac{\beta_1^{(f)}}{{\beta_0^{(f)}}^2} \frac{\ln(\ln(\mu^2/\Lambda_f^2))}{\ln(\mu^2/\Lambda_f^2)}], \tag{3.91}$$

where

$$\beta_0^{(f)} = \frac{11N - 2f}{3} \tag{3.92}$$

$$\beta_1^{(f)} = \frac{34}{3} N^2 - \frac{10}{3} Nf - 2C_F f \tag{3.93}$$

$$C_F = \frac{N^2 - 1}{2N}, \tag{3.94}$$

and N is the number of colors, f is the number of active quark flavors. The other unknown parameter Λ_f in Equation 3.91 is determined from the matching condition:

$$\alpha_s^{(5)}(M_z) = 0.1185 \tag{3.95}$$

$$\alpha_s^{(5)}(m_b) = \alpha_s^{(4)}(m_b) \tag{3.96}$$

$$\alpha_s^{(4)}(m_c) = \alpha_s^{(3)}(m_c) \tag{3.97}$$

The Z-boson mass and $\alpha_s^{(5)}(M_z)$ are input from PDG booklet [26] . From the above three conditions, $\Lambda_f(f = 3, 4, 5)$ are determined. The result for $\alpha_s^{(3)}(\mu = 1.53\text{GeV})$ is then calculated and used in calculating $\overline{\text{MS}}$ Wilson coefficients at 1.53 GeV.

Chapter 4

Measurement Methods

In this chapter we discuss the details of several measurement techniques, including G-parity boundary conditions and all-to-all propagators. The G-parity boundary conditions give physical relative momenta to the pions in the final $I = 0$ state, while the all-to-all propagators suppresses fluctuation in vacuum diagrams and reduce propagator inversion.

4.1 G-parity boundary condition

In the physical $K \to \pi\pi$ decay, each of the two pions in the final state carries a non-zero momentum. This results in a large difficulty if we use periodic boundary conditions. In that case the single pion ground state has zero momentum and two-pion ground state is much lighter than kaon mass. G-parity boundary conditions provide a solution because a pion acquires a minus sign under the G-parity transformation. In other words, pions will satisfy anti-periodic boundary conditions if G-parity boundary conditions are imposed on the quark. So the single pion state with momentum $p = 0$ is eliminated and it now carries at least one half the lattice momentum $\frac{1}{2} \times \frac{2\pi}{L}$.

A G-parity transformation is a combination of an isospin rotation by 180 degrees about

the y-axis and charge conjugation. When applying to quark and anti-quark field operators:

$$\hat{G}\begin{pmatrix} u \\ d \end{pmatrix} = \hat{C}e^{-i\pi\hat{I}_y}\begin{pmatrix} u \\ d \end{pmatrix} = \hat{C}\begin{pmatrix} 0 & -1 \\ 1 & 0 \end{pmatrix}\begin{pmatrix} u \\ d \end{pmatrix} = \begin{pmatrix} -C\bar{d}^T \\ C\bar{u}^T \end{pmatrix} \tag{4.1}$$

$$\hat{G}\begin{pmatrix} \bar{d} \\ \bar{u} \end{pmatrix} = \hat{C}e^{-i\pi\hat{I}_y}\begin{pmatrix} \bar{d} \\ \bar{u} \end{pmatrix} = \hat{C}\begin{pmatrix} 0 & -1 \\ 1 & 0 \end{pmatrix}\begin{pmatrix} \bar{d} \\ \bar{u} \end{pmatrix} = \begin{pmatrix} -u^T C^{-1} \\ d^T C^{-1} \end{pmatrix}, \tag{4.2}$$

where C, in our conventions, is $-\gamma_2\gamma_4$. The SU(2) isospin symmetry is preserved by G-parity transformation and three pion states are all G-parity odd:

$$\hat{G}(\hat{\pi}^+) = -\hat{\pi}^+ \tag{4.3}$$

$$\hat{G}(\hat{\pi}^-) = -\hat{\pi}^- \tag{4.4}$$

$$\hat{G}(\hat{\pi}^0) = -\hat{\pi}^0 \tag{4.5}$$

So the corresponding components of the momenta of the pions are $(2n+1)/L$, where n is an integer and L is the spatial size of the lattice. The ground state pion will carry the momentum of magnitude $\sqrt{n_{tw}} \cdot \pi/L$ where n_{tw} is the number of G-parity boundary twists, the number of spatial directions in which G-parity boundary conditions are imposed. The number of G-parity boundary twists and the volume of the lattice have been chosen so that the energy of the two-pion (I=0) ground state $E_{\pi\pi}$ is very close to the kaon mass M_K, which corresponds to the physical decay that we are trying to achieve.

These physical kinematics do not come for free. In the first place G-parity boundary conditions make the evolution of the gauge ensemble slow, since they make the fermion determinant (see Equation 3.9) hard to evaluate. The usual pseudo-fermion method (see Chapter 16 of Ref [16]) in Hybrid Monte Carlo algorithms is no longer easy to use since the up and down quark are now combined into one flavor in the fermion determinant, while the pseudo-fermion method only works if there are even number of equivalent quark flavors

(another method called Rational Hybrid Monte Carlo [27] is therefore needed for the light quarks). Besides the difficulty in gauge field evolution, G-parity boundary conditions also introduce several difficulties to measurements. These include:

- Extra Wick contractions
- Broken cubic symmetry
- Special treatment for the kaon

4.1.1 Extra wick contraction

Extra Wick contractions are needed because the G-parity transformation mixes the two isospin partners. As a simple example, the pion correlation function becomes:

$$\langle \pi\pi \rangle = \bar{u}\gamma_5 d \quad \bar{d}\gamma_5 u + \bar{u}\gamma_5 d \quad \bar{d}\gamma_5 u \ , \tag{4.6}$$

where the first term is the usual contraction term, while the second term arises because the quark lines could cross the G-parity boundary. Thus a d quark could change flavor and contract with a u quark as shown in Figure (4.1). This extra contraction will not change the SU(2) isospin quantum number since u and d have the opposite isospin. Because the G-parity boundary mixes the two quark flavors, the number of possible Wick contractions grows rapidly as the correlation function becomes more complicated. For example, the $\langle \pi\pi | H_w | K \rangle$ matrix element could contain as many as 256 different contractions.

4.1.2 Broken cubic symmetry

G-parity boundary conditions also put constraints on the quarks' momenta, which break the usual lattice cubic symmetry. With G-parity boundary conditions, quarks will satisfy

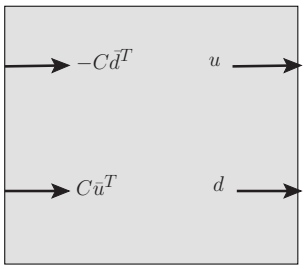

Figure 4.1: G-parity boundary mixes the two quark flavors.

anti-periodic boundary conditions in a double-sized lattice, since

$$u(x+2L) = -\gamma_4\gamma_2\bar{d}^T(x+L) = -u(x), \tag{4.7}$$

which constrains the quark's momentum to be in the form of $(n+\frac{1}{2})\frac{\pi}{L}$, with n an integer, in each of the spatial directions with G-parity boundary conditions. Besides that constraint, there is also constraint on the momentum direction. This can be seen by writing down a quark field which is momentum eigenstate. A momentum eigenstate is defined by:

$$T_z\widetilde{\psi}(p_z)T_z^{-1} = e^{ip_z}\widetilde{\psi}(p_z), \tag{4.8}$$

using the two-component field notation introduced by Chris Kelly, combining the two SU(2) flavors into a two-component fermion field: $\psi = \begin{pmatrix} \psi^{(0)} \\ \psi^{(1)} \end{pmatrix} = \begin{pmatrix} d \\ C\bar{u}^T \end{pmatrix}$. The field ψ transforms when passing through the G-parity boundary as:

$$\psi(L_z) = i\sigma_2\psi(0) \tag{4.9a}$$

$$\bar{\psi}(L_z) = -i\bar{\psi}(0)\sigma_2, \tag{4.9b}$$

And the translation operator T_z shifts the field operator by one unit:

$$T_z\psi(z)T_z^{-1} = \psi(z-1). \tag{4.10}$$

The definition given in Equations 4.9 and 4.10 are dictated by the requirement that the fermion action is invariant under translation.

The quark field with the momentum p_z is then given by:

$$\widetilde{\psi}(p_z) = \sum_{n_z=0}^{L_z-1} \{e^{-ip_z n_z}\psi(n_z) + i\sigma_2 e^{-ip_z(n_z+L_z)}\psi(n_z)\} \tag{4.11}$$

$$= (1 + ie^{-ip_z L_z}\sigma_2) \sum_{n_z=0}^{L_z-1} \{e^{-ip_z n_z}\psi(n_z)\}. \tag{4.12}$$

Translating in z-direction by one unit, the two components just to the left and right of the G-parity boundary in equation (4.11) will transform into each other, with the overall phase factor as in equation (4.8). Using $p_z = (n_z + \frac{1}{2})\frac{\pi}{L}$, equation (4.11) becomes

$$\widetilde{\psi}(p_z) = (1 + (-1)^{n_z}\sigma_2) \sum_{n_z=0}^{L_z-1} \{e^{-ip_z n_z}\psi(n_z)\} \tag{4.13}$$

With three G-parity twists, the prefactor in equation (4.13) changes from $(1 + (-1)^{n_z}\sigma_2)$ to $(1 + (-1)^{n_x}\sigma_2)(1 + (-1)^{n_y}\sigma_2)(1 + (-1)^{n_z}\sigma_2)$. Since $(1 - \sigma_2)$ is orthogonal to $(1 + \sigma_2)$, all the n_x, n_y, n_z must have the same parity, otherwise $\widetilde{\psi}(p_z)$ vanishes. Figure (4.2) shows the constraint that the G-parity boundary puts on the quark momentum.

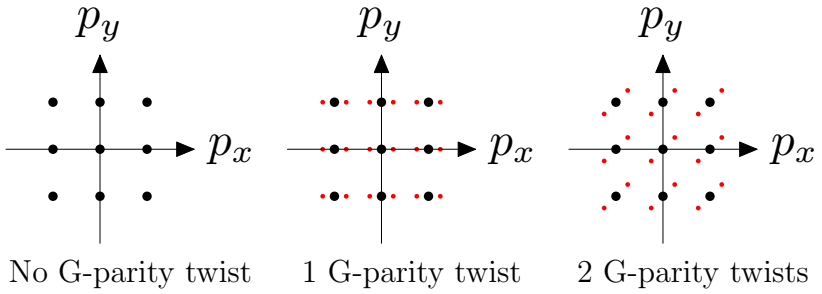

Figure 4.2: Large black dots: allowed quark momentums with periodic boundary conditions; small red dots: allowed quark momentums with G-parity boundary conditions.

A consequence of this momentum constraint is that the cubic symmetry of the fermion action is broken. Fortunately this doesn't break the cubic symmetry of pion operator sig-

nificantly. Even though the quarks are required to carry momenta only in the 'diagonal' direction as shown in Figure (4.2), the pion's momentum is not constrained in this way and G-parity boundary conditions are the same as anti-periodic boundary conditions for the pion. Given a pion momentum, there are multiple ways to distribute the momentum between the pion's two quark components. In this work, two different quark momenta configurations are averaged for each unique pion momentum as in Table 4.1.

Pion momentum	quark momenta, choice 1	quark momenta, choice 2
(2, 0, 0)	(1, 0, 0) + (1, 0, 0)	(-1, 0, 0) + (3, 0, 0)
(-2, 0, 0)	(-1, 0, 0) + (-1, 0, 0)	(1, 0, 0) + (-3, 0, 0)
(2, 2, 0)	(1, 1, 0) + (1, 1, 0)	(-1,-1, 0) + (3, 3, 0)
(-2,-2, 0)	(-1,-1, 0) + (-1,-1, 0)	(1, 1, 0) + (-3,-3, 0)
(-2, 2, 0)	(1, 1, 0) + (-3, 1, 0)	(-1,-1, 0) + (-1, 3, 0)
(2,-2, 0)	(-1,-1, 0) + (3,-1, 0)	(1, 1, 0) + (1,-3, 0)
(2, 2, 2)	(1, 1, 1) + (1, 1, 1)	(-1,-1,-1) + (3, 3, 3)
(-2,-2,-2)	(-1,-1,-1) + (-1,-1,-1)	(1, 1, 1) + (-3,-3,-3)
(-2, 2, 2)	(1, 1, 1) + (-3, 1, 1)	(-1,-1,-1) + (-1, 3, 3)
(2,-2,-2)	(-1,-1,-1) + (3,-1,-1)	(1, 1, 1) + (1,-3,-3)
(2,-2, 2)	(1, 1, 1) + (1,-3, 1)	(-1,-1,-1) + (3,-1, 3)
(-2, 2,-2)	(-1,-1,-1) + (-1, 3,-1)	(1, 1, 1) + (-3, 1,-3)
(2, 2,-2)	(1, 1, 1) + (1, 1,-3)	(-1,-1,-1) + (3, 3,-1)
(-2,-2, 2)	(-1,-1,-1) + (-1,-1, 3)	(1, 1, 1) + (-3,-3, 1)

Table 4.1: quark momenta used to construct pion momentum eigenstate. Upper part: one spatial G-parity boundary; Middle part: two spatial G-parity boundaries; Lower part: three spatial G-parity boundaries. All numbers are in units of $\frac{\pi}{2L}$. The final pion momentum eigenstate we use is the average of choice 1 and choice 2.

As can be seen from the Table 4.1, the cubic symmetry breaking at the quark level affects the pion operator in a subtle way: pion operators with diagonal momentum (the (2,2,2) entry and (-2,-2,-2) entry) can have two quarks each carrying the same momentum, while pion operators with off-diagonal momentum can't. The subtle difference in the quark composition of pion momentum eigenstates is caused by the G-parity boundary conditions and should be exponentially suppressed when the lattice volume becomes large, due to the short distance nature of the strong interaction. The reason to use the average of 2 quark

momenta distribution for every pion momentum is to further reduce this cubic symmetry breaking effect at pion level.

On the $32^3 \times 64$ ensemble that we are using, that single pion states with minimal momenta are all degenerate as can be seen from Table 4.2. So we are unable to see any evidence of this cubic symmetry breakdown.

	p=(2,2,2)	p=(-2,2,2)	p=(2,-2,2)	p=(2,2,-2)
E_π	0.19852(85)	0.19823(82)	0.19839(72)	0.19866(88)
Z_π	6.167(69)e+06	6.081(63)e+06	6.183(50)e+06	6.170(61)e+06

Table 4.2: The pion energy and two-point function normalization, with different momentum directions. Components of p are in unit of $\frac{\pi}{2L}$. Measured on 24 configuration.

Another test of cubic symmetry at pion level is by checking the orthogonality of the following 2 pi-pi states:

$$\pi\pi_{A1} = \frac{1}{2}\{(+++) \oplus (-++) \oplus (+-+) \oplus (++-)\} \tag{4.14}$$

$$\pi\pi_{T2_0} = \frac{1}{\sqrt{12}}\{3(+++) \ominus (-++) \ominus (+-+) \ominus (++-)\}, \tag{4.15}$$

where '+' and '-' in each parenthesis indicates the momentum orientation for one of the two pions, the momentum for the other pion is exactly opposite to the first pion and is not written out in the expression. These 2 states are only orthogonal if cubic symmetry is preserved, because they belong to different representations of the cubic group. The observed orthogonality is at sub-percent level as in Figure 4.3.

4.1.3 Special treatment to Kaon

In Chapter 3, we introduced the G-parity counterpart of strange quark s', and the zero-momentum kaon state under G-parity boundary condition, in Equation 3.27. However, for the weak Hamiltonian H_W, we used the traditional definition without introducing the fictional s' quark, which results in an extra factor of $\sqrt{2}$ in the normalization factor of weak

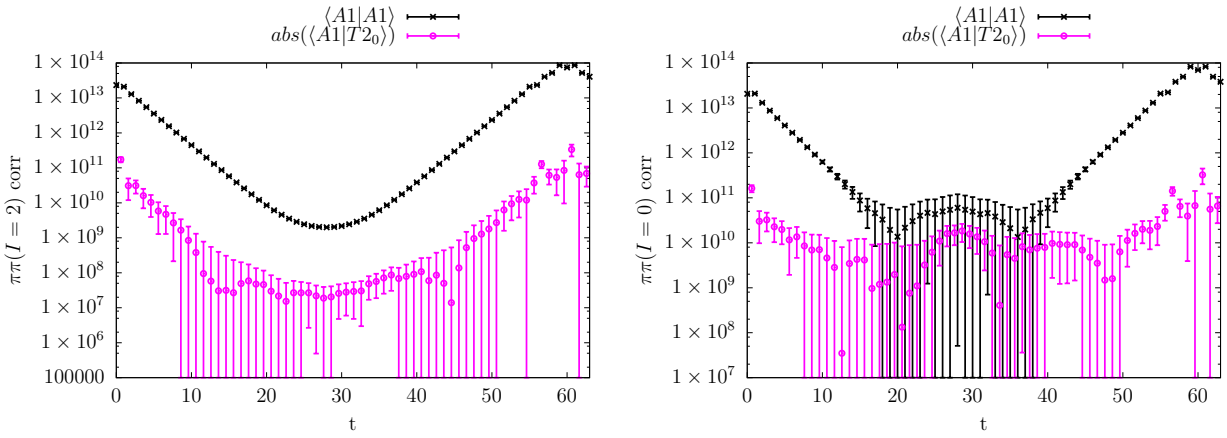

Figure 4.3: Orthogonality of $\pi\pi_{A1}$ state and $\pi\pi_{T2_0}$ state. Left: I=2 channel. Right: I=0 channel.

matrix elements:

$$\langle \pi\pi | H_w | K \rangle_{G-parity} = \frac{1}{\sqrt{2}} \langle \pi\pi | H_w | K \rangle \tag{4.16}$$

This is because only half of the kaon source couples to the weak Hamiltonian. Only $\frac{i}{\sqrt{2}}\bar{d}\gamma_5 s$ part of kaon source can be absorbed by H_w.

4.2 All-to-all propagators

A major difficulties in $K \to \pi\pi(I = 0)$ calculation is the bad signal-to-noise ratio, due to the disconnected graphs (e.g. the Vacuum graph in Table 3.1 and Type 4 graphs in Appendix B). Because there are no quark lines joining the initial and final two parts, the noise from these graphs doesn't fall exponentially as the time extent grows, but the signal does. One way to reduce the fluctuation in these graphs is to use better meson interpolating operators that have a better overlap with $\pi\pi$ ground state, reducing the fluctuation due to unphysical coupling with vacuum. In our previous threshold $K \to \pi\pi(I = 0)$ calculation [28], the pion interpolating operator is wall-like, where the two quarks in each pion are both distributed over the whole spatial extend and are linked by gauge links to make a gauge

invariant operator. Since the actual size of a pion is less than the lattice size (for example, on the 32nt64 ensemble, $m_\pi L \approx 3$), the wall-like $\pi\pi$ operator introduces unphysical coupling with the vacuum.

All-to-all propagators provide a way to reduce this unphysical uncoupling. In Ref [29], we explored this technique on a $16^3 \times 32$ (in later text, it's abbreviated as "16nt32") ensemble without G-parity boundary conditions, and observed a factor of 2 decrease in error bars of $E_{\pi\pi(I=0)}$ and $\mathrm{Im}(A_0)$, compared to the result using wall-like meson operators. Detailed comparison is presented in Appendix D.

4.2.1 General idea

All-to-all propagators provide a way to approximate the quark propagator $G(x,y) \equiv D^{-1}(x;y)$ with any combination of x and y without inverting the Dirac operator for each choice of y. Suppose we have a random vector $\vec{\eta}$ with all its component η_x being mutually independent. By definition the correlation matrix is a unit matrix:

$$\langle \eta_x \eta_y^* \rangle = \delta_{xy} \tag{4.17}$$

Using this relation, the quark propagator $G(x;y)$ with an arbitrary combination of x and y can be approximated as[30, 31]:

$$(D^{-1}\vec{\eta})_x \eta_y^* = D^{-1}(x;x')\eta_{x'}\eta_y^* \approx D^{-1}(x;x')\delta_{x'y} = D^{-1}(x;y) = G(x;y), \tag{4.18}$$

or equivalently,

$$D^{-1} \approx (D^{-1}\vec{\eta}) \otimes \vec{\eta}^\dagger, \tag{4.19}$$

where the approximation becomes exact if we sample an infinite number of independent $\vec{\eta}$ vectors and take the average:

$$D^{-1} = \lim_{N_{hit}\to\infty} \frac{1}{N_{hit}} \sum_{i=1}^{N_{hit}} (D^{-1}\vec{\eta}^{\,i}) \otimes \vec{\eta}^{\,i\dagger}. \tag{4.20}$$

Though they can be used to calculate propagators from all points to all points, all-to-all propagators introduces noise because the use of the random vector $\vec{\eta}$. To reduce the variance, we can use those eigenvectors with small eigenvalues to construct the low energy part of Dirac operator and only use random vectors in the high energy part:

$$D^{-1} \approx \sum_{i=1}^{N_{ev}} \frac{\vec{h}^i \otimes \vec{h}^{i\dagger}}{\lambda^i} + \sum_{j=1}^{N_{hit}} (D^{-1}_{deflate}\vec{\eta}^j) \otimes \vec{\eta}^{j\dagger} \tag{4.21}$$

$$D^{-1}_{deflate} \equiv D^{-1} - \sum_{i=1}^{N_{ev}} \frac{\vec{h}^i \otimes \vec{h}^{i\dagger}}{\lambda^i}, \tag{4.22}$$

where N_{ev} is the number of low eigenvectors of the Dirac operator which are used and λ^i are the corresponding eigenvalues. N_{ev} and N_{hit} can both be adjusted depending on how much precision we want for the low and high energy parts. For simplicity, we will call the fermion vectors in the set $\{\frac{h_i}{\lambda_i}, D^{-1}_{deflate}\vec{\eta}^j\}$ as $\vec{v}$, call those in the set $\{h^{i\dagger}, \eta^{j\dagger}\}$ as $\vec{w}^\dagger$. Both $\vec{v}$ and $\vec{w}$ are fermion vectors with indices identify the correspond mode or hit number.

4.2.2 Definition of $\vec{v}$ and $\vec{w}$ vectors

Until now, we have been describing the general idea of all-to-all propagators. In this work, the $\vec{v}$ and $\vec{w}$ vectors are defined in the context of preconditioned Dirac operator. For example

the even-odd preconditioned Shamir-kernel Dirac operator is:

$$\begin{aligned} D_{DWF} &= \begin{pmatrix} M_{ee} & M_{eo} \\ M_{oe} & M_{oo} \end{pmatrix} \\ &= \begin{pmatrix} 1 & 0 \\ M_{oe}M_{ee}^{-1} & 1 \end{pmatrix} \begin{pmatrix} M_{ee} & 0 \\ 0 & M_{oo} - M_{oe}M_{ee}^{-1}M_{eo} \end{pmatrix} \begin{pmatrix} 1 & M_{ee}^{-1}M_{eo} \\ 0 & 1 \end{pmatrix} \\ &= \begin{pmatrix} 1 & 0 \\ M_{oe}M_{ee}^{-1} & 1 \end{pmatrix} \begin{pmatrix} M_{ee} & 0 \\ 0 & D_{oo} \end{pmatrix} \begin{pmatrix} 1 & M_{ee}^{-1}M_{eo} \\ 0 & 1 \end{pmatrix} \end{aligned}$$

The inverted Dirac operator is then:

$$D_{DWF}^{-1} = \begin{pmatrix} 1 & -M_{ee}^{-1}M_{eo} \\ 0 & 1 \end{pmatrix} \begin{pmatrix} M_{ee}^{-1} & 0 \\ 0 & (D_{oo}^{\dagger}D_{oo})^{-1} \end{pmatrix} \begin{pmatrix} 1 & 0 \\ 0 & D_{oo}^{\dagger} \end{pmatrix} \begin{pmatrix} 1 & 0 \\ -M_{oe}M_{ee}^{-1} & 1 \end{pmatrix}$$

The Lanczos algorithm is then used to calculate the low eigenvectors (low-modes) of the Hermitian operator $(D_{oo}^{\dagger}D_{oo})^{-1}$. By separating out the low-mode contribution of $D_{oo}^{\dagger}D_{oo}$, we can write D_{DWF}^{-1} into two parts:

$$\begin{aligned} D_{DWF}^{-1} &= A + B \\ A &= \begin{pmatrix} 1 & -M_{ee}^{-1}M_{eo} \\ 0 & 1 \end{pmatrix} \begin{pmatrix} 0 & 0 \\ 0 & \sum \frac{1}{\lambda_i} h_i h_i^{\dagger} \end{pmatrix} \begin{pmatrix} 1 & 0 \\ 0 & D_{oo}^{\dagger} \end{pmatrix} \begin{pmatrix} 1 & 0 \\ -M_{oe}M_{ee}^{-1} & 1 \end{pmatrix} \\ B &= \begin{pmatrix} 1 & -M_{ee}^{-1}M_{eo} \\ 0 & 1 \end{pmatrix} \begin{pmatrix} M_{ee}^{-1} & 0 \\ 0 & (D_{oo}^{\dagger}D_{oo})^{-1} - \sum \frac{1}{\lambda_i} h_i h_i^{\dagger} \end{pmatrix} \begin{pmatrix} 1 & 0 \\ 0 & D_{oo}^{\dagger} \end{pmatrix} \begin{pmatrix} 1 & 0 \\ -M_{oe}M_{ee}^{-1} & 1 \end{pmatrix} \end{aligned}$$

Where A is the low mode part, B is the high mode part. Finally the two sets of vectors $\{v_i\}$ and $\{w_i\}$ in all-to-all propagators are defined as:

For $i = 1, 2, \cdots, N_{low}$ (low-mode part):

$$
\begin{aligned}
v_i &= \begin{pmatrix} 1 & -M_{ee}^{-1} M_{eo} \\ 0 & 1 \end{pmatrix} \begin{pmatrix} 0 \\ \frac{1}{\lambda_i} h_i \end{pmatrix} \\
w_i &= \begin{pmatrix} 1 & -M_{ee}^{-1,\dagger} M_{oe}^{\dagger} \\ 0 & 1 \end{pmatrix} \begin{pmatrix} 1 & 0 \\ 0 & D_{oo} \end{pmatrix} \begin{pmatrix} 0 \\ h_i \end{pmatrix}
\end{aligned}
$$

For $i = N_{low} + 1, N_{low} + 2, \cdots, N_{low} + N_{high}$ (high-mode part):

$$
\begin{aligned}
v_i &= \begin{pmatrix} 1 & -M_{ee}^{-1} M_{eo} \\ 0 & 1 \end{pmatrix} \begin{pmatrix} M_{ee}^{-1} & 0 \\ 0 & (D_{oo}^{\dagger} D_{oo})^{-1} - \sum \frac{1}{\lambda_i} h_i h_i^{\dagger} \end{pmatrix} \begin{pmatrix} 1 & 0 \\ 0 & D_{oo}^{\dagger} \end{pmatrix} \begin{pmatrix} 1 & 0 \\ -M_{oe} M_{ee}^{-1} & 1 \end{pmatrix} \eta_i \\
w_i &= \eta_i
\end{aligned}
$$

When using the Möbius Dirac operator instead of Shamir Dirac operator, a similar idea is applied to define $\vec{v}$ and $\vec{w}$ vectors but we must include the additional D_- operator.

$$
D_{MDWF}^{-1} D_- = \begin{pmatrix} 1 & -M_{ee}^{-1} M_{eo} \\ 0 & 1 \end{pmatrix} \begin{pmatrix} M_{ee}^{-1} & 0 \\ 0 & (D_{oo}^{\dagger} D_{oo})^{-1} \end{pmatrix} \begin{pmatrix} 1 & 0 \\ 0 & D_{oo}^{\dagger} \end{pmatrix} \begin{pmatrix} 1 & 0 \\ -M_{oe} M_{ee}^{-1} & 1 \end{pmatrix} D_-
$$

$$
\begin{aligned}
&D_{MDWF}^{-1} D_- = A + B \\
&A = \begin{pmatrix} 1 & -M_{ee}^{-1} M_{eo} \\ 0 & 1 \end{pmatrix} \begin{pmatrix} 0 & 0 \\ 0 & \sum \frac{1}{\lambda_i} h_i h_i^{\dagger} \end{pmatrix} \begin{pmatrix} 1 & 0 \\ 0 & D_{oo}^{\dagger} \end{pmatrix} \begin{pmatrix} 1 & 0 \\ -M_{oe} M_{ee}^{-1} & 1 \end{pmatrix} D_- \\
&B = \begin{pmatrix} 1 & -M_{ee}^{-1} M_{eo} \\ 0 & 1 \end{pmatrix} \begin{pmatrix} M_{ee}^{-1} & 0 \\ 0 & (D_{oo}^{\dagger} D_{oo})^{-1} - \sum \frac{1}{\lambda_i} h_i h_i^{\dagger} \end{pmatrix} \begin{pmatrix} 1 & 0 \\ 0 & D_{oo}^{\dagger} \end{pmatrix} \begin{pmatrix} 1 & 0 \\ -M_{oe} M_{ee}^{-1} & 1 \end{pmatrix} D_-
\end{aligned}
$$

For $i = 1, 2, \cdots, N_{low}$ (low-mode part):

$$
\begin{aligned}
v_i &= \begin{pmatrix} 1 & -M_{ee}^{-1} M_{eo} \\ 0 & 1 \end{pmatrix} \begin{pmatrix} 0 \\ \frac{1}{\lambda_i} h_i \end{pmatrix} \\
w_i &= D_-^\dagger \begin{pmatrix} 1 & -M_{ee}^{-1,\dagger} M_{oe}^\dagger \\ 0 & 1 \end{pmatrix} \begin{pmatrix} 1 & 0 \\ 0 & D_{oo} \end{pmatrix} \begin{pmatrix} 0 \\ h_i \end{pmatrix}
\end{aligned}
$$

For $i = N_{low} + 1, N_{low} + 2, \cdots, N_{low} + N_{high}$ (high-mode part):

$$
\begin{aligned}
v_i &= \begin{pmatrix} 1 & -M_{ee}^{-1} M_{eo} \\ 0 & 1 \end{pmatrix} \begin{pmatrix} M_{ee}^{-1} & 0 \\ 0 & (D_{oo}^\dagger D_{oo})^{-1} - \sum \frac{1}{\lambda_i} h_i h_i^\dagger \end{pmatrix} \begin{pmatrix} 1 & 0 \\ 0 & D_{oo}^\dagger \end{pmatrix} \begin{pmatrix} 1 & 0 \\ -M_{oe} M_{ee}^{-1} & 1 \end{pmatrix} D_- \eta_i \\
w_i &= \eta_i
\end{aligned}
$$

Note that the eigenvectors of $(D_{oo}^\dagger D_{oo})^{-1}$ with small eigenvalues are not only necessary to compute the low-mode $\vec{v}$ and $\vec{w}$ vectors, but they also project out the low mode part of $(D_{oo}^\dagger D_{oo})^{-1}$ (so called "deflation" technique), causing the condition number of $(D_{oo}^\dagger D_{oo})^{-1} - \sum \frac{1}{\lambda_i} h_i h_i^\dagger$ being smaller than $(D_{oo}^\dagger D_{oo})^{-1}$. This will reduce the CG iteration number when solving for the high mode $\vec{v}$ vectors. The speed-up due to projecting out low-mode in $(D_{oo}^\dagger D_{oo})$ can be seen from Figure 6.1 for the 32nt64 ensemble, and Figure 5.1 for the 16nt32 ensemble.

4.2.3 Lanczos Algorithm

The Lanczos algorithm is used to find the low modes of the preconditioned operator $D_{oo}^\dagger D_{oo}$, which are then used to construct the all-to-all propagators as described in above. When finding eigenvectors of a Hermitian matrix A, the Lanczos algorithm makes a guess for

a set of vectors $\{\vec{h}_i | i = 1, 2, \cdots, M\}$, and iteratively improves them (also known as implicit restart) until they are close enough to the true eigenvectors in the Krylov space $\{\vec{v}_0, A\vec{v}_0, A^2\vec{v}_0, \cdots, A^{N-1}\vec{v}_N\}$, where v_0 is a random vector and $M < N$. Lanczos algorithm is most efficient when the eigenvalues are large and well separated. There are three important parameters we can tune to speed up the Lanczos algorithm: α, β, and the order of Chebyshev filter n. They are used to construct a new matrix $T_n(q(A))$, which is a polynomial of the original matrix A, such that the eigenvalues of A within the range (β, α) correspond to very small ($\ll 1$) eigenvalues of $T_n(q(A))$, while the other eigenvalues correspond to large and well separated eigenvalues ($\gg 1$) of $T_n(q(A))$. The Chebyshev filter makes it easier to find the eigenvectors of A, which have eigenvalues in the range of $(0, \beta)$ and (α, ∞).

$$q(A; \alpha, \beta) = \frac{(A^2 - \beta^2) + (A^2 - \alpha^2)}{(\beta^2 - \alpha^2)} \tag{4.23}$$

$$T_n(q(A)) = 2q(A)T_{n-1}(q(A)) - T_{n-2}(q(A)) \tag{4.24}$$

$$T_1(q(A)) = q(A) \tag{4.25}$$

The larger n is, the fewer iteration of implicit restart. But the time in each implicit restart increases because the time complexity of multiplying a vector by $T_n(q(A))$ is $O(n)$. α and β values are usually chosen so that α exceeds the largest eigenvalue of A by $\approx 10\%$, and β exceeds the largest desired eigenvalue by $\approx 10\%$. If β or α is chosen too large, the degeneracy of eigenvectors is not broken down enough at small eigenvalues (Figure 4.4 and 4.5), which slows the Lanczos method since it takes more iterations to distinguish the near-degenerate eigenvectors.

Since the range of eigen values of $(D_{oo}^{\dagger} D_{oo})$ is not known prior to running Lanczos, it usually needs several trial-and-error tests before the optimum parameters α, β are found.

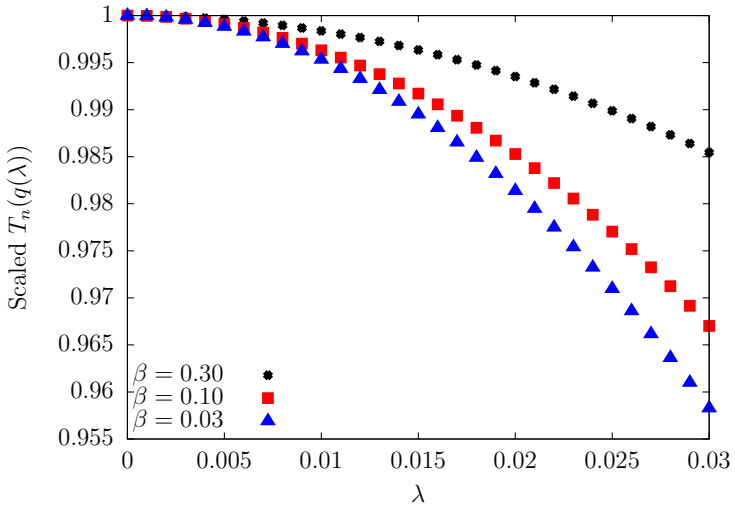

Figure 4.4: The eigen value and its mapped value. Mapped eigen-values in each curve are scaled (multiply by a factor) such that the largest value is 1. Chebyshev-Polynomial order $n = 50$, $\alpha = 10$

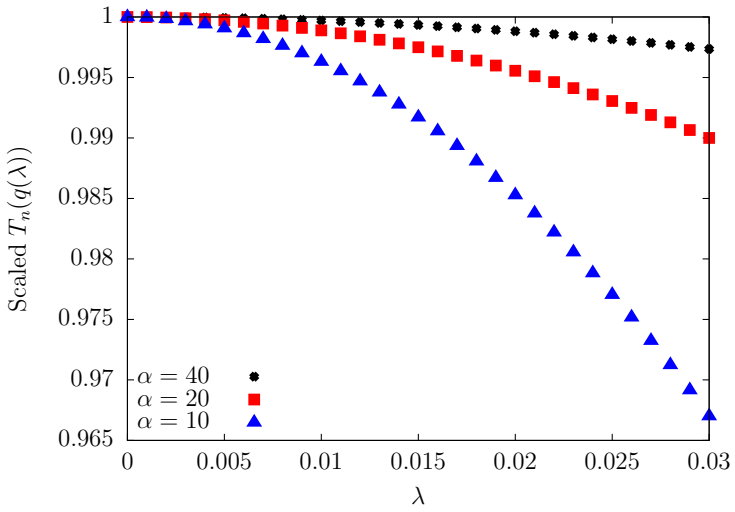

Figure 4.5: The eigen value and its mapped value. Mapped eigen-values in each curve are scaled (multiply by a factor) such that the largest value is 1. Chebyshev-Polynomial order $n = 50$, $\beta = 0.1$

4.2.4 Construction of meson field

Now the propagator between two arbitrary points can be written as:

$$D^{-1}(x;y) \approx \sum_{i=1}^{N_{ev}+N_{hit}} v^i(x) w^{i*}(y), \tag{4.26}$$

where x and y are indices representing space, time, spin, and color. (Note that in the presence of G-parity boundary conditions, x and y will also contain flavor indices.) The approximation sign is from the use of random vectors in the high energy part.

One obvious advantage of all-to-all propagators is that it saves the CG time. When using the traditional method to calculate a momentum wall source quark propagator, we need one solve for each quark momentum:

$$\tilde{G}(x', t_2; p, t_1) = \sum_x D^{-1}(x', t_2; x, t_1) e^{-ipx}, \tag{4.27}$$

where p is the quark momentum. In contrast, an all-to-all propagator does not need any extra solves for multiple quark momenta, because it already contains the propagation information from an arbitrary source point to an arbitrary sink point, up to random noise[29]:

$$G(x', t_2; x, t_1) \approx \sum_i v^i(x', t_2) w^{i\dagger}(x, t_1), \tag{4.28}$$

and the quark momentum are included by doing a Fourier transform:

$$\tilde{G}(x', t_2; p, t_1) \approx \sum_x \sum_i v^i(x', t_2) w^{i\dagger}(x, t_1) e^{-ipx} \ . \tag{4.29}$$

The above equation is for a momentum-source-point-sink propagator, while the momentum-source-momentum-sink propagator requires a Fourier transform on x' also. As can be seen from this equation, different quark momenta amount to different Fourier transforms, and no

extra inversion of the Dirac operator is needed, only the sum over modes must be performed for each choice of p. In the presence of G-parity boundary in 3 spatial directions, the allowed quark momenta are $p = (n_1, n_2, n_3)\frac{2\pi}{L} \pm (1,1,1)\frac{\pi}{2L}$ with n_i being integers, and it turns out that we need to use at least 4 of them to construct a two-pion operator which has the greatest degree of cubic symmetry. In our current $K \to \pi\pi(I=0)$ measurement job, with the use of all-to-all propagators, it takes 30% of the total time to compute the light quark propagator with only one momentum (on all 64 time slices). It's obvious that using all-to-all propagators saves a significant amount of computational time.

Once we have calculated the $\vec{v}$ vectors and $\vec{w}$ vectors, we can build the meson fields. As an example, the pseudo-scaler correlation function between two time slices is:

$$\begin{aligned}\sum_{x,y} G(x,t_x;y,t_y)\gamma_5 G(y,t_y;x,t_x)\gamma_5 &= \sum_{x,y,i,j} v^i(x,t_x) w^{i\dagger}(y,t_y)\gamma_5 v^j(y,t_y) w^{j\dagger}(x,t_x)\gamma_5 \\ &= \sum_{i,j}\sum_{x}\{w^j(x,t_x)^\dagger \gamma_5 v^i(x,t_x)\}\sum_{y}\{w^{i\dagger}(y,t_y)\gamma_5 v^j(y,t_y)\} \\ &= \sum_{i,j}\Pi^{ji}_{t_x}\Pi^{ij}_{t_y} \qquad (4.30)\end{aligned}$$

Here repeated indices are summed, and the summation on x and y is over their spacial indices, leaving the correlator as a function of time. The meson field Π in (4.30) is actually a point-like meson, in which the two quarks are right on top of each other. In order to make a better overlap with the meson ground state, we can allow some displacement between the two quarks, link them by Coulomb fixed color matrix $S(x)$, and weight the operator by a meson field wave function $\phi(r)$, so that:

$$\Pi^{ij}_{t_x} = \sum_{x,x'} w^{i\dagger}(x) S^\dagger(x)\gamma_5 S(x') v^j(x')\phi(|x-x'|) \qquad (4.31)$$

Here the γ_5 spin matrix comes from that in the pion interpolating operator.

Because the ϕ function depends only on the distance between x and x', we can use a fast

Fourier transform to efficiently evaluate the convolution in Π:

$$\Pi^{ij}_{t_x} = \frac{1}{V}\sum_{\vec{p}} \tilde{w}^{i\dagger}(\vec{p})\gamma_5\tilde{v}^{j}(\vec{p})\tilde{\phi}(\vec{p}), \tag{4.32}$$

where V is the spatial volume, the $\tilde{w}$ and $\tilde{v}$ are the gauge-fixed and Fourier transformed vectors of w and v:

$$\tilde{w}^{k}_{\vec{p},a,\alpha} = \sum_{x,b} S(x)_{ab} w^{k}_{x,b,\alpha} e^{-i\vec{p}x} \tag{4.33}$$

$$\tilde{v}^{k}_{\vec{p},c,\beta} = \sum_{x,b} S(x)_{cb} v^{k}_{x,b,\beta} e^{-i\vec{p}x} \tag{4.34}$$

$$\tilde{\phi}(\vec{p}) = \sum_{x} \phi(x) e^{-i\vec{p}x}, \tag{4.35}$$

where the color indices a, b, c are written out explicitly.

With G-parity boundary conditions, the w vector and v vector contain the two flavor components and the quark momentum phase factor, and the γ_5 spin structure in the meson field of the π^0 pion will be replaced by $\sigma_3\gamma_5$. As a result the meson field with G-parity boundary conditions becomes:

$$\Pi^{ij}_{t_x,\vec{k}_1+\vec{k}_2} = \sum_{x,x'} e^{-i\vec{k}_1 x} w^{i\dagger}(x) S^{\dagger}(x)\sigma_3\gamma_5 S(x') e^{-i\vec{k}_2 x'} v^{j}(x')\phi(|x-x'|) \tag{4.36}$$

$$= \frac{1}{V}\sum_{\vec{p}} \tilde{w}^{i\dagger}(\vec{p}-\vec{k}_1)\sigma_3\gamma_5\tilde{v}^{j}(\vec{p}+\vec{k}_2)\tilde{\phi}(\vec{p}), \tag{4.37}$$

The trivial meson field wave function $\phi(r) = 1$ corresponds to the wall-source-wall-sink quark propagator. A better choice is a localized wave function, for example a hydrogen wave function like:

$$\phi(|x-x'|) = e^{-|x-x'|/r} \tag{4.38}$$

The parameter r controls the size of the meson and needs some tuning. As can be seen from Figure (4.6): when choosing a too small meson size r, the excited states contamination becomes worse (left figure); when choosing a too large meson size, the signal becomes worse because the $\pi\pi(I = 0)$ state now has a large overlap with vacuum and the disconnected diagrams fluctuate hugely (right figure).

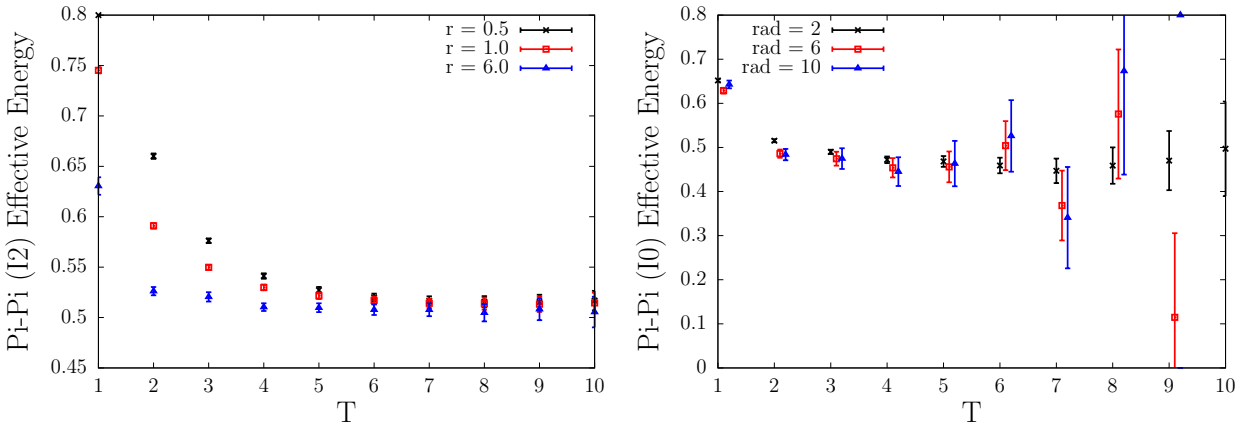

Figure 4.6: $E_{\pi\pi}$ measured on 16nt32 Iwasaki+DWF ensemble with periodic boundary condition. Left: $\pi\pi(I = 2)$ effective mass plot. Right: $\pi\pi(I = 0)$ effective mass plot.

Though it brings advantages, this use of all-to-all propagators could easily introduce systematic error due to unexpected correlation between random numbers. For example, without using low eigenvectors, the single pion correlation function with point-like pion interpolating operator is:

$$\begin{aligned} \langle\hat{\pi}(x')\hat{\pi}(x)\rangle &= Tr\{D^{-1}(x';x)\gamma_5 D^{-1}(x;x')\gamma_5\} \\ &\approx \sum_{i,j} Tr\{D^{-1}(x';x'')w^i(x'')w^{i\dagger}(x)\gamma_5 D^{-1}(x;x''')w^j(x''')w^{j\dagger}(x')\gamma_5\}, \end{aligned} \tag{4.39}$$

where for simplicity the spin-color indices are hidden. The summation over mode indices i and j are supposed to produce the delta function:

$$\sum_{i,j} w^i(x'')w^{i\dagger}(x)w^j(x''')w^{j\dagger}(x') \approx \delta(x'' - x)\delta(x''' - x'), \tag{4.40}$$

so that the approximation holds on the second line of equation (4.39). But equation (4.40) is not totally true, in fact:

$$\begin{aligned}\sum_{i,j} w^i(x'')w^{i\dagger}(x)w^j(x''')w^{j\dagger}(x') &\approx \delta(x''-x)\delta(x'''-x') + \sum_{i,j}\delta_{ij}(w^i(x'')w^{j\dagger}(x'))(w^{i\dagger}(x)w^j(x''')) \\ &\approx \delta(x''-x')\delta(x'''-x) + \frac{1}{N}\delta(x''-x')\delta(x-x'''), \qquad (4.41)\end{aligned}$$

where N is the number of random hits. The second term in equation (4.41) is not expected and will cause systematic error. One way to avoid it is to dilute the random vectors w in the time index:

$$w(x) = \sum_{i=1}^{T} w^j(x) \qquad (4.42)$$

$$w^j(x) = \delta_{jt_x} w(x) \qquad (4.43)$$

Each of the diluted random vector $\{w^1, w^2, \cdots, w^T\}$ is inverted, generating T pairs of $\{w^j, v^j\}$ and a better approximation for D^{-1} from a single noise source:

$$D^{-1} \approx \sum_{i=1}^{T} \vec{v}^i \otimes \vec{w}^{i\dagger} \qquad (4.44)$$

After dilution, the product of w^i_{x1} and $w^{i\dagger}_{x2}$ will be exactly zero (not by statistic), as long as $x1$ and $x2$ are not on the same time slice. The systematic error in equation (4.39) will be eliminated for those x and x' on different time slices.

4.2.5 $K \to \pi\pi$ correlation functions using all-to-all propagators

When using all-to-all propagators to calculate the $K \to \pi\pi$ decay amplitude, because of γ_5-Hermiticity (see Equation 3.76) in our lattice propagators, we can choose which end is the source (w vectors) and which end is the sink (v vectors) for each quark propagator, Figure

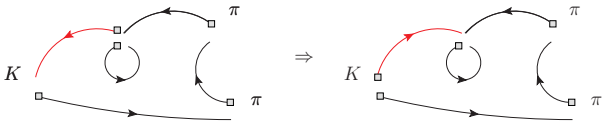

Figure 4.7: Left: original contraction. Right: a better way to do contraction.

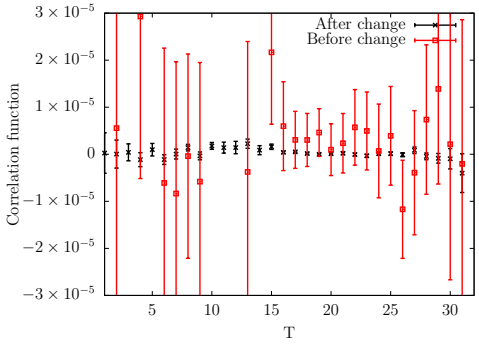

Figure 4.8: Measured correlation function corresponds to Figure 4.7

4.7 shows two ways of doing the contraction, shaded boxes are where we have used random numbers. Note that in order to avoid the systematic error as in (4.41), the shaded boxes are put on different time slices except for the one on the only strange quark propagator (in red). This doesn't introduce systematic error because the w random vectors for the strange quark are independent of those for the light quark. The left panel and right panels in Figure 4.7 show two ways to calculate the $K \to \pi\pi$ correlation functions. The right panel turns out to be a much better way. The lesson is that when using all-to-all propagators it is best to locate as few random sources as possible at the four-quark operator. Figure 4.8 shows how large the improvement is.

Another unexpected difficulty is the large computational cost of evaluating the $K \to \pi\pi$ contraction, which arises from the large number of modes in the all-to-all propagators. Take

the contraction C13 (see Appendix B) as an example:

$$\begin{aligned} C13(\Gamma_1,\Gamma_2) &= Tr\{\Gamma_1 \mathcal{G}^{(L)}_{x_{op},x_{\pi_1}} S_2 \mathcal{G}^{(L)}_{x_{\pi_1},x_{\pi_2}} S_2 \mathcal{G}^{(L)}_{x_{\pi_2},x_K} \gamma_5 \mathcal{G}^{(H)}_{x_K,x_{op}}\} \cdot Tr\{\Gamma_2 \mathcal{G}^{(L)}_{x_{op},x_{op}}\} \\ &= \sum_{\vec{x}_{op}} \{{w'}^{m}_{x_{op}}{}^{\dagger} \Gamma_1 v^i_{x_{op}}\} \cdot \{w^j_{x_{op}}{}^{\dagger} \Gamma_2 v^j_{x_{op}}\} \cdot \Pi^{ik}_{t_{\pi_1}} \Pi^{kl}_{t_{\pi_2}} K^{lm}_{t_K}, \end{aligned} \tag{4.45}$$

where the Π and K on the second line are the meson fields for pion and kaon respectively. Taking into account the summation over x_{op} and the time translations of kaon and pipi fields, the computational time is proportional to (Number of Modes)^2 $\times$ (Volume) $\times$ (T size) $\times 24^2$. The trailing 24^2 is the size of the spin-color-flavor matrix in each of the traces $Tr\{\cdots\}$. In the production run on our 32nt64 ensemble (see Chapter 6), the total number of modes for light quark is 2436, volume is $32^3 \times 64$, T is 64. The total computational cost of evaluating this contraction is large and several optimizations are used, which are explained in Chapter 6.

4.3 Data Analysis

4.3.1 Regression

Once we have the lattice correlation functions, we can extract out physical parameters using regression analysis. For example, we have the measured pion correlation function $C(t)$ and another analytic function $f(t,\theta)$ expected to describe $C(t)$. We use the quantity χ^2 as a measure of goodness of fit:

$$\chi^2 = \sum_{t_1,t_2} [f(t_1,\theta) - C(t_1)] V^{-1}(t_1,t_2) [f(t_2,\theta) - C(t_2)], \tag{4.46}$$

where

$$V(t_1,t_2)=\frac{1}{N(N-1)}\sum_{i=1}^{N}(C^i_{t_1}-\overline{C(t_1)})(C^i_{t_2}-\overline{C(t_2)}), \tag{4.47}$$

t_1,t_2 are two numbers within the fitting range, i is the index of measured configuration. The parameter(s) θ in $f(t,\theta)$ that gives the minimum χ^2 is the result of regression. In the case of pion correlation function, $f(t,\theta)=Z_\pi(e^{-t\cdot m_\pi}+e^{-(T-t)\cdot m_\pi})$ and θ contains the pion mass and norm of the pion state.

4.3.2 Jackknife resampling

Regression analysis gives the expected values of parameters, but not the distribution. The jackknife procedure is a way to estimate the standard deviation of parameters. If the sample S has a size of N, jackknife resampling first generates N sub-samples $S_i, i\in 1,2,\cdots,N$, where each S_i are drawn from the original sample S but with the ith element left out. For each S_i, we can then do the usual regression analysis and get the result θ_i. Finally the mean and standard deviation of the parameter θ are:

$$\bar{\theta} = \frac{1}{N}\sum_{i=1}^{N}\theta_i \tag{4.48}$$

$$\sigma^2_\theta = \frac{N-1}{N}\sum_{i=1}^{N}(\theta_i-\bar{\theta})^2 \tag{4.49}$$

Chapter 5

Results from $16^3 \times 32 \times 16$ Lattice

Because of the complexity of the $K \to \pi\pi$ project, we did a first trial calculation on a small $16^3 \times 32 \times 16$ lattice. The pions and kaons are both unphysical but the calculation is relatively cheap and it serves as a playground to test the all-to-all propagators and G-parity boundary conditions.

5.1 Gauge Ensembles

The ensembles were generated using the Iwasaki gauge action with $\beta = 2.13$ (corresponding to the inverse lattice spacing $a^{-1} = 1.73(3)$GeV [2]), and 2+1 dynamical flavors of Domain Wall Fermions (DWF). The lattice size is $16^3 \times 32$ with the fifth dimension of size $L_s = 16$. The sea quark masses are $m_{u/d} = 0.01$ and $m_s = 0.032$. These parameters are chosen to match a previously generated ensemble described in Ref. [2]. Although in Ref. [2] a heavier strange quark mass 0.04 is used, that ensemble was later extended using a lighter strange quark mass 0.032, to make the kaon more physical.

With this setup, we generated three ensembles with G-parity boundary conditions in 1, 2, and 3 spatial directions.

5.2 Computational Details

In all 3 ensembles, Shamir kernel with $L_s = 16$ is used for the 5D Dirac operator. The temporal boundary conditions are all anti-periodic. The light quark all-to-all propagators contain 100 low modes, for high mode part we use 1 random hit on each lattice site with time-spin-color-flavor dilution. So the total number of $\vec{v}$ vectors (as so is $\vec{w}$ vectors) in light quark all-to-all propagators is $100 + 32 * 12 * 2 = 868$. For the strange quark, we use the same setup for high mode part as is used in the light quark all-to-all propagators, but no low modes are used. Coulomb gauge fixing on each time slice is used to construct gauge invariant pion interpolating operators. The Lanczos algorithm uses the parameters $\alpha = 5.5, \beta = 0.5$ and Chebyshev order $n = 100$.

The number of low modes is chosen such that the low mode deflation no longer reduces the CG iteration number significantly as in Figure 5.1. Since CG iteration number depends on the condition number (ratio of the largest eigenvalue to the smallest eigenvalue) of the matrix to be inverted, Figure 5.1 also indicates that further increasing the number of low modes will only slowly increase the corresponding eigenvalues.

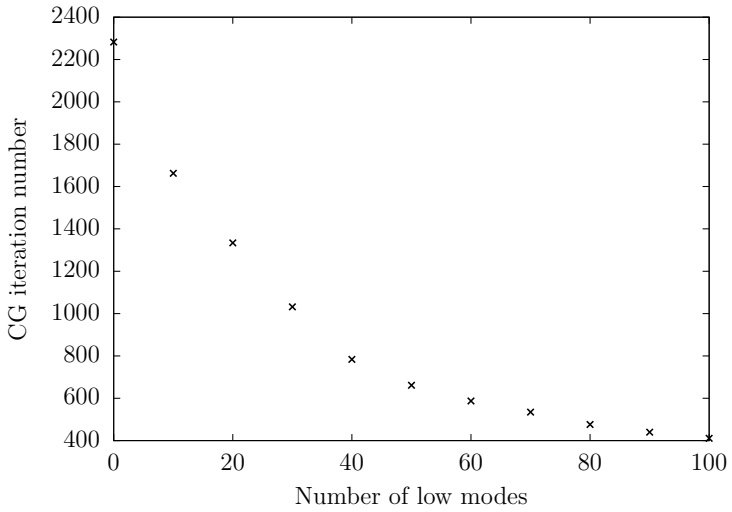

Figure 5.1: CG iteration number depending on number of low modes used for deflation.

The number of random number hits is always chosen as 1 throughout this work, this is suggested by experimenting with various number of random hits. We have used 1 to 4 random hits on the most noisy vacuum graphs in $\pi\pi(I = 0)$ scattering and compare the error bar in the resulting $\pi\pi(I = 0)$ energy. The experiment is done on the G-parity 1-twist ensemble, the two points in the $\pi\pi$ source are separated by 4 time slices (as are those in the sink $\pi\pi$), and the $\pi\pi$ correlator are measured on 560 configurations. The result is in Table 5.1.

Number of random hits	$E_{\pi\pi,I0}$
1	0.5478(412)
2	0.5469(396)
3	0.5461(400)
4	0.5537(402)

Table 5.1: $E_{\pi\pi}$ dependence on hit number.

The meson field wave functions used for both the kaon and pion are a hydrogen wave function as in Equation 4.38, with radius 2. More about meson source in all-to-all propagators is provided in Chapter 4. The quarks' momenta used in pion are in Table 4.1, and Table 5.2 for kaon.

Kaon momentum	quark momenta
(0, 0, 0)	(1, 0, 0) + (-1, 0, 0)
(0, 0, 0)	(1, 1, 0) + (-1,-1, 0)
(0, 0, 0)	(1, 1, 1) + (-1,-1,-1)

Table 5.2: quark momenta used to construct kaon momentum eigenstate. Upper part: 1 spatial G-parity boundary; Middle part: 2 spatial G-parity boundaries; Lower part: 3 spatial G-parity boundaries. All numbers are in units of $\frac{\pi}{2L}$.

The gauge configurations are evolved in a Hybrid Monte Carlo simulation. The neighbouring configurations are likely correlated which reduces the number of independent samples and may cause the error to be underestimated. In order to avoid any autocorrelation in the measured data, we group the data into blocks (also known as binning) and see how the errors

of the fitted result change as the block size changes. If the error doesn't constantly go up as block sizes increases, autocorrelation is not a problem. Table 5.3 shows that as the bin size increases, the errors go up and then stabilize, showing an autocorrelation length of less than 10 (E_π has an autocorrelation length of about 8, $E_{\pi\pi(I=0}$ has an autocorrelation length of about 6, $E_{\pi\pi(I=2}$ has an autocorrelation length of about 8.)

bin size	E_π	$E_{\pi\pi,I2}$	$E_{\pi\pi,I0V}$	$E_{\pi\pi,I0}$
1	0.3067(8)	0.6503(16)	0.5234(48)	0.3648(293)
2	0.3067(11)	0.6503(22)	0.5233(64)	0.3707(355)
3	0.3067(13)	0.6504(26)	0.5233(76)	0.3681(416)
4	0.3067(15)	0.6503(30)	0.5233(84)	0.3731(413)
5	0.3067(16)	0.6503(32)	0.5233(90)	0.3711(451)
6	0.3066(17)	0.6502(35)	0.5233(97)	0.3708(520)
7	0.3067(18)	0.6504(37)	0.5232(101)	0.3811(525)
8	0.3067(19)	0.6503(39)	0.5233(105)	0.3791(498)
9	0.3065(20)	0.6501(40)	0.5233(114)	0.3638(555)
10	0.3066(19)	0.6503(40)	0.5233(115)	0.3809(632)

Table 5.3: The dependence on bin size. $E_{\pi\pi,I0V}$ is the $\pi\pi(I=0)$ energy without disconnected graphs. Measured check point 1000,1001,...1400. pion radius = 2, and split pion operator with time separation of 4. Un-correlated fitting with a diagonal covariance matrix which does not vary with jackknife block.

The two-point correlation function behaves as:

$$C(t) \equiv \langle 0|J_X^\dagger(t)J_X(0)|0\rangle = Z_X^2(e^{-E_X t} + e^{-E_X(T-t)}) + \cdots \tag{5.1}$$

At small time separation t, the two-point correlation function $C(t)$ will contain a non-negligible contribution from excited states (the dots in above equation). In order to perform a valid single state fit, we have to make sure the excited states are negligible within the fitting range. This is conveniently done by calculating the effective energy $E_{eff}(t)$, which is defined by:

$$\frac{C(t+1)}{C(t)} = \frac{\cosh(E_{eff}(t) * (T/2 - t - 1))}{\cosh(E_{eff}(t) * (T/2 - t))} \tag{5.2}$$

The effective energy plots for the 16nt32 ensemble are in Figure E.1. Excited states contamination will typically make the effective energy higher, so the appropriate fitting range is basically where a flat plateau is seen.

5.3 Dispersion Relation

The reason we are using G-parity boundary conditions is that it brings the right kinematics to the pion and kaon ground state, and it's crucial to check this. We measured the pion and kaon energy on the ensembles with 1, 2, and 3 G-parity twists. The result with 0 G-parity twists is taken from the Ref. [18].

Ensemble	0 G-parity	1 G-parity	2 G-parity	3 G-parity
E_π	0.24373(47)	0.31029(71)	0.3665(14)	0.4136(21)
E_K	0.50729(44)	0.5043(12)	0.50591(70)	0.50445(80)

Table 5.4: Pion and kaon energies measured on ensembles with different number of G-parity twists. Valence quark mass are $m_l = 0.01$ and $m_s = 0.099$. Number of configurations used are respectively 800, 551, 289, 165 for E_π, and 800, 99, 289, 165 for E_K for 0, 1, 2, and 3 twists respectively.

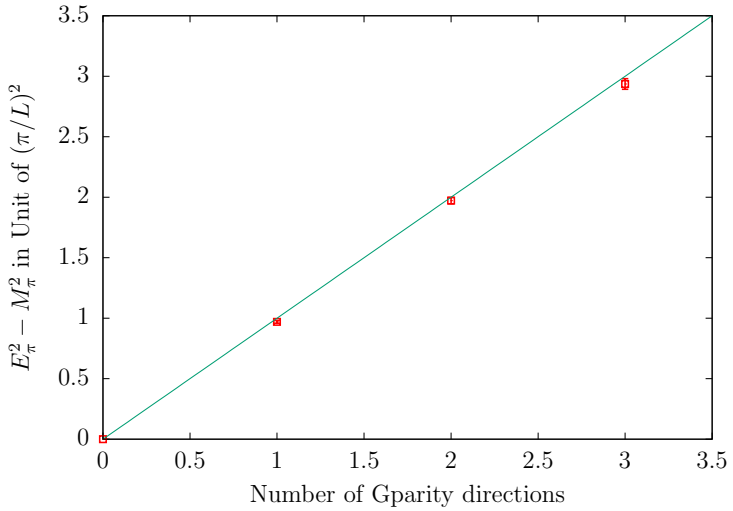

Figure 5.2: pion dispersion relation

From Table 5.4, the kaon mass is statistically the same for different numbers of G-parity twists. Figure 5.2 shows the expected dispersion relation if the pion indeed satisfies G-parity, or anti-periodic, boundary condition: $E_\pi = \sqrt{M_\pi^2 + N_{tw}(\pi/L)^2}$, where M_π is from the Ref. [18].

5.4 $E_{\pi\pi}$ and $\pi\pi$ Scattering Phase Shift

The energy of two-pion state is obtained by fitting the pipi correlator $C_{\pi\pi}(t)$ to the function $Z_{\pi\pi} \times (e^{-m_{\pi\pi}t} + e^{-m_{\pi\pi}(T-t)}) + const$, where the pipi state norm $Z_{\pi\pi}$, mass $m_{\pi\pi}$, and the constant term "const" are the three parameters of the fitting. The constant term is due to the around-the-world effect: the pion emitted from one source propagates forward in time to contract with one sink pion while the other source pion propagate backward in time to contract with the other sink pion. The fitted pipi energies are given in Table 5.5.

Ensemble	1 G-parity	2 G-parity	3 G-parity
$E_{\pi\pi(I=2)}$	0.6590(13)	0.7950(28)	0.9258(74)
$p_{I=2}$	0.22551(56)	0.3174(13)	0.3988(42)
$\delta_2(p_{I=2})$	-0.3622(68)	-0.515(18)	-0.555(40)
$E_{\pi\pi(I=0)}$	0.531(22)	0.46(14)	1.4(14)
$p_{I=0}$	0.113(26)	0.00(31)	0.64(76)
$\delta_0(p_{I=0})$	1.11(38)	-0.0(34)	0.2(74)

Table 5.5: $E_{\pi\pi}$ and phase shifts. Measured 551, 289, and 165 configurations respectively. $E_{\pi\pi(I=2,0)}$ and $p_{I=2,0}$ are in lattice unit a^{-1}; $\delta_{I=2,0}$ is in unit of radian. $p_{I=2,0}$ are calculated from $p_I = \sqrt{E_{\pi\pi(I)}^2/4 - M_\pi^2}$, and $M_\pi = \sqrt{E_\pi^2 - N_{tw}(\frac{\pi}{L})^2}$. N_{tw} is number of G-parity twists.

The pion-pion scattering phase shift is calculated using the 2-particle energy[21]. According to Lüscher's work, there is a relationship between the energy of two-particle state in a finite box and $\pi\pi$ scattering phase shift. This is called Lüscher's quantization condition. In the case of negligible phase shift in angular momentum quantum number number $L > 1$

channel, the $L = 0$ phase shift $\delta(p)$ is determined by:

$$\delta(p) + \phi(q) = n\pi, \tag{5.3}$$

where

$$\begin{aligned} p &= \sqrt{E_{\pi\pi}^2/4 - m_\pi^2} && (5.4)\\ q &= \frac{pL}{2\pi} && (5.5)\\ \tan\,\phi(q) &= -\frac{\pi^{3/2} q}{\mathcal{Z}_{00}(1;q^2)} && (5.6)\\ \mathcal{Z}_{00}(1;q^2) &= \frac{1}{\sqrt{4\pi}} \sum_{n\in S} \frac{1}{n^2 - q^2} && (5.7) \end{aligned}$$

In the last equation S is the set of three component vectors, each component is an integer in directions with periodic boundary conditions and half integer in directions with anti-periodic boundary conditions, from which we can see this condition on the scattering phase shift depends on boundary conditions. Lüscher's original paper only discussed the case where all boundaries are periodic, while in [32] the formula is generalized to any combination of periodic and anti-periodic boundaries. To numerically evaluate the function $\mathcal{Z}_0(1;q^2)$, we used the formula in Appendix A of [33].

Lüscher's quantization condition is quite powerful since it doesn't require knowing the nature of the interaction beforehand. The only assumption is that lattice size is large compared to the scale of interaction, namely $L > 2R$ where R is the scale of interaction. On the 16nt32 lattice, $m_\pi L \approx 4$ which justifies the use of Lüshcer's quantization condition.

In the I=2 channel pion-pion scattering, the energy $E_{\pi\pi}$ is higher than twice E_π and the phase shift is negative, because of the repulsion between the two pions. While in I=0 channel pion-pion scattering, because of the attraction between the two pions, the energy is lower than twice E_π and phase shift is positive (observed from the better resolved 1 G-parity case).

Also note that the G-parity boundary condition is crucial in calculating the phase shift δ_0, without it the two pions are both at rest and p becomes an imaginary number ($E_{\pi\pi} < 2M_\pi$).

5.5 $K \to \pi\pi(I = 2)$ Result with G-parity Boundary and H-parity Boundary

In this section we describe one of the cross-checks on our measurement code, by comparing the result using G-parity boundary conditions with that obtained using H-parity boundary conditions.

When calculating the $K \to \pi\pi(I = 2)$ decay amplitude, G-parity is not the only way to give correct kinematics to the $\pi\pi$ ground state. For example in Ref. [1], anti-periodic spatial boundary condition is imposed on the d quark only (also known as "H-parity boundary conditions"), in order to give momentum of π/L (L is the spatial extend of the lattice) for the charged pions $\pi^\pm$.

Note that H-parity boundary conditions cannot be used to calculate the $K \to \pi\pi(I = 0)$ decay. This is because under H-parity boundary conditions, the momentum of $\pi^\pm$ meson is odd multiple of π/L while the momentum of π^0 meson is even multiple π/L, breaking the degeneracy between $\pi^\pm$ and π^0. Since the $(I = 0)$ $\pi\pi$ state involves both $\pi^\pm$ and π^0, it is no longer an energy eigenstate. In this section, we only introduce an H-parity boundary to compare the $K \to \pi\pi(I = 2)$ result between that obtained using H-parity and G-parity boundaries, as a cross check of the G-parity method. The binary code using H-parity boundary conditions was written by Hantao Yin, and the corresponding measurement is done on the same 16nt32 ensemble except without a G-parity boundary [18]. The comparison of correlation functions is shown in Figures E.2, E.3, and E.4. The comparison of fitted values are in Table 5.6.

For both boundary conditions, the time separation between kaon and $\pi\pi$ are 12 and the

Q_i	G-parity	H-parity
1	7.6(12)e-04	8.17(10)e-04
7	5.30(30)e-03	5.220(50)e-03
8	2.04(10)e-02	2.006(18)e-02
1	1.17(11)e-03	1.205(36)e-03
7	5.16(31)e-03	5.10(13)e-03
8	2.137(98)e-02	2.160(53)e-02
1	1.92(19)e-03	2.10(12)e-03
7	6.41(45)e-03	6.03(32)e-03
8	2.98(16)e-02	2.91(15)e-02

Table 5.6: Fitting results for $\langle \pi\pi | Q_i | K \rangle$. Upper part: one G-parity (or H-parity) twist; Middle part: two G-parity (or H-parity) twists; Lower part: three G-parity (or H-parity) twists. We used a fitting range of $T(Q_i - \pi\pi) = [4 : 8]$. The time separation $T(K - \pi\pi) = 12$. The number of measurements for G-parity with 1,2,3 twists are 17,73,41 respectively; Numbers of measurements for H-parity with 1,2,3 twists are 200,106,119 respectively. Time translation averaging was done on only every 8th time slice for 1 and 2 G-parity twists; Time translation averaging was done on every time slice for all other measurements.

valance quark masses are $m_l = 0.01$, $m_s = 0.099$. In the G-parity boundary case, because of using the all-to-all propagators (see Chapter 4), the two pions are separated by 4 in the time direction with their distances to the kaon of 12 and 16 respectively. These results show a good agreement between the use of G-parity boundary and H-parity boundary, for the $K \to \pi\pi(I = 2)$ decay. Note that in the H-parity boundary condition case, the quark field doesn't involve any two-flavor notation, and the Wick contractions are totally different from those appearing in the G-parity boundary condition case. Another difference is in the propagator source: the measurement with H-parity twist are done using a "cosine" wall source, while the measurement with G-parity are carried out using all-to-all propagators to construct hydrogen-wave-function-like mesons.

We also carried out the same comparison but replacing the usual DWF by Möbius DWF with $L_s = 16$, using 3 G-parity twists and 3 H-parity twists, as in Figure E.5 and Table 5.7. This comparison also shows a good agreement between the use of G-parity boundary and H-parity boundary.

Q_i	G-parity	H-parity
1	1.70(20)e-03	1.85(16)e-03
7	6.89(70)e-03	5.73(52)e-03
8	2.96(28)e-02	2.71(25)e-02

Table 5.7: Fitting results for $\langle \pi\pi | Q_i | K \rangle$, with three G-parity (or H-parity) twists. Used a fitting range of $T(Q_i - \pi\pi) = [4 : 8]$. The time separation $T(K - \pi\pi) = 12$. The numbers of measurements for G-parity is 71, while the numbers of measurements for H-parity is 66. A time translation averaging is done on only every 8th time slice for the G-parity results.

5.6 Free Field Check

In order to further check the propagators and the contraction formula for each correlation function on G-parity case, we compared the free field (i.e. unit matrix for every SU(3) gauge link) results with the G-parity boundary and with the usual periodic boundary. These two results should be identical in the infinite volume limit or in the heavy quark mass limit, since in both limits the quark propagator can't go far enough to detect the boundary.

We made the comparison on a free 16nt32 lattice and also on a free 24nt32 lattice, both with DWF action (no Möbius, $L_s = 16$), valance light and strange quark are 0.3. With each lattice size, we used (1 spatial G-parity boundary + 2 spatial periodic boundaries + 113-degree-twisted temporal boundary) to calculate the full $K \to \pi\pi$(I=0) result, and did the same thing using (3 spatial periodic boundaries + 113-degree-twisted temporal boundary), then their comparison on each of the 2-point or 3-point correlation functions are plotted. The twisted temporal boundary condition is to make those graphs with quark self-loop contribute to the decay matrix elements. For the $K \to \pi\pi$ 3 point function, the kaon to $\pi\pi$ separation are set to 12. The two pions in the $\pi\pi$ source are separated by 4 time slices. The Meson field wave functions in all-to-all propagators are point-like ($r \to 0$). In order to compare to a high precision, no low-modes are used in all-to-all propagators. The random numbers in high mode part are set all 0 except the sites with $x = y = z = 0$ are set to 1.

The comparison are shown in Figure E.6 to E.37. From these plots, the results using G-parity and periodic boundaries agree very well and the agreement on 24nt32 lattice is

even better than that on 16nt32 lattice, which shows the decreasing effect of the boundary conditions when volume gets larger.

Chapter 6

Results from $32^3 \times 64 \times 12$ Lattice

After the trial calculation has been conducted on the 16nt32 ensemble with unphysical pion and kaon masses, we are ready to calculate the physical decay amplitude A_0. We descibe the various optimizations that have been done to speed up the measurement; and then show the result for pion-pion scattering, the decay amplitude A_0, and ϵ'/ϵ; lastly, we estimate the effect of not having physical kinematics and not directly including charm on lattice.

6.1 Gauge Ensembles

For the physical ensemble, we used 2+1 dynamic flavors of DWF and Iwasaki+DSDR[34] gauge action, with $\beta = 1.75$ and $a^{-1} = 1.379(7)$GeV. The lattice size is $32^3 \times 64 \times 32$. For the fifth dimension, we have used an improved DWF formalism (the Möbius DWF[17]) and reduced the L_s from 32 to 12 by choosing the Möbius parameters $(b+c) = 32/12$, $(b-c) = 1$. The sea quark masses are $m_{u/d} = 0.0001$ and $m_s = 0.045$. All these parameters are chosen to match the physical pion and kaon masses, found from our earlier ensemble in Ref. [25]. G-parity boundary conditions are applied to all 3 spatial directions, the measured ground state pion energy ≈275 MeV and the kaon mass ≈490 MeV.

6.2 Computational Details

We used the unitary valance quark masses on 216 configurations, and another heavier valance strange quark mass of 0.0495 on 69 configurations in order to check the dependence of the final result on the kinematics. These 216 configurations are each separated by 4 units of molecular dynamics time. The autocorrelation length for $K \to \pi\pi$ matrix elements turns out to be shorter than 4, by looking at the results with different bin sizes, in Table F.1. The measurements starts on the 300th time unit for equilibrium. Different bin sizes are tried to make sure there is no auto-correlation. The light quark all-to-all propagators use 900 low modes and 1 random hit on each lattice site with time-spin-color-flavor dilution. The strange quark all-to-all propagators use no low modes and the same number of random vectors as those for the light quark. The Lanczos algorithm uses the parameters $\alpha = 15, \beta = 0.07$ and Chebyshev order $n = 200$. Deflation using the 900 low modes has accelerated the CG significantly, the reduction in CG iteration number is shown in Figure 6.1

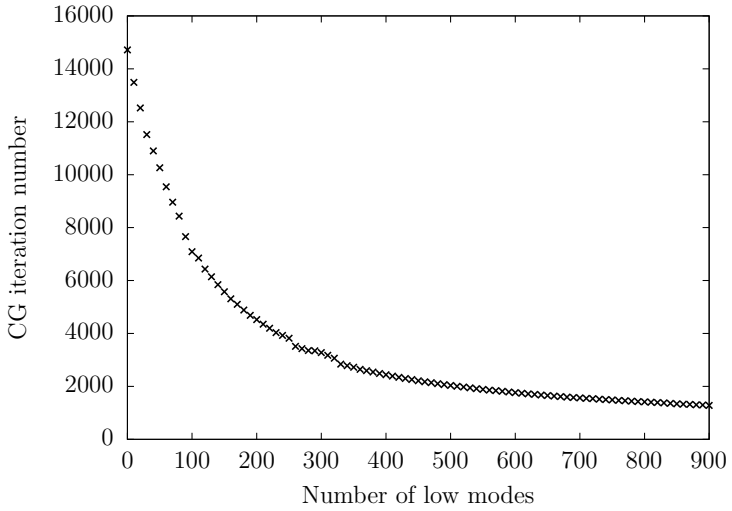

Figure 6.1: CG iteration number depending on number of low modes used for deflation.

The computation is done on a half-rack IBM Blue Gene/Q computer with the bagel fermion matrix package [35]. The time for one full measurement is ≈20 hours and breaks

	time
Lanczos (900 eigen vectors)	3.6h
Light quark CG (900 modes deflation)	4.6h
Strange quark CG	2.9h
Gauge fixing	0.33h
Computing meson field(900 low modes)	3.0h
Pion(s),Kaon spectrum	1.1h
Type1 contraction	0.79h
Type2 contraction	0.54h
Type3 contraction	1.97h
Type4 contraction	0.50h
Total	$\sim$19.5h

Table 6.1: Computational time for one full $K \to \pi\pi(I = 0)$ measurement on the 32nt64 ensemble. On 512-node IBM Blue Gene/Q computer.

down into the times shown in Table 6.1. Several optimizations have already been implemented:

- Defect correction solver [36] is used to speed up the solving of Dirac equation, by reducing most of the double precision operations to single precision.

- Multi-dimension fast Fourier transformation (FFT) is used to evaluate the meson field in Equation 4.32. The $\vec{v}$ and $\vec{w}$ vectors in all-to-all propagators are distributed on different nodes (otherwise the memory on each single node is not sufficient to hold all these vectors), each node holds a fraction of data in every space-time direction. To speed up the communication, we wrote the multi-dimension FFT such that each 1-dimension FFT is done sequentially, which reduces the communication time to be proportional to the number of computer nodes in each one direction. This is based on the 4D torus structure of the IBM Blue Gene/Q computer.

- We utilized the single-instruction-multiple-data (SIMD) feature of the PowerPC processor in the Blue Gene/Q computer, which delivers four floating point operations per CPU cycle, reducing the time of contracting the propagators that form the $K \to \pi\pi$

three-point functions by nearly a factor of 4. As stated in Chapter 4, the complexity of evaluating $K \to \pi\pi$ three-point function is (Mode Number)$^2\times$(Volume)$\times$(T size)$\times 24^2$. The mode number for the light quark is 2436, the volume is $32^3 \times 64$, T is 64, the total number of floating point operation is $\approx 10^{17}$, which is non-trivial and the SIMD does help a lot.

- Because the high mode $\vec{w}$ vectors in all-to-all propagators are time-spin-color-flavor diluted, most components in these $\vec{w}$ vectors are zero. To save time, any calculation involving these zero components are avoided.

- The amount of statistics collected for different parts of computation is adjusted to achieve more efficiency. The type 1 and 2 graphs in $K \to \pi\pi$ fluctuate much less than type 4 graphs but they consume more time than type 4 graphs, so we choose to do time translation on every the 8th time slice for type 1 and type 2 diagram, and every time slice for type 3 and type 4 graphs. Although Type 3 is more expensive than Type 4, it contains a quark self-loop as does Type 4 and is quite noisy, so we choose not to reduce the statistics for the Type 3 graphs. The same optimization is used in $\pi\pi$ scattering, where the 'Vacuum' graph is the main source of noise but consumes less time than the other graphs, so we do the time translation on every time slice for vacuum graph but only translate on every 8th time slice for the other 'Direct', 'Cross', and 'Rectangle' graphs.

6.3 Meson spectrum and $\pi\pi$ scattering phase shift

The effective energy plot for kaon, pion, and $\pi\pi(I = 0, 2)$ states are in Figures F.1, F.2, and F.3. The fitted energy is shown in Table 6.2.

Note that the δ_2 phase shift in Table 6.3 is not the phase shift at physical kinematics since $E_{\pi\pi(I=2)} > m_K$ in this work. In the physical $K \to \pi\pi$(I=2) decay channel, the pion-pion

units	$m_K^{(0)}$	$m_K^{(1)}$	E_π	$E_{\pi\pi(I=2)}$	$E_{\pi\pi(I=0V)}$	$E_{\pi\pi(I=0)}$
lattice	0.35567(16)	0.37168(27)	0.19923(28)	0.41553(50)	0.3550(12)	0.3613(74)
MeV	490.47(22)	512.55(37)	274.74(39)	573.02(69)	485.5(17)	498(10)

Table 6.2: Meson spectrum measured on 32nt64 ensemble. The super script (0), (1) on kaon mass corresponds to two valance strange quark mass, m_s=0.045, and 0.0495. The $m_K^{(1)}$ is measured on 69 configurations while all the other quantities are measured on 216 configurations.

$p_{I=2}$ (lattice)	$\delta_2(p_{I=2})$ (rad)	$p_{I=0}$ (lattice)	$\delta_0(p_{I=0})$ (rad)
0.17997(31)	-0.1875(59)	0.1479(46)	0.416(85)
$p_{I=2}$ (MeV)	$\delta_2(p_{I=2})$(degree)	$p_{I=0}$ (MeV)	$\delta_0(p_{I=0})$(degree)
248.18(43)	-10.74(34)	204.0(63)	23.8(49)

Table 6.3: pion-pion scattering phase shifts measured on 32nt64 ensemble. $p_{I=2,0}$ are calculated from $p_I = \sqrt{E^2_{\pi\pi(I)}/4 - M^2_\pi}$, and $M_\pi = \sqrt{E^2_\pi - N_{tw}(\frac{\pi}{L})^2}$. N_{tw} is number of G-parity twists.

scattering phase shift is measured to be $\delta_2 = -11.6(2.5)(1.2)$ degree, which is a corrected value of the continuum result obtained in Ref. [8]. Combining the δ_2 with δ_0 from this work (see Table 6.3):

$$\delta_0 - \delta_2 = 23.9(4.9) + 11.6(2.5)(1.2) = 35.5(5.6) \text{ degree} \tag{6.1}$$

If we use this value to approximate the arg(A_0)-arg(A_2) (i.e. neglecting the CP-violating phases in A_0 and A_2), it's about 2σ diffenrent from the conventional value given in Equation 2.38. But the actual distance with our current statistics is surely less than 2σ since a number of other sources of error are not considered, for example the error of experimental arg(A_0)-arg(A_2), the discretization error in lattice result for δ_0 result, and the QED interaction is absent in our current lattice calculation.

Remember that the phase shift formula 5.3 assumes that the scattering phase shifts $\delta_l(p)$ are near zero for $l > 0$. As a sanity check, we measured the energy for the following pipi

states:

$$\pi\pi_{D1-wave} = \frac{1}{\sqrt{3}}\left(|\pi_{-++}\pi_{+--}\rangle + e^{\frac{2\pi}{3}i}|\pi_{+-+}\pi_{-+-}\rangle + e^{\frac{4\pi}{3}i}|\pi_{++-}\pi_{--+}\rangle\right) \quad (6.2)$$

$$\pi\pi_{D2-wave} = \frac{1}{\sqrt{3}}\left(|\pi_{-++}\pi_{+--}\rangle + e^{\frac{4\pi}{3}i}|\pi_{+-+}\pi_{-+-}\rangle + e^{\frac{2\pi}{3}i}|\pi_{++-}\pi_{--+}\rangle\right) \quad (6.3)$$

$$\pi\pi_{D3-wave} = \frac{1}{\sqrt{12}}\left(3|\pi_{+++}\pi_{---}\rangle - |\pi_{-++}\pi_{+--}\rangle - |\pi_{+-+}\pi_{-+-}\rangle - |\pi_{++-}\pi_{--+}\rangle\right) \quad (6.4)$$

The subscript of each pion describes it's momentum orientation. They are all orthogonal to the s-wave ground state:

$$\pi\pi_{s-wave} = \frac{1}{\sqrt{4}}\left(|\pi_{+++}\pi_{---}\rangle + |\pi_{-++}\pi_{+--}\rangle + |\pi_{+-+}\pi_{-+-}\rangle + |\pi_{++-}\pi_{--+}\rangle\right) \quad (6.5)$$

The measured energies are shown in Figure F.4 and F.5. The s-wave pipi state is the one we use to extract the ground state energy $E_{\pi\pi}$. As can be seen from the figures, the s-wave pipi energy is significantly different from $2E_\pi$ while the other d-wave have $E_{\pi\pi} \approx 2_\pi$, this shows only s-wave scattering occurs and the pion-pion interaction with higher angular momentum is much weaker.

6.4 $K \to \pi\pi(I = 0)$ Amplitude

When calculating the 3-point correlation function $\langle \pi\pi(I = 0)|Q_i|K\rangle$, we fixed the kaon to pipi separations and let the weak operator vary over the time slices in between. This time separation has to be large enough such that the weak operator is at sufficient distance from both kaon and pipi, that little excited state contamination occurs. On the other hand this time separation can't be too large, since the noise will grow and there may be contamination from the around-the-world effect [18]: the unexpected $K\pi \to \pi$ process when one pion travels from weak operator to $\pi\pi$ sink while the other pion travels forward in time and wraps over to the weak operator.

In this work, we used the kaon to $\pi\pi$ separation of 10, 12, 14, 16, 18. For each separation, we used the data points where the weak operator Q_i is at least 4 time slices away from the $\pi\pi$ operator and 6 time slices away from the kaon operator, to avoid excited state contamination.

The way we treat the operator mixing with lower dimension $\bar{s}\gamma_5 d$ is the same as in the previous work [28]. The quark self-loop in Type 3 and Type 4 graphs contains a $1/a^2$ divergence, which arises from this mixing and needs to be subtracted. The subtraction coefficients are determined from the condition:

$$\langle 0|Q_i - \alpha_i \bar{s}\gamma_5 d|K\rangle = 0 \tag{6.6}$$

Using the equations of motion, $\bar{s}\gamma_5 d$ term is proportional to $\partial_\mu(\bar{s}\gamma_5\gamma^\mu d)$, which vanishes when the initial kaon and final $\pi\pi$ have the same energy and momentum. Note that $\bar{s}\gamma_5 d$ is not a translational invariant operator (even if we sum over the spatial position), because we didn't include $\bar{u}\gamma_5 s'$, the G-parity transformation of the $\bar{s}\gamma_5 d$ operator, in above equation. We omitted the $\bar{u}\gamma_5 s'$ piece because the Q_i also doesn't contain its G-parity transformation of itself (which has the fictional s' quark in it), so $\bar{s}\gamma_5 d$ is more correlated to the divergence piece in Q_i. Leaving out the $\bar{u}\gamma_5 s'$ piece is justified since we have used a translational invariant kaon source in the correlation function $\langle 0|\bar{s}\gamma_5 d|K\rangle$, and we don't have to translate $\bar{s}\gamma_5 d$ crossing the G-parity boundary.

The ten 3-point correlation functions $e^{E_K*(t_Q-t_K)}e^{E_{\pi\pi}*(t_{\pi\pi}-t_Q)}\langle K|Q_i|\pi\pi(I=0)\rangle$ are shown in Figure F.6 to F.15. The exponential factors in front is to compensate for the energy difference between kaon and pipi state, and to provide an easily recognized plateau in these graphs. Each data point in these graphs are the error weighted average of the 5 different kaon to $\pi\pi$ separations. The fitted 10 weak matrix elements are given in Table 6.4.

To get the final A_0 result, we used the RI/SMOM($\not{q},\not{q}$) intermediate scheme with parity-odd projectors for the NPR procedure (see Appendix C for NPR results). The $\overline{\text{MS}}$ Wilson coefficients are listed in Table A.3. The final A_0 result and its contributions from each of

the ten $\overline{\text{MS}}$ operators are in Table 6.5.

i	$M_i^{1/2,lat}$
1	-3.94(1.00) $\times 10^{-3}$
2	4.23(1.14) $\times 10^{-3}$
3	-1.02(2.91) $\times 10^{-3}$
4	7.08(3.01) $\times 10^{-3}$
5	-9.58(2.35) $\times 10^{-3}$
6	-1.89(0.46) $\times 10^{-2}$
7	2.11(0.14) $\times 10^{-2}$
8	7.40(0.28) $\times 10^{-2}$
9	-5.49(1.56) $\times 10^{-3}$
10	2.81(1.59) $\times 10^{-3}$

Table 6.4: $M_i^{1/2,lat}$ from the 32nt64 G-parity ensemble. Averaged over $K-\pi$ separation of 10, 12, ..., 18.

i	Re(A_0)(GeV)	Im(A_0)(GeV)
1	1.02(0.20)(0.07) $\times 10^{-7}$	0
2	3.63(0.91)(0.28) $\times 10^{-7}$	0
3	-1.19(1.58)(1.12) $\times 10^{-10}$	1.54(2.04)(1.45) $\times 10^{-12}$
4	-1.86(0.63)(0.33) $\times 10^{-9}$	1.82(0.62)(0.32) $\times 10^{-11}$
5	-8.72(2.17)(1.80) $\times 10^{-10}$	1.57(0.39)(0.32) $\times 10^{-12}$
6	3.33(0.85)(0.22) $\times 10^{-9}$	-3.57(0.91)(0.24) $\times 10^{-11}$
7	2.40(0.41)(0.00) $\times 10^{-11}$	8.55(1.45)(0.00) $\times 10^{-14}$
8	-1.33(0.04)(0.00) $\times 10^{-10}$	-1.71(0.05)(0.00) $\times 10^{-12}$
9	-7.12(1.90)(0.46) $\times 10^{-12}$	-2.43(0.65)(0.16) $\times 10^{-12}$
10	7.57(2.72)(0.71) $\times 10^{-12}$	-4.74(1.70)(0.44) $\times 10^{-13}$
Tot	4.66(0.96)(0.27) $\times 10^{-7}$	-1.90(1.19)(0.32) $\times 10^{-11}$

Table 6.5: Contributions to A_0 from the ten $\overline{\text{MS}}$ operators Q_i averaged over $K-\pi\pi$ separations of 10, 12, ..., 18; Two statistical errors are shown: one from the lattice matrix element (left) and one from the lattice to RI matching matrix (right).

From table 6.5, our final A_0 result is:

$$\text{Re}(A_0) = 4.66(0.96)(0.27) \times 10^{-7} \text{ GeV} \tag{6.7}$$

$$\text{Im}(A_0) = 1.90(1.19)(0.32) \times 10^{-11} \text{ GeV} \tag{6.8}$$

The NPR calculation is much cheaper than that for the lattice matrix elements and the corresponding error (the second error in Table 6.5) can be reduced rather easily.

6.5 ϵ'/ϵ

The ratio ϵ'/ϵ is determined by:

$$\frac{\epsilon'}{\epsilon} = \frac{i\omega e^{\delta_2-\delta_0}}{\sqrt{2}\epsilon}[\frac{\mathrm{Im}A_2}{\mathrm{Re}A_2} - \frac{\mathrm{Im}A_0}{\mathrm{Re}A_0}] \tag{6.9}$$

We now have all the ingredients to calculate this ratio: $\omega(\equiv \mathrm{Re}(A_2)/\mathrm{Re}(A_0))$ and ϵ from experiments, δ_2, A_2 from lattice calculation in Ref [8] (for δ_2 we have used a corrected value 11.6(2.5)(1.2) degree). $\mathrm{Im}(A_0)$ is from this work. In order to have a more accurate result, we also use the experimental value for $\mathrm{Re}(A_0)$. Eventually, we get:

$$\mathrm{Re}(\frac{\epsilon'}{\epsilon}) = 1.38(5.08) \times 10^{-4}, \tag{6.10}$$

Note that several large systematic errors in the lattice calculation are not yet considered. We'll discuss them in the next few sections as well as in Chaper 7.

6.6 Evaluating LL factor

As explained in Chapter 3, the Lellouch-Lüscher (LL) factor relates the lattice matrix elements to that in infinite-volume. The LL factor as in Equation 3.62 is $\frac{1}{\pi q}\sqrt{\frac{\partial\phi}{\partial q} + \frac{\partial\delta}{\partial q}}\sqrt{m_K}E_{\pi\pi}L^{2/3}$ and we have used linear approximation to evaluate the partial derivative of δ: $\partial\delta/\partial p \approx \delta/p$. But this approximation doesn't necessarily hold, especially when pions carry such large momentum and p value is large (see Table 6.3).

In order to estimate the systematic error for this approximation, we use a second way to approximate $\partial\delta/\partial p$ and compare the difference in final LL factor, which is by assuming the

phase shift δ_0 is linear in $E_{\pi\pi(I=0)}$. This is suggested by the phenomenological result for the pion-pion scattering phase shift in Ref [37]. Using this approximation, we'll have:

$$\begin{aligned}\frac{\partial\delta}{\partial q} &= \frac{\partial\delta}{\partial E_{\pi\pi}}\frac{\partial E_{\pi\pi}}{\partial q} \\ &= \frac{\delta}{E_{\pi\pi}-2m_\pi}\frac{\partial E_{\pi\pi}}{\partial q} \\ &= \frac{\delta}{E_{\pi\pi}-2m_\pi}\frac{4q}{E_{\pi\pi}}\left(\frac{2\pi}{L}\right)^2 \end{aligned} \tag{6.11}$$

The comparison using these two approximations, as well as neglecting δ contribution, are in Table 6.6. The relative difference in LL factor using these three approximations is at most 11%.

	$\partial\phi/\partial q$	$\partial\delta/\partial q$	$\sqrt{\partial\phi/\partial q+\partial\delta/\partial q}$
Assuming $\delta\propto p$	3.6708(55)	0.55(13)	2.055(30)
Assuming $\delta\propto E_{\pi\pi}$	3.6708(55)	0.87(21)	2.131(48)
Assuming $\partial\delta/\partial q=0$	3.6708(55)	0	1.9159(14)

Table 6.6: Comparing the difference in LL factor, by treating δ linear in p, linear in $E_{\pi\pi}$, and equal to 0. Assuming $\delta\propto p$ gives $\partial\delta/\partial q=\delta/q$. Assuming $\delta\propto E_{\pi\pi}$ gives Equation 6.11.

6.7 Effect of Unphysical Kinematics

The $\bar{s}\gamma_5 d$ subtraction relies on the on shell condition of the decay, so it's important that the kaon and the $\pi\pi$ states have the same energy. With the unitary $m_{u/d}=0.0001$ and $m_s 0.045$ values, the kaon mass turns out to be a little lower than $\pi\pi$ energy (see Table 6.2). To estimate the effect of this energy non-conservation, we have used the second valance quark mass $m_s=0.0495$, and repeated the same $K\to\pi\pi$ measurement on 69 configurations. The unitary kaon mass is labeled as $m_K^{(0)}$, the kaon mass with $m_s=0.0495$ is labeled as $m_K^{(1)}$. The heavier strange quark mass is chosen such that the energy conserving kaon mass lies between the two kaon masses we have. As a side remark, the kaon mass with this 10%

heavier strange quark mass is ≈5% heavier than unitary kaon mass, which is in accordance with chiral perturbation theory. The comparison of lattice matrix elements calculated from the two strange quark masses are in Table F.3. As can be seen, the largest, and statistically resolved discrepancy for Q_i in Table F.3 is ≈8%, combining with the ≈2% miss match between $m_K^{(0)}$ and $E_{\pi\pi(I=0)}$, we estimate the effect of unphysical kinematics to be ≤3%.

6.8 Estimation of Charm Quark Contribution

For the A_0 result in this work, we have only considered the 3-flavor (up, down, strange) QCD on the lattice. The effects of the other 3 flavors are included in the perturbative $\overline{\text{MS}}$ Wilson coefficients at the energy scale 1.53 GeV, which is not so high above charm threshold and raises the question of how much systematic error is introduced from neglecting charm quark on the lattice. Although we didn't include a valence charm quark in H_W or the $K \to \pi\pi$ contractions, we can estimate the charm quark contribution by examining the graphs in which charm quark could appear.

The charm quark enters the 4-flavor weak Hamiltonian $H_W^{(4f)}$ through a term of in the form of $(\bar{s}d)(\bar{c}c)$, since both kaon and $\pi\pi$ operators don't contain any valence charm quarks, the charm and anti-charm fields in $H_W^{(4f)}$ must contract with each other, leaving a contraction graph that looks like the Type 3 or Type 4 graph in 3-flavor $K \to \pi\pi$. Suppose we now do a 4-flavor $K \to \pi\pi$ calculation for the operator Q6 (which contributes most to the imaginary A_0 among all 10 weak operators) without disconnected graphs, the only new contribution besides the existing 3-flavor contractions is the:

$$
\begin{aligned}
& \langle\pi\pi(I=0)|Q_6^{(c-loop)}|K\rangle_{conn} - \frac{\langle 0|Q_6^{(c-loop)}|K\rangle}{\langle 0|\bar{s}\gamma_5 d|K\rangle}\cdot\langle\pi\pi(I=0)|\bar{s}\gamma_5 d|K\rangle_{conn} \\
= \quad & \frac{3}{\sqrt{6}}\cdot Tr_c\{Tr_{s,f}\{\Gamma_1\mathcal{G}^{(L)}_{x_{op},x_{\pi_1}}S_2\mathcal{G}^{(L)}_{x_{\pi_1},x_{\pi_2}}S_2\mathcal{G}^{(L)}_{x_{\pi_2},x_K}\gamma_5\mathcal{G}^{(s)}_{x_K,x_{op}}\}\cdot Tr_{s,f}\{\Gamma_2\mathcal{G}^{(c)}_{x_{op},x_{op}}\}\} \\
- \quad & \frac{3}{\sqrt{6}}\cdot\frac{Tr_c\{Tr_{s,f}\{\Gamma_1\mathcal{G}^{(L)}_{x_{op},x_K}\gamma_5\mathcal{G}^{(s)}_{x_K,x_{op}}\}\cdot Tr_{s,f}\{\Gamma_2\mathcal{G}^{(c)}_{x_{op},x_{op}}\}\}}{Tr\{F_0\gamma_5\mathcal{G}^{(L)}_{x_{op},x_K}\gamma_5\mathcal{G}^{(s)}_{x_K,x_{op}}\}} \\
\times \quad & Tr\{F_0\gamma_5\mathcal{G}^{(L)}_{x_{op},x_{\pi_1}}S_2\mathcal{G}^{(L)}_{x_{\pi_1},x_{\pi_2}}S_2\mathcal{G}^{(L)}_{x_{\pi_2},x_K}\gamma_5\mathcal{G}^{(s)}_{x_K,x_{op}}\}
\end{aligned}
\tag{6.12}
$$

where $\mathcal{G}^{(L)}$ is u/d quark propagator, $\mathcal{G}^{(s)}$ is strange quark propagator, $\mathcal{G}^{(c)}$ is charm quark propagator, $\Gamma_1 = F_0\gamma_u(1-\gamma_5)$ and $\Gamma_2 = F_0\gamma^u(1+\gamma_5)$. Q_6^{c-loop} is the part of 4-flavor Q_6 that contains $\bar{c}c$. The subscript $\langle\ldots\rangle_{conn}$ denotes the fact that disconnected Type 4 graphs are not considered when evaluating the correlation function, which is for better resolution.

In order to estimate the size of the expression in Equation 6.12, we can replace the charm quark loop in expression 6.12 by either light quark loop or strange quark loop , which we have evaluated in the 3-flavor $K\to\pi\pi$ calculation, and then compare their sizes. Hopefully it could allow us to extrapolate to the expression 6.12 with charm quark loop. To be more concrete, We want to check the size of:

$$
\begin{aligned}
& \frac{3}{\sqrt{6}}\cdot Tr_c\{Tr_{s,f}\{\Gamma_1\mathcal{G}^{(L)}_{x_{op},x_{\pi_1}}S_2\mathcal{G}^{(L)}_{x_{\pi_1},x_{\pi_2}}S_2\mathcal{G}^{(L)}_{x_{\pi_2},x_K}\gamma_5\mathcal{G}^{(s)}_{x_K,x_{op}}\}\cdot Tr_{s,f}\{\Gamma_2\mathcal{G}^{(L)}_{x_{op},x_{op}}\}\} \\
- \quad & \frac{3}{\sqrt{6}}\cdot\frac{Tr_c\{Tr_{s,f}\{\Gamma_1\mathcal{G}^{(L)}_{x_{op},x_K}\gamma_5\mathcal{G}^{(s)}_{x_K,x_{op}}\}\cdot Tr_{s,f}\{\Gamma_2\mathcal{G}^{(L)}_{x_{op},x_{op}}\}\}}{Tr\{F_0\gamma_5\mathcal{G}^{(L)}_{x_{op},x_K}\gamma_5\mathcal{G}^{(s)}_{x_K,x_{op}}\}} \\
\times \quad & Tr\{F_0\gamma_5\mathcal{G}^{(L)}_{x_{op},x_{\pi_1}}S_2\mathcal{G}^{(L)}_{x_{\pi_1},x_{\pi_2}}S_2\mathcal{G}^{(L)}_{x_{\pi_2},x_K}\gamma_5\mathcal{G}^{(s)}_{x_K,x_{op}}\}
\end{aligned}
\tag{6.13}
$$

and the size of:

$$\begin{aligned}
& \frac{3}{\sqrt{6}} \cdot Tr_c\{Tr_{s,f}\{\Gamma_1 \mathcal{G}^{(L)}_{x_{op},x_{\pi_1}} S_2 \mathcal{G}^{(L)}_{x_{\pi_1},x_{\pi_2}} S_2 \mathcal{G}^{(L)}_{x_{\pi_2},x_K} \gamma_5 \mathcal{G}^{(s)}_{x_K,x_{op}}\} \cdot Tr_{s,f}\{\Gamma_2 \mathcal{G}^{(s)}_{x_{op},x_{op}}\}\} \\
- \quad & \frac{3}{\sqrt{6}} \cdot \frac{Tr_c\{Tr_{s,f}\{\Gamma_1 \mathcal{G}^{(L)}_{x_{op},x_K} \gamma_5 \mathcal{G}^{(s)}_{x_K,x_{op}}\} \cdot Tr_{s,f}\{\Gamma_2 \mathcal{G}^{(s)}_{x_{op},x_{op}}\}\}}{Tr\{F_0 \gamma_5 \mathcal{G}^{(L)}_{x_{op},x_K} \gamma_5 \mathcal{G}^{(s)}_{x_K,x_{op}}\}} \\
\times \quad & Tr\{F_0 \gamma_5 \mathcal{G}^{(L)}_{x_{op},x_{\pi_1}} S_2 \mathcal{G}^{(L)}_{x_{\pi_1},x_{\pi_2}} S_2 \mathcal{G}^{(L)}_{x_{\pi_2},x_K} \gamma_5 \mathcal{G}^{(s)}_{x_K,x_{op}}\}
\end{aligned} \tag{6.14}$$

Since the charm quark contribution is not a physical decay amplitude, we show the time dependence of expressions 6.13 and 6.14 instead of fitting them, in Table F.4. According to Table F.4, the difference between the light quark self-loop and the strange quark self-loop can not be clearly resolved. Furthermore, this specific contribution is only a small fraction of the contribution from all Type1, 2, 3, and 4 contribution, namely 10% (with a sign opposite to that of the full result), so it's expected that the charm quark reduces the Q_6 magnitude by about 10%. On the other hand, from Table F.2 the magnitude of the $\overline{\text{MS}}$ Wilson coefficient for Q_6 goes up by $\approx$16% when going the 3-flavor to the 4-flavor theory. As a result, the relative change of Q_6 contribution to A_0 (which is the product of Wilson coefficients and decay matrix elements) is $(1 - 10\%)(1 + 16\%) - 1 \approx 4\%$. Since Q_6 is the major contributor to $Im(A_0)$, we expect the change in $Im(A_0)$ from adding an active charm quark is not a concern, given the current 3-flavor statistical error.

Chapter 7

Conclusions

We have demonstrated the successful use of G-parity boundary conditions and all-to-all propagators:

- G-parity boundary conditions were well tested on 16nt32 lattice and gave the expected kinematics of the $\pi\pi$ state. Although these boundary conditions, even when applied to all three directions, break the cubic rotation symmetry at the quark level, the pion propagator is not affected significantly. The fictional strange quark s' that we introduced also proves successful for constructing a static kaon state. The agreement between the $K \to \pi\pi$(I=2) results using G-parity and H-parity boundary conditions is further strong evidence of the correctness of the G-parity boundary condition technique, given that H-parity technique is well understood and has given a physical value for A_2 [8], that agrees with the experimental result.

- All-to-all propagators were tested on the 16nt32 ensembles and proved to be superior to the traditional wall-source-wall-sink propagator: the results for $E_{\pi\pi}$(I=0) and Im(A_0) showed a factor of 2 decrease in their errors. The use of all-to-all propagators also significantly saved CG time on the 32nt64 ensemble, since the various momentum directions of quarks did not require additional inversions of Dirac operator with

all-to-all propagators. Although all-to-all propagators make the 3-point functions expensive to evaluate, we have managed to compensate for that by implementing several computational optimizations and improving the sampling strategy.

G-parity boundary conditions removes the stationary pion state and introduces correct kinematics for the ground $\pi\pi$ state, and the use of all-to-all propagators suppresses the fluctuations from disconnected graphs, increasing computational efficiency. These techniques have enabled us to calculate A_0 and $\mathrm{Re}(\epsilon'/\epsilon)$ at physical kinematics, an important step beyond our earlier threshold calculation in Ref [28]. Much other technical progress in the past few years is also crucial in this work. To name a few: the DWF action making the operator mixing pattern easy to handle, the 100-teraflops-scale super computer and superior software package allowing us to simulate the physical light quarks on the lattice.

In Chapter 6, we showed the result for kaon decay amplitude A_0 and the ratio of ϵ'/ϵ. They are calculated from a $32^3 \times 64$ lattice, which corresponds to a box $\approx$4.8fm on a side, with a physical pion mass (140 MeV) and kaon mass (490 MeV). The energy of $\pi\pi$(I=0) state is $\approx$498 MeV, corresponding to the near-physical kinematics. It's the first time that a calculation of A_0 with physical quark masses and kinematics has been possible to compute on the lattice. Although the statistical error is large with our current 216 measurements, the $\mathrm{Re}(A_0)$ agrees with experimental result, and $\mathrm{Re}(\epsilon'/\epsilon)$ evaluates to

$$\mathrm{Re}(\frac{\epsilon'}{\epsilon}) = 1.38(5.08) \times 10^{-4}, \tag{7.1}$$

which agrees at the 2σ level (after considering all other systematic errors which will be explained below) with experimental result $1.66(0.23) \times 10^{-3}$.

To further improve the calculation, besides increasing the statistics, we have to examine and reduce all systematic errors. In Chapter 3, we have estimated the systematic error in $Lat \to \overline{\mathrm{MS}}$ operator matching procedure (the similar work was done in an earlier work [8]). In Chapter 6 we have examined: 1.the effect of unphysical kinematics, 2.the effect of leaving

charm contribution to perturbation theory. 3.the systematic error in LL factor.

There are still other systematic errors:

- Finite lattice spacing. The lattice regularization introduces a systematic errors of order $O(a^2)$, also known as lattice artefacts. We estimate this error by comparing our earlier $K \to \pi\pi$(I=2) result [38] with the result in the continuum limit result [8]. The $K \to \pi\pi$(I=2) was calculated on an ensemble which is the same as that used in this work (there were periodic instead of G-parity boundary conditions, and the unitary pion mass was 170 MeV) and so should have the same lattice artefacts. This systematic error will be removed when the calculation has been performed with multiple lattice spacings and an $a \to 0$ extrapolation evaluated.

- $\overline{\text{MS}}$ Wilson coefficients. In this work, we calculated the Wilson coefficients to next-to-leading (NLO) order in perturbation theory [9] at 1.53 GeV, which is not much larger than the 500 MeV energy scale at which QCD is highly non-perturbative. We estimate this systematic error by comparing the difference in A_0 computed using leading order Wilson coefficients and the result from of NLO. This systematic error will be reduced if we do step scaling [39] in NPR and match the lattice weak operators to those in the $\overline{\text{MS}}$ scheme at a higher energy scale.

- Finite volume. The finite size of lattice has changed the loop integral in Feynman diagrams to discrete summation over the allowed momenta. This systematic error can be estimated using SU(3) finite-volume chiral perturbation theory (like the work in Ref [38]).

- Excited states contamination. A fitting range containing time separations that are too small will result in the excited states contamination. While it's typically chosen by examining the onset of a plateau in the effective mass plot, some excited state contamination may remain. We estimated the excited states contamination by doing

a 2-state fit on the two point correlation function, and compares the results with those from a 1-state fit. The comparison shows a systematic error of $\leq 5\%$, in the fitted, ground state amplitude.

There are other minor systematic issues like isospin breaking (light quark mass differences), the electromagnetic interaction, and the errors in the standard model physical parameters that we use as input in this work. But currently those are not major concerns compared to sources of errors discussed above or the current statistical error. The systematic errors are summarized in Table 7.1.

Description	Error
Operator renormalization	15%
$\overline{\text{MS}}$ Wilson coefficients	12%
LL factor	$\leq$11%
Finite lattice spacing	8%
Finite volume	7%
Excited states	$\leq$5%
Unphysical kinematics	$\leq$3%
Total	25%

Table 7.1: Systematic error budget for $\mathrm{Re}(A_0)$ and $\mathrm{Im}(A_0)$.

Although the error on our $\mathrm{Re}(\epsilon'/\epsilon)$ result is large compared to that from experiment, it is under control since we have seen the plateaus for the most important weak matrix elements Q_2 and Q_6, which contribute the major part of $\mathrm{Re}(A_0)$ and $\mathrm{Im}(A_0)$ respectively. We have shown that the CP-violation quantity $\mathrm{Re}(\epsilon'/\epsilon)$ is now accessible on lattice. With increasing statistics and possible improvements reducing the systematic errors discussed above, we can further improve the result for $\mathrm{Re}(\epsilon'/\epsilon)$, and allowing a more precise comparison of the standard model prediction with the result from experiment. The calculation of $\mathrm{Re}(\epsilon'/\epsilon)$, with 10% error relative to the present experimental value, can hopefully be carried out in 5 years, motivating more precise experimental measurement.

Bibliography

[1] T. Blum, P. Boyle, N. Christ, N. Garron, E. Goode, *et al.*, Phys.Rev.Lett. **108**, 141601 (2012), 1111.1699.

[2] C. Allton *et al.* (RBC, UKQCD), Phys.Rev. **D76**, 014504 (2007), hep-lat/0701013.

[3] G. Aad *et al.* (ATLAS), Phys.Lett. **B716**, 1 (2012), 1207.7214.

[4] C. Wu, E. Ambler, R. Hayward, D. Hoppes, and R. Hudson, Phys.Rev. **105**, 1413 (1957).

[5] J. Christenson, J. Cronin, V. Fitch, and R. Turlay, Phys.Rev.Lett. **13**, 138 (1964).

[6] J. Donoghue, E. Golowich, and B. R. Holstein, Camb.Monogr.Part.Phys.Nucl.Phys.Cosmol. **2**, 1 (1992).

[7] K. M. Watson, Phys.Rev. **88**, 1163 (1952).

[8] T. Blum, P. Boyle, N. Christ, J. Frison, N. Garron, *et al.*, Phys.Rev. **D91**(7), 074502 (2015), 1502.00263.

[9] G. Buchalla, A. J. Buras, and M. E. Lautenbacher, Rev.Mod.Phys. **68**, 1125 (1996), hep-ph/9512380.

[10] S. Duane, A. Kennedy, B. Pendleton, and D. Roweth, Phys.Lett. **B195**, 216 (1987).

[11] K. G. Wilson, Phys.Rev. **D10**, 2445 (1974).

[12] Y. Iwasaki and T. Yoshie, Phys.Lett. **B143**, 449 (1984).

[13] Y. Iwasaki, Nucl.Phys. **B258**, 141 (1985).

[14] D. B. Kaplan, Phys.Lett. **B288**, 342 (1992), hep-lat/9206013.

[15] T. Blum, P. Chen, N. H. Christ, C. Cristian, C. Dawson, *et al.*, Phys.Rev. **D69**, 074502 (2004), hep-lat/0007038.

[16] H. Rothe, World Sci.Lect.Notes Phys. **43**, 1 (1992).

[17] R. C. Brower, H. Neff, and K. Orginos (2012), 1206.5214.

[18] Q. Liu, *Kaon to two pions decays from lattice QCD: ΔI=1/2 rule and CP violation*, Ph.D. thesis, Columbia University (2012).

[19] L. Lellouch and M. Luscher, Commun.Math.Phys. **219**, 31 (2001), hep-lat/0003023.

[20] L. Maiani and M. Testa, Phys.Lett. **B245**, 585 (1990).

[21] M. Luscher, Nucl.Phys. **B354**, 531 (1991).

[22] C. D. Lin, G. Martinelli, C. T. Sachrajda, and M. Testa, Nucl.Phys. **B619**, 467 (2001), hep-lat/0104006.

[23] C. Lehner and C. Sturm, Phys.Rev. **D84**, 014001 (2011), 1104.4948.

[24] C. Sturm, Y. Aoki, N. Christ, T. Izubuchi, C. Sachrajda, *et al.*, Phys.Rev. **D80**, 014501 (2009), 0901.2599.

[25] R. Arthur *et al.* (RBC, UKQCD), Phys.Rev. **D87**, 094514 (2013), 1208.4412.

[26] K. Olive *et al.* (Particle Data Group), Chin.Phys. **C38**, 090001 (2014).

[27] A. Kennedy, I. Horvath, and S. Sint, Nucl.Phys.Proc.Suppl. **73**, 834 (1999), hep-lat/9809092.

[28] P. Boyle *et al.* (RBC, UKQCD), Phys.Rev.Lett. **110**(15), 152001 (2013), 1212.1474.

[29] D. Zhang, PoS **LATTICE2013**, 403 (2013).

[30] T. Kaneko *et al.* (JLQCD Collaboration), PoS **LATTICE2010**, 146 (2010), 1012.0137.

[31] J. Foley, K. Jimmy Juge, A. O'Cais, M. Peardon, S. M. Ryan, *et al.*, Comput.Phys.Commun. **172**, 145 (2005), hep-lat/0505023.

[32] M. Lightman, *ΔI=3/2 $K \to \pi\pi$ Decays Using lattice QCD with Domain Wall Fermions*, Ph.D. thesis, Columbia University (2011).

[33] T. Yamazaki *et al.* (CP-PACS), Phys.Rev. **D70**, 074513 (2004), hep-lat/0402025.

[34] D. Renfrew, T. Blum, N. Christ, R. Mawhinney, and P. Vranas, PoS **LATTICE2008**, 048 (2008), 0902.2587.

[35] P. A. Boyle, Comput.Phys.Commun. **180**, 2739 (2009).

[36] H. Yin, *Precision Lattice Calculation of Kaon Decays with Möbius Domain Wall Fermions*, Ph.D. thesis, Columbia University (2013).

[37] A. Schenk, Nucl.Phys. **B363**, 97 (1991).

[38] T. Blum, P. Boyle, N. Christ, N. Garron, E. Goode, *et al.*, Phys.Rev. **D86**, 074513 (2012), 1206.5142.

[39] R. Arthur and P. Boyle (RBC, UKQCD), Phys.Rev. **D83**, 114511 (2011), 1006.0422.

[40] Y. Aoki, P. Boyle, N. Christ, C. Dawson, M. Donnellan, *et al.*, Phys.Rev. **D78**, 054510 (2008), 0712.1061.

Appendix A

Physical Parameters

This appendix lists the input physical parameters that are used in this work, most are from PDG 2014 [26].

parameter	value
$\tau = \frac{V_{ts}^* V_{td}}{V_{ud} V_{us}^*}$	0.001543 - i * 0.000635
G_F	1.1663787e-5 GeV^{-2}
$\|V_{us}\|$	0.2253
$\|V_{ud}\|$	0.97425
α_e	1/128.0
$sin^2\theta_W$	0.23116
M_t	160.0 GeV
M_z	91.1876 GeV
M_w	80.385 GeV
m_b	4.18 GeV
m_c	1.275 GeV
$\alpha_s(M_z)$	0.1185
$\alpha_s^{3f}(1.52GeV)$	0.35355
$\omega = \mathrm{Re}A_2/\mathrm{Re}A_0$	0.04454(12)
$\|\epsilon\|$	$(2.228 \pm 0.011) \times 10^{-3}$
ϕ_ϵ	(43.52 ± 0.05) degree
$\mathrm{Re}(\epsilon'/\epsilon)$	$(1.66 \pm 0.23) \times 10^{-3}$

Table A.1: Fundamental physical constants used in this work

Meson Mass	
$M_{\pi^\pm}$	0.13957 GeV
M_{π^0}	0.13498 GeV
M_{K^+}	0.49368 GeV
$M_{K_S^0}$	0.49761 GeV
Meson Lifetime	
τ_{K^+}	1.238e-08 s
$\tau_{K_S^0}$	0.8954e-10 s
Branching Ratio	
$K^+ \to \pi^+\pi^0$	0.2066
$K_S^0 \to \pi^0\pi^0$	0.3069
$K_S^0 \to \pi^+\pi^-$	0.6920

Table A.2: Physical parameters for kaon decay.

i	$z_i^{\overline{\rm MS}}(\mu, 3f)$	$y_i^{\overline{\rm MS}}(\mu, 3f)$
1	-0.3735505346	0.0
2	1.189590707	0.0
3	0.001303738042	0.02720639673
4	-0.003723251215	-0.05827800254
5	0.002512132039	0.007125448671
6	-0.004745880306	-0.08193700481
7	6.09969058e-05	-0.0003401030763
8	-4.401008694e-05	0.0008687933744
9	3.568891181e-05	-0.01046394832
10	3.000903511e-05	0.003498092209

Table A.3: Wilson coefficients in the $\overline{\rm MS}$ scheme, at energy scale $\mu = 1.53$ GeV with 3-flavor QCD. These numbers were provided by Christoph Lehner.

Appendix B

$K \to \pi\pi$ Contractions

This appendix provides a summary of contractions which determine $\langle \pi\pi | H_W | K \rangle$ correlation function (see Chapter 3). Section B.1 contains the graphical representation of these contractions, categorized into four types. Section B.2 contains their formulas in terms of quark propagators.

B.1 Graphs

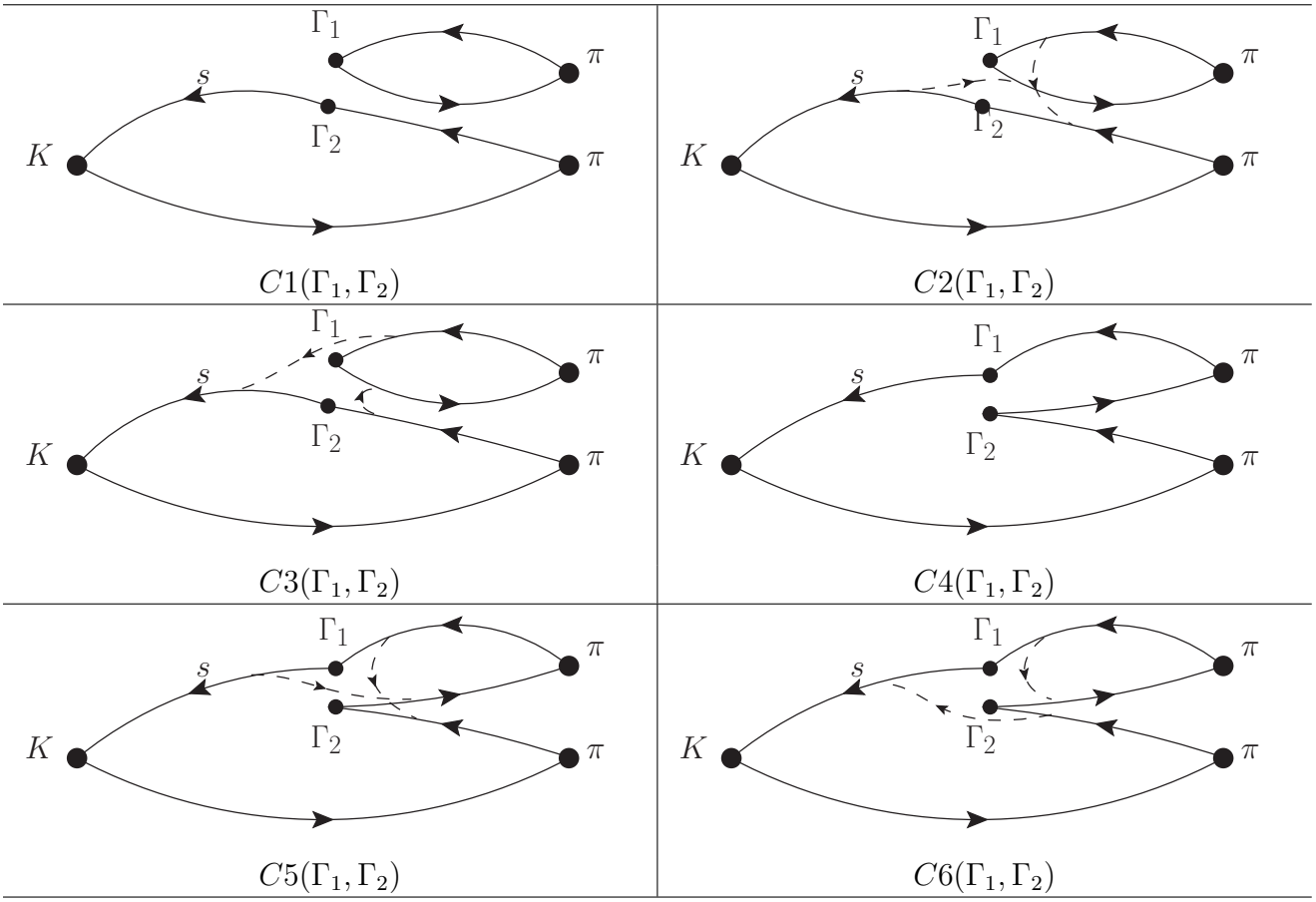

Figure B.1: Type1 Contractions. Lines with no label are light quark propagators, those with 's' are for the strange quark. When two quark lines are simply joined at a solid circle, both their spin, color, and flavor indices are contracted. Flavor index is from the use of two-component G-parity notation for the quark operator. If an added dashed line appears, it joins the lines whose color indices are contracted while the contraction of the solid lines indicates the joins of spin and flavor indices that are contracted.

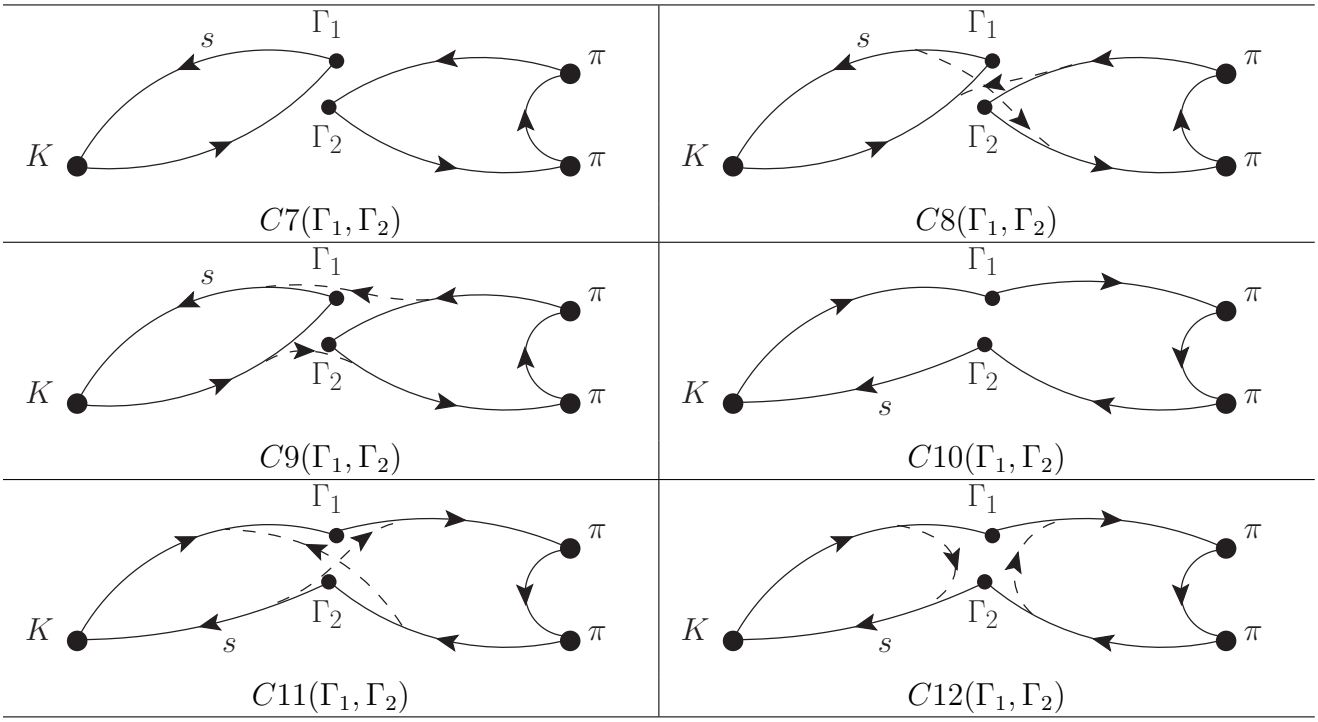

Figure B.2: Type2 Contractions. Lines with no label are light quark propagators, those with 's' are for the strange quark. When two quark lines are simply joined at a solid circle, both their spin, color, and flavor indices are contracted. Flavor index is from the use of two-component G-parity notation for the quark operator. If an added dashed line appears, it joins the lines whose color indices are contracted while the contraction of the solid lines indicates the joins of spin and flavor indices that are contracted.

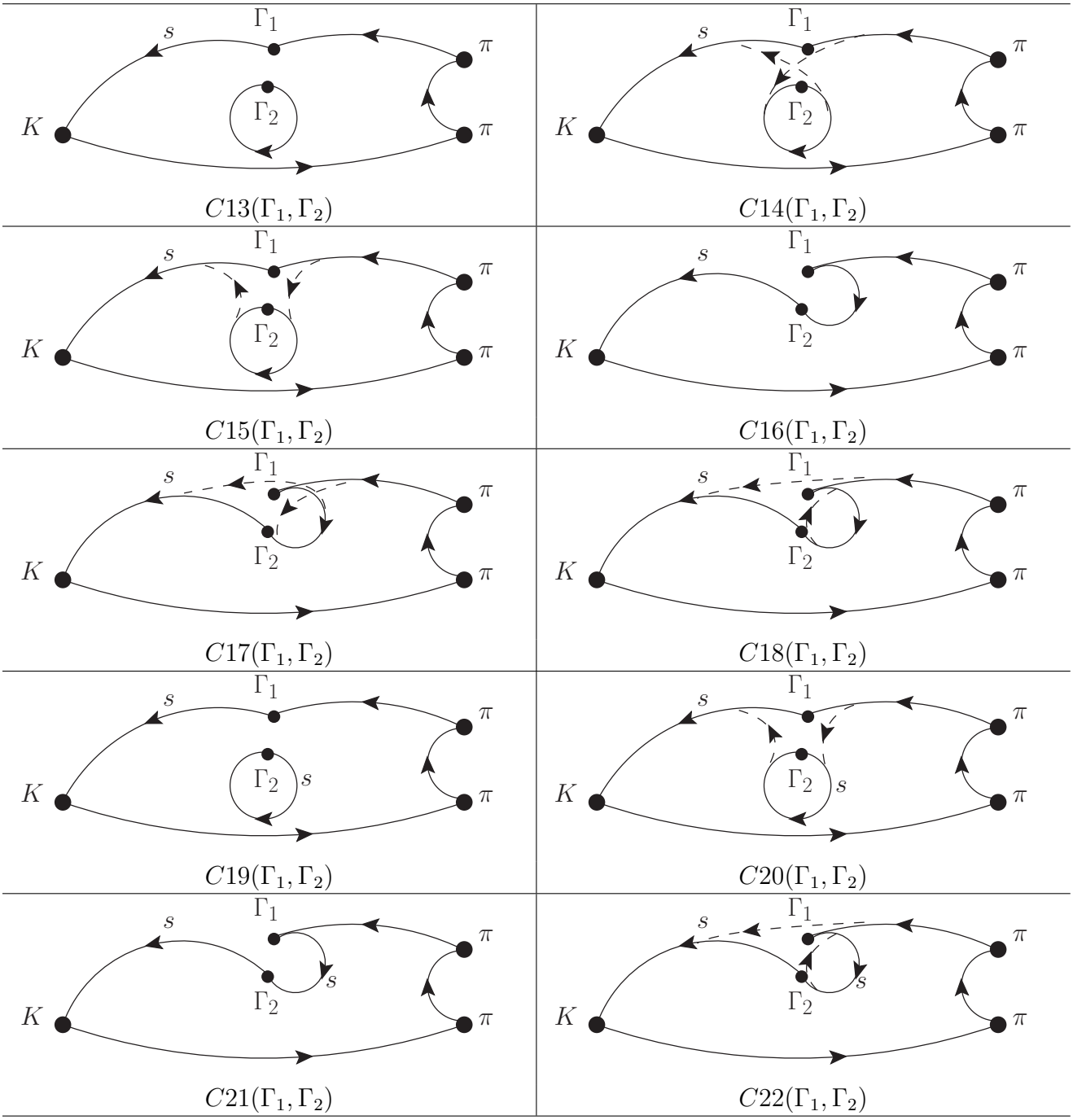

Figure B.3: Type3 Contractions. Lines with no label are light quark propagators, those with 's' are for the strange quark. When two quark lines are simply joined at a solid circle, both their spin, color, and flavor indices are contracted. Flavor index is from the use of two-component G-parity notation for the quark operator. If an added dashed line appears, it joins the lines whose color indices are contracted while the contraction of the solid lines indicates the joins of spin and flavor indices that are contracted.

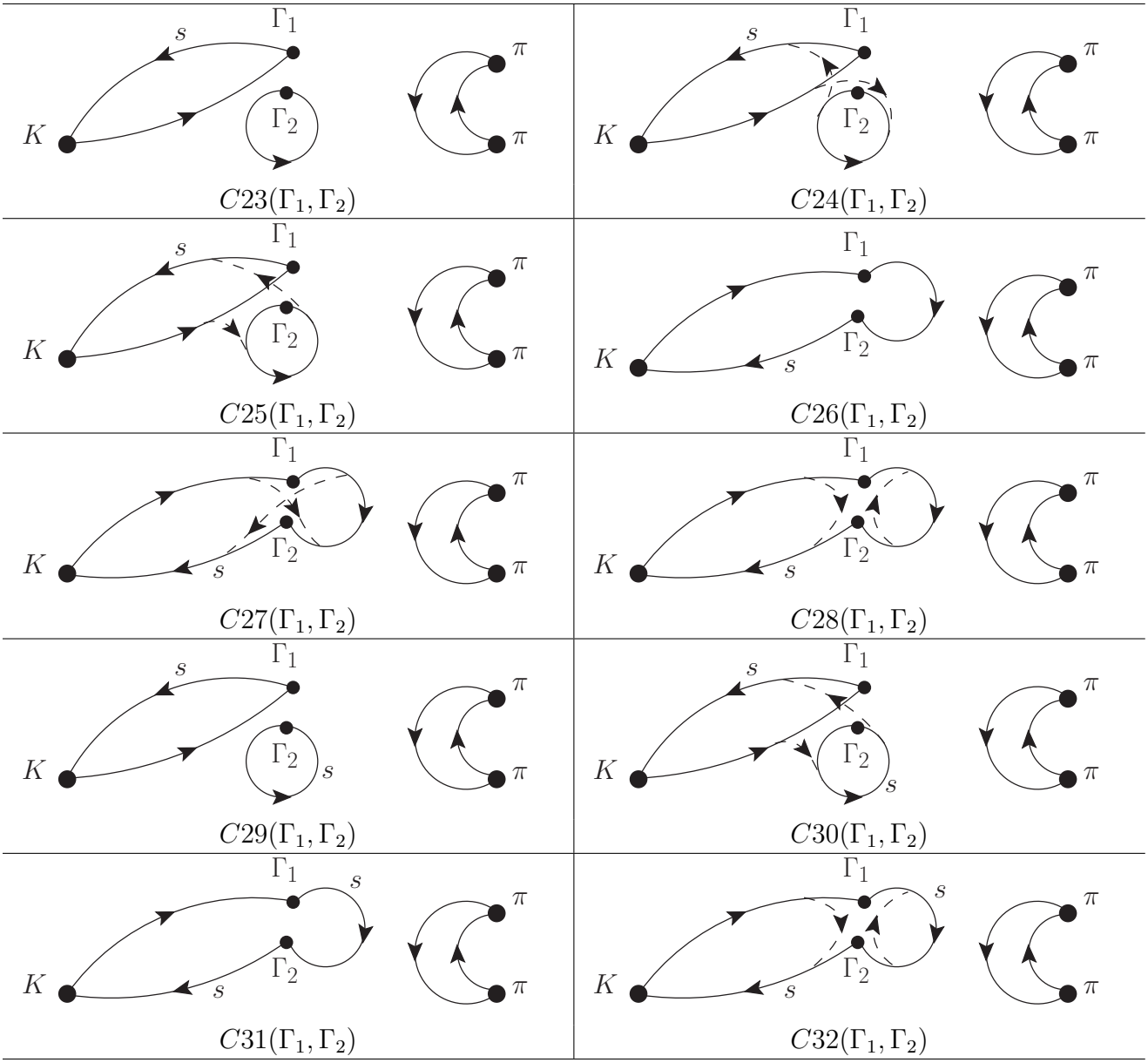

Figure B.4: Type4 Contractions. Lines with no label are light quark propagators, those with 's' are for the strange quark. When two quark lines are simply joined at a solid circle, both their spin, color, and flavor indices are contracted. Flavor index is from the use of two-component G-parity notation for the quark operator. If an added dashed line appears, it joins the lines whose color indices are contracted while the contraction of the solid lines indicates the joins of spin and flavor indices that are contracted.

B.2 Formulas

α, β are color indices, Tr_s stands for spin trace, Tr_c for color trace, Tr_f for G-parity flavor trace, Tr for spin-color-flavor trace, $\mathcal{G}^{(L)}$ is light quark propagator, $\mathcal{G}^{(H)}$ is strange quark propagator. For Type4 contractions, we only show the factor which multiplies the $\pi\pi$ bubble, the actual result is the product of the factor shown times the amplitude for the $\pi\pi$ bubble. This product is both multiplied and then averaged, and then the product of the averages is subtracted:

$$\langle C_i \cdot \frac{-1}{2} Tr\{\mathcal{G}^{(L)}_{x_{\pi_1},x_{\pi_2}} S_2 \mathcal{G}^{(L)}_{x_{\pi_2},x_{\pi_1}} S_2\}\rangle - \langle C_i\rangle \cdot \langle \frac{-1}{2} Tr\{\mathcal{G}^{(L)}_{x_{\pi_1},x_{\pi_2}} S_2 \mathcal{G}^{(L)}_{x_{\pi_2},x_{\pi_1}} S_2\}\rangle, \tag{B.1}$$

where $i = 23, 24, \ldots 32$.

Type1:

$$C1(\Gamma_1,\Gamma_2) = Tr\{\Gamma_1 \mathcal{G}^{(L)}_{x_{op},x_{\pi_2}} S_2 \mathcal{G}^{(L)}_{x_{\pi_2},x_{op}}\} \cdot Tr\{\Gamma_2 \mathcal{G}^{(L)}_{x_{op},x_{\pi_1}} S_2 \mathcal{G}^{(L)}_{x_{\pi_1},x_K} \gamma_5 \mathcal{G}^{(H)}_{x_K,x_{op}}\}$$

$$C2(\Gamma_1,\Gamma_2) = (Tr_{s,f}\{\Gamma_1 \mathcal{G}^{(L)}_{x_{op},x_{\pi_2}} S_2 \mathcal{G}^{(L)}_{x_{\pi_2},x_{op}}\})_{\alpha\beta} \cdot (Tr_{s,f}\{\Gamma_2 \mathcal{G}^{(L)}_{x_{op},x_{\pi_1}} S_2 \mathcal{G}^{(L)}_{x_{\pi_1},x_K} \gamma_5 \mathcal{G}^{(H)}_{x_K,x_{op}}\})_{\alpha\beta}$$

$$C3(\Gamma_1,\Gamma_2) = Tr_c\{Tr_{s,f}\{\Gamma_1 \mathcal{G}^{(L)}_{x_{op},x_{\pi_2}} S_2 \mathcal{G}^{(L)}_{x_{\pi_2},x_{op}}\} \cdot Tr_{s,f}\{\Gamma_2 \mathcal{G}^{(L)}_{x_{op},x_{\pi_1}} S_2 \mathcal{G}^{(L)}_{x_{\pi_1},x_K} \gamma_5 \mathcal{G}^{(H)}_{x_K,x_{op}}\}\}$$

$$C4(\Gamma_1,\Gamma_2) = Tr\{\Gamma_1 \mathcal{G}^{(L)}_{x_{op},x_{\pi_2}} S_2 \mathcal{G}^{(L)}_{x_{\pi_2},x_{op}} \cdot \Gamma_2 \mathcal{G}^{(L)}_{x_{op},x_{\pi_1}} S_2 \mathcal{G}^{(L)}_{x_{\pi_1},x_K} \gamma_5 \mathcal{G}^{(H)}_{x_K,x_{op}}\}$$

$$C5(\Gamma_1,\Gamma_2) = Tr_{s,f}\{(\Gamma_1 \mathcal{G}^{(L)}_{x_{op},x_{\pi_2}} S_2 \mathcal{G}^{(L)}_{x_{\pi_2},x_{op}})_{\alpha\beta} \cdot (\Gamma_2 \mathcal{G}^{(L)}_{x_{op},x_{\pi_1}} S_2 \mathcal{G}^{(L)}_{x_{\pi_1},x_K} \gamma_5 \mathcal{G}^{(H)}_{x_K,x_{op}})_{\alpha\beta}\}$$

$$C6(\Gamma_1,\Gamma_2) = Tr_{s,f}\{Tr_c\{\Gamma_1 \mathcal{G}^{(L)}_{x_{op},x_{\pi_2}} S_2 \mathcal{G}^{(L)}_{x_{\pi_2},x_{op}}\} \cdot Tr_c\{\Gamma_2 \mathcal{G}^{(L)}_{x_{op},x_{\pi_1}} S_2 \mathcal{G}^{(L)}_{x_{\pi_1},x_K} \gamma_5 \mathcal{G}^{(H)}_{x_K,x_{op}}\}\}$$

Type 2:

$$C7(\Gamma_1,\Gamma_2) = Tr\{\Gamma_1\mathcal{G}^{(L)}_{x_{op},x_K}\gamma_5\mathcal{G}^{(H)}_{x_K,x_{op}}\}\cdot Tr\{\Gamma_2\mathcal{G}^{(L)}_{x_{op},x_{\pi_1}}S_2\mathcal{G}^{(L)}_{x_{\pi_1},x_{\pi_2}}S_2\mathcal{G}^{(L)}_{x_{\pi_2},x_{op}}\}$$

$$C8(\Gamma_1,\Gamma_2) = (Tr_{s,f}\{\Gamma_1\mathcal{G}^{(L)}_{x_{op},x_K}\gamma_5\mathcal{G}^{(H)}_{x_K,x_{op}}\})_{\alpha\beta}\cdot(Tr_{s,f}\{\Gamma_2\mathcal{G}^{(L)}_{x_{op},x_{\pi_1}}S_2\mathcal{G}^{(L)}_{x_{\pi_1},x_{\pi_2}}S_2\mathcal{G}^{(L)}_{x_{\pi_2},x_{op}}\})_{\alpha\beta}$$

$$C9(\Gamma_1,\Gamma_2) = Tr_c\{Tr_{s,f}\{\Gamma_1\mathcal{G}^{(L)}_{x_{op},x_K}\gamma_5\mathcal{G}^{(H)}_{x_K,x_{op}}\}\cdot Tr_{s,f}\{\Gamma_2\mathcal{G}^{(L)}_{x_{op},x_{\pi_1}}S_2\mathcal{G}^{(L)}_{x_{\pi_1},x_{\pi_2}}S_2\mathcal{G}^{(L)}_{x_{\pi_2},x_{op}}\}\}$$

$$C10(\Gamma_1,\Gamma_2) = Tr\{\Gamma_1\mathcal{G}^{(L)}_{x_{op},x_K}\gamma_5\mathcal{G}^{(H)}_{x_K,x_{op}}\cdot\Gamma_2\mathcal{G}^{(L)}_{x_{op},x_{\pi_1}}S_2\mathcal{G}^{(L)}_{x_{\pi_1},x_{\pi_2}}S_2\mathcal{G}^{(L)}_{x_{\pi_2},x_{op}}\}$$

$$C11(\Gamma_1,\Gamma_2) = Tr_{s,f}\{(\Gamma_1\mathcal{G}^{(L)}_{x_{op},x_K}\gamma_5\mathcal{G}^{(H)}_{x_K,x_{op}})_{\alpha\beta}\cdot(\Gamma_2\mathcal{G}^{(L)}_{x_{op},x_{\pi_1}}S_2\mathcal{G}^{(L)}_{x_{\pi_1},x_{\pi_2}}S_2\mathcal{G}^{(L)}_{x_{\pi_2},x_{op}})_{\alpha\beta}\}$$

$$C12(\Gamma_1,\Gamma_2) = Tr_{s,f}\{Tr_c\{\Gamma_1\mathcal{G}^{(L)}_{x_{op},x_K}\gamma_5\mathcal{G}^{(H)}_{x_K,x_{op}}\}\cdot Tr_c\{\Gamma_2\mathcal{G}^{(L)}_{x_{op},x_{\pi_1}}S_2\mathcal{G}^{(L)}_{x_{\pi_1},x_{\pi_2}}S_2\mathcal{G}^{(L)}_{x_{\pi_2},x_{op}}\}\}$$

Type 3:

$$C13(\Gamma_1,\Gamma_2) = Tr\{\Gamma_1\mathcal{G}^{(L)}_{x_{op},x_{\pi_1}}S_2\mathcal{G}^{(L)}_{x_{\pi_1},x_{\pi_2}}S_2\mathcal{G}^{(L)}_{x_{\pi_2},x_K}\gamma_5\mathcal{G}^{(H)}_{x_K,x_{op}}\}\cdot Tr\{\Gamma_2\mathcal{G}^{(L)}_{x_{op},x_{op}}\}$$

$$C14(\Gamma_1,\Gamma_2) = (Tr_{s,f}\{\Gamma_1\mathcal{G}^{(L)}_{x_{op},x_{\pi_1}}S_2\mathcal{G}^{(L)}_{x_{\pi_1},x_{\pi_2}}S_2\mathcal{G}^{(L)}_{x_{\pi_2},x_K}\gamma_5\mathcal{G}^{(H)}_{x_K,x_{op}}\})_{\alpha\beta}\cdot(Tr_{s,f}\{\Gamma_2\mathcal{G}^{(L)}_{x_{op},x_{op}}\})_{\alpha\beta}$$

$$C15(\Gamma_1,\Gamma_2) = Tr_c\{Tr_{s,f}\{\Gamma_1\mathcal{G}^{(L)}_{x_{op},x_{\pi_1}}S_2\mathcal{G}^{(L)}_{x_{\pi_1},x_{\pi_2}}S_2\mathcal{G}^{(L)}_{x_{\pi_2},x_K}\gamma_5\mathcal{G}^{(H)}_{x_K,x_{op}}\}\cdot Tr_{s,f}\{\Gamma_2\mathcal{G}^{(L)}_{x_{op},x_{op}}\}\}$$

$$C16(\Gamma_1,\Gamma_2) = Tr\{\Gamma_1\mathcal{G}^{(L)}_{x_{op},x_{\pi_1}}S_2\mathcal{G}^{(L)}_{x_{\pi_1},x_{\pi_2}}S_2\mathcal{G}^{(L)}_{x_{\pi_2},x_K}\gamma_5\mathcal{G}^{(H)}_{x_K,x_{op}}\cdot\Gamma_2\mathcal{G}^{(L)}_{x_{op},x_{op}}\}$$

$$C17(\Gamma_1,\Gamma_2) = Tr_{s,f}\{(\Gamma_1\mathcal{G}^{(L)}_{x_{op},x_{\pi_1}}S_2\mathcal{G}^{(L)}_{x_{\pi_1},x_{\pi_2}}S_2\mathcal{G}^{(L)}_{x_{\pi_2},x_K}\gamma_5\mathcal{G}^{(H)}_{x_K,x_{op}})_{\alpha\beta}\cdot(\Gamma_2\mathcal{G}^{(L)}_{x_{op},x_{op}})_{\alpha\beta}\}$$

$$C18(\Gamma_1,\Gamma_2) = Tr_{s,f}\{Tr_c\{\Gamma_1\mathcal{G}^{(L)}_{x_{op},x_{\pi_1}}S_2\mathcal{G}^{(L)}_{x_{\pi_1},x_{\pi_2}}S_2\mathcal{G}^{(L)}_{x_{\pi_2},x_K}\gamma_5\mathcal{G}^{(H)}_{x_K,x_{op}}\}\cdot Tr_c\{\Gamma_2\mathcal{G}^{(L)}_{x_{op},x_{op}}\}\}$$

$$C19(\Gamma_1,\Gamma_2) = Tr\{\Gamma_1\mathcal{G}^{(L)}_{x_{op},x_{\pi_1}}S_2\mathcal{G}^{(L)}_{x_{\pi_1},x_{\pi_2}}S_2\mathcal{G}^{(L)}_{x_{\pi_2},x_K}\gamma_5\mathcal{G}^{(H)}_{x_K,x_{op}}\}\cdot Tr\{\Gamma_2\mathcal{G}^{(H)}_{x_{op},x_{op}}\}$$

$$C20(\Gamma_1,\Gamma_2) = Tr_c\{Tr_{s,f}\{\Gamma_1\mathcal{G}^{(L)}_{x_{op},x_{\pi_1}}S_2\mathcal{G}^{(L)}_{x_{\pi_1},x_{\pi_2}}S_2\mathcal{G}^{(L)}_{x_{\pi_2},x_K}\gamma_5\mathcal{G}^{(H)}_{x_K,x_{op}}\}\cdot Tr_{s,f}\{\Gamma_2\mathcal{G}^{(H)}_{x_{op},x_{op}}\}\}$$

$$C21(\Gamma_1,\Gamma_2) = Tr\{\Gamma_1\mathcal{G}^{(L)}_{x_{op},x_{\pi_1}}S_2\mathcal{G}^{(L)}_{x_{\pi_1},x_{\pi_2}}S_2\mathcal{G}^{(L)}_{x_{\pi_2},x_K}\gamma_5\mathcal{G}^{(H)}_{x_K,x_{op}}\cdot\Gamma_2\mathcal{G}^{(H)}_{x_{op},x_{op}}\}$$

$$C22(\Gamma_1,\Gamma_2) = Tr_{s,f}\{Tr_c\{\Gamma_1\mathcal{G}^{(L)}_{x_{op},x_{\pi_1}}S_2\mathcal{G}^{(L)}_{x_{\pi_1},x_{\pi_2}}S_2\mathcal{G}^{(L)}_{x_{\pi_2},x_K}\gamma_5\mathcal{G}^{(H)}_{x_K,x_{op}}\}\cdot Tr_c\{\Gamma_2\mathcal{G}^{(H)}_{x_{op},x_{op}}\}\}$$

Type 4: ($\pi\pi$ bubble is not included for simplicity)

$$C23(\Gamma_1,\Gamma_2) = Tr\{\Gamma_1 \mathcal{G}^{(L)}_{x_{op},x_K}\gamma_5\mathcal{G}^{(H)}_{x_K,x_{op}}\}\cdot Tr\{\Gamma_2\mathcal{G}^{(L)}_{x_{op},x_{op}}\}$$

$$C24(\Gamma_1,\Gamma_2) = (Tr_{s,f}\{\Gamma_1 \mathcal{G}^{(L)}_{x_{op},x_K}\gamma_5\mathcal{G}^{(H)}_{x_K,x_{op}}\})_{\alpha\beta}\cdot (Tr_{s,f}\{\Gamma_2\mathcal{G}^{(L)}_{x_{op},x_{op}}\})_{\alpha\beta}$$

$$C25(\Gamma_1,\Gamma_2) = Tr_c\{Tr_{s,f}\{\Gamma_1 \mathcal{G}^{(L)}_{x_{op},x_K}\gamma_5\mathcal{G}^{(H)}_{x_K,x_{op}}\}\cdot Tr_{s,f}\{\Gamma_2\mathcal{G}^{(L)}_{x_{op},x_{op}}\}\}$$

$$C26(\Gamma_1,\Gamma_2) = Tr\{\Gamma_1 \mathcal{G}^{(L)}_{x_{op},x_K}\gamma_5\mathcal{G}^{(H)}_{x_K,x_{op}}\cdot\Gamma_2\mathcal{G}^{(L)}_{x_{op},x_{op}}\}$$

$$C27(\Gamma_1,\Gamma_2) = Tr_{s,f}\{(\Gamma_1 \mathcal{G}^{(L)}_{x_{op},x_K}\gamma_5\mathcal{G}^{(H)}_{x_K,x_{op}})_{\alpha\beta}\cdot(\Gamma_2\mathcal{G}^{(L)}_{x_{op},x_{op}})_{\alpha\beta}\}$$

$$C28(\Gamma_1,\Gamma_2) = Tr_{s,f}\{Tr_c\{\Gamma_1 \mathcal{G}^{(L)}_{x_{op},x_K}\gamma_5\mathcal{G}^{(H)}_{x_K,x_{op}}\}\cdot Tr_c\{\Gamma_2\mathcal{G}^{(L)}_{x_{op},x_{op}}\}\}$$

$$C29(\Gamma_1,\Gamma_2) = Tr\{\Gamma_1 \mathcal{G}^{(L)}_{x_{op},x_K}\gamma_5\mathcal{G}^{(H)}_{x_K,x_{op}}\}\cdot Tr\{\Gamma_2\mathcal{G}^{(H)}_{x_{op},x_{op}}\}$$

$$C30(\Gamma_1,\Gamma_2) = Tr_c\{Tr_{s,f}\{\Gamma_1 \mathcal{G}^{(L)}_{x_{op},x_K}\gamma_5\mathcal{G}^{(H)}_{x_K,x_{op}}\}\cdot Tr_{s,f}\{\Gamma_2\mathcal{G}^{(H)}_{x_{op},x_{op}}\}\}$$

$$C31(\Gamma_1,\Gamma_2) = Tr\{\Gamma_1 \mathcal{G}^{(L)}_{x_{op},x_K}\gamma_5\mathcal{G}^{(H)}_{x_K,x_{op}}\cdot\Gamma_2\mathcal{G}^{(H)}_{x_{op},x_{op}}\}$$

$$C32(\Gamma_1,\Gamma_2) = Tr_{s,f}\{Tr_c\{\Gamma_1 \mathcal{G}^{(L)}_{x_{op},x_K}\gamma_5\mathcal{G}^{(H)}_{x_K,x_{op}}\}\cdot Tr_c\{\Gamma_2\mathcal{G}^{(H)}_{x_{op},x_{op}}\}\}$$

Appendix C

NPR Results

This appendix provide more details about the NPR method and results (the NPR procedure is explained in Chapter 3). The NPR Green functions are measured on 100 configurations from the 2+1 flavor, 32nt64 ensemble, generated with the IDSDR gauge action at $\beta = 1.75$ [1]. The two external momenta are chosen to be (in lattice units):

$$p_1 = (0, 4, 4, 0) \cdot \frac{2\pi}{L} \tag{C.1}$$

$$p_2 = (4, 4, 0, 0) \cdot \frac{2\pi}{L} \tag{C.2}$$

They are the non-exceptional momenta ($|p_1| = |p_2| = |p_1 - p_2|$) [40] which suppresses chiral symmetry breaking and other unwanted infrared effects [24].

	1	2	3	4	5	6	7
				mean:			
1	8.1023e-01	6.6711e-05	-6.9404e-06	-1.2170e-05	-1.5590e-05	-6.9866e-03	2.5370e-03
2	-2.6604e-06	8.7110e-01	-1.3819e-01	-3.3180e-03	-2.5172e-02	1.7819e-03	3.5264e-03
3	8.1198e-07	-7.0452e-02	9.1508e-01	2.3405e-04	7.1408e-04	-1.8952e-04	-1.9284e-03
4	-1.0388e-05	-3.5369e-02	-6.5780e-02	9.1090e-01	-2.0520e-01	7.8975e-03	9.8800e-03
5	7.5255e-06	-9.4921e-02	-8.3660e-02	-5.7388e-02	6.0669e-01	-8.0282e-03	8.6522e-04
6	-8.5468e-04	-1.1743e-02	3.5239e-03	7.5779e-04	-3.3919e-04	9.3368e-01	-1.7509e-01
7	-1.1844e-04	-8.5939e-03	1.0275e-02	-3.1196e-03	-8.2487e-03	-4.8744e-02	5.7921e-01
				error bar:			
1	9.0443e-05	7.7694e-05	8.3875e-05	3.7178e-05	3.0457e-05	6.4797e-05	2.6668e-05
2	6.7190e-06	6.4168e-02	5.4812e-02	2.7493e-02	1.9848e-02	8.2135e-03	6.5331e-03
3	4.0439e-06	3.1415e-02	3.1385e-02	1.2315e-02	9.6453e-03	4.6913e-03	3.2188e-03
4	2.0855e-05	2.0532e-01	1.6629e-01	8.6342e-02	6.0777e-02	2.4958e-02	1.9637e-02
5	1.3680e-05	9.1173e-02	9.6152e-02	4.0341e-02	3.2781e-02	1.5488e-02	1.2961e-02
6	7.8608e-06	1.1327e-02	1.2334e-02	4.9407e-03	4.2247e-03	3.2009e-03	2.5145e-03
7	8.1857e-06	1.8469e-02	2.2221e-02	7.0151e-03	7.0474e-03	3.5861e-03	4.3356e-03
				mean:			
1	8.1023e-01	-1.6216e-13	-1.6971e-13	1.7344e-14	-1.8381e-14	-9.3623e-17	-1.9604e-16
2	1.8495e-15	8.7272e-01	-1.3910e-01	-4.1293e-03	3.3385e-03	-4.4808e-17	1.4794e-17
3	-2.5090e-15	-7.5215e-02	9.3011e-01	-1.5559e-02	1.0626e-02	6.0257e-17	-1.8915e-17
4	6.3990e-17	-1.3545e-01	-1.1509e-01	8.9777e-01	-1.1157e-01	-9.7144e-18	-4.1633e-18
5	-4.2942e-17	-9.5667e-02	-4.7312e-02	-6.6366e-02	5.9777e-01	-1.8873e-17	1.2212e-17
6	4.1538e-19	4.5986e-19	9.7276e-18	-2.6747e-17	1.2940e-17	9.3431e-01	-1.7399e-01
7	-6.0652e-21	8.3007e-19	-3.2236e-18	6.1237e-19	2.2050e-18	-5.0636e-02	5.7787e-01
				error bar:			
1	9.0469e-05	1.1453e-13	1.4096e-13	4.9721e-14	3.2769e-14	6.5362e-16	3.7635e-16
2	1.5171e-15	6.2415e-02	5.7460e-02	2.5594e-02	1.5432e-02	1.3644e-16	9.8427e-17
3	2.0649e-15	2.9945e-02	3.1336e-02	1.0995e-02	8.6316e-03	1.5065e-16	1.2185e-16
4	2.7458e-16	1.8444e-01	1.6978e-01	7.8658e-02	4.5914e-02	2.8329e-15	1.3688e-15
5	1.6914e-16	7.9738e-02	8.1133e-02	3.6841e-02	2.3750e-02	1.6031e-15	1.9568e-15
6	8.1108e-17	2.7216e-16	3.7579e-16	1.7739e-15	7.1163e-16	1.0260e-04	4.5991e-05
7	5.2903e-17	1.4463e-16	2.3428e-16	8.1772e-16	2.9751e-16	4.1504e-05	1.2445e-04

Table C.1: NPR matrix $Z^{Lat\to RI}/Z_q^2$ with γ_μ projectors, at 1.53 GeV, measured on 100 configurations from the 32nt64 ensemble (no Gparity) [1] with $a^{-1} = 1.364$GeV. External momenta are $p_1 = (0,4,4,0)\cdot 2\pi/L, p_2 = (4,4,0,0)\cdot 2\pi/L$ and valence quark masses are $m_{l/s} = 0.01$. The dim-3 and dim-4 operators which mix with the lattice operators have been subtracted. The upper half shows results from the parity even part of each operator, while the lower half shows the results from the parity odd part.

	1	2	3	4	5	6	7
				mean:			
1	7.2768e-01	0.0000e+00	0.0000e+00	0.0000e+00	0.0000e+00	0.0000e+00	0.0000e+00
2	0.0000e+00	4.8376e-01	-4.7810e-01	-5.5167e-03	-3.6937e-03	0.0000e+00	0.0000e+00
3	0.0000e+00	2.1709e-01	1.3258e+00	4.9468e-03	-4.2714e-03	0.0000e+00	0.0000e+00
4	0.0000e+00	-1.3495e-01	-1.4757e-01	7.4442e-01	-1.7073e-01	0.0000e+00	0.0000e+00
5	0.0000e+00	-5.7964e-02	7.2590e-02	-4.8371e-02	5.7642e-01	0.0000e+00	0.0000e+00
6	0.0000e+00	0.0000e+00	0.0000e+00	0.0000e+00	0.0000e+00	7.8077e-01	-1.4432e-01
7	0.0000e+00	0.0000e+00	0.0000e+00	0.0000e+00	0.0000e+00	-9.6648e-02	5.7696e-01
				error bar:			
1	1.2800e-04	0.0000e+00	0.0000e+00	0.0000e+00	0.0000e+00	0.0000e+00	0.0000e+00
2	0.0000e+00	4.8667e-02	5.8977e-02	2.1115e-02	1.4009e-02	0.0000e+00	0.0000e+00
3	0.0000e+00	8.2487e-02	9.5552e-02	3.3641e-02	2.4977e-02	0.0000e+00	0.0000e+00
4	0.0000e+00	2.5929e-01	2.8255e-01	9.1546e-02	5.9709e-02	0.0000e+00	0.0000e+00
5	0.0000e+00	1.5195e-01	2.1581e-01	5.9684e-02	3.9953e-02	0.0000e+00	0.0000e+00
6	0.0000e+00	0.0000e+00	0.0000e+00	0.0000e+00	0.0000e+00	6.0732e-03	4.2876e-03
7	0.0000e+00	0.0000e+00	0.0000e+00	0.0000e+00	0.0000e+00	9.7883e-03	7.1652e-03
				mean:			
1	7.2768e-01	0.0000e+00	0.0000e+00	0.0000e+00	0.0000e+00	0.0000e+00	0.0000e+00
2	0.0000e+00	4.6486e-01	-4.9705e-01	-1.9463e-02	9.1893e-03	0.0000e+00	0.0000e+00
3	0.0000e+00	2.1729e-01	1.3259e+00	-8.0524e-03	9.5229e-03	0.0000e+00	0.0000e+00
4	0.0000e+00	-2.5362e-01	-2.5451e-01	6.9755e-01	-1.1228e-01	0.0000e+00	0.0000e+00
5	0.0000e+00	5.3154e-02	1.6763e-01	-5.6372e-02	5.4883e-01	0.0000e+00	0.0000e+00
6	0.0000e+00	0.0000e+00	0.0000e+00	0.0000e+00	0.0000e+00	7.8179e-01	-1.4633e-01
7	0.0000e+00	0.0000e+00	0.0000e+00	0.0000e+00	0.0000e+00	-9.4179e-02	5.9137e-01
				error bar:			
1	1.2795e-04	0.0000e+00	0.0000e+00	0.0000e+00	0.0000e+00	0.0000e+00	0.0000e+00
2	0.0000e+00	4.7599e-02	5.5433e-02	1.7838e-02	1.1336e-02	0.0000e+00	0.0000e+00
3	0.0000e+00	7.6323e-02	9.1038e-02	3.3251e-02	2.2141e-02	0.0000e+00	0.0000e+00
4	0.0000e+00	2.1240e-01	2.2747e-01	7.7165e-02	4.5480e-02	0.0000e+00	0.0000e+00
5	0.0000e+00	1.2478e-01	1.5937e-01	5.8291e-02	3.7986e-02	0.0000e+00	0.0000e+00
6	0.0000e+00	0.0000e+00	0.0000e+00	0.0000e+00	0.0000e+00	1.7862e-04	5.7718e-05
7	0.0000e+00	0.0000e+00	0.0000e+00	0.0000e+00	0.0000e+00	8.2486e-05	1.3845e-04

Table C.2: NPR matrix $Z^{Lat\to RI}/Z_q^2$ with $\not{q}$ projectors, at 1.53 GeV, measured on 100 configurations from the 32nt64 ensemble (no Gparity) [1] with $a^{-1} = 1.364$GeV. External momenta are $p_1 = (0, 4, 4, 0) \cdot 2\pi/L, p_2 = (4, 4, 0, 0) \cdot 2\pi/L$ and valence quark masses are $m_{l/s} = 0.01$. The dim-3 and dim-4 operators which mix with the lattice operators have been subtracted. The upper half shows results from the parity even part of each operator, while the lower half shows the results from the parity odd part.

	γ_μ scheme	$\not{q}$ scheme
Z_q	0.723713 ± 0.000034	0.793584 ± 0.000084

Table C.3: $Z_q = \frac{\Lambda_V Z_V + \Lambda_A Z_A}{2}$ in both γ_μ and $\not{q}$ scheme, measured on 100 configurations from the 32nt64 ensemble (no Gparity) [1] with $a^{-1} = 1.364$GeV. The external momenta are $p_1 = (0, 4, 4, 0) \cdot 2\pi/L, p_2 = (4, 4, 0, 0) \cdot 2\pi/L$, and valence quark masses are $m_{l/s} = 0.01$.

	(γ_μ, γ_μ)	$(\gamma_\mu, \not{q})$	$(\not{q}, \gamma_\mu)$	$(\not{q}, \not{q})$
1	-2.318e-01 ± 7.113e-03	-2.570e-01 ± 7.892e-03	-2.938e-01 ± 2.050e-02	-3.219e-01 ± 2.242e-02
2	5.802e-01 ± 7.111e-03	6.446e-01 ± 7.888e-03	6.242e-01 ± 2.050e-02	6.911e-01 ± 2.242e-02
3	5.399e-03 ± 7.302e-03	5.813e-03 ± 8.104e-03	8.553e-02 ± 1.585e-02	9.114e-02 ± 1.734e-02
5	-5.796e-03 ± 6.783e-03	-6.295e-03 ± 7.530e-03	4.270e-03 ± 1.554e-02	5.142e-03 ± 1.692e-02
6	1.567e-03 ± 5.616e-03	1.499e-03 ± 6.233e-03	-2.064e-03 ± 1.145e-02	-2.712e-03 ± 1.252e-02
7	3.186e-05 ± 2.051e-09	3.553e-05 ± 6.111e-09	2.931e-05 ± 4.734e-09	3.282e-05 ± 3.058e-09
8	-2.031e-05 ± 2.579e-09	-2.276e-05 ± 5.111e-09	-1.988e-05 ± 3.326e-09	-2.229e-05 ± 5.124e-09

Table C.4: Real part of the lattice Wilson coefficients C_i^{Lat}, using the 4 different RI intermediate schemes, and perturbatively matched at 1.53 GeV. The NPR matrix is measured on 100 configurations from the 32nt64 ensemble [1].

	(γ_μ, γ_μ)	$(\gamma_\mu, \not{q})$	$(\not{q}, \gamma_\mu)$	$(\not{q}, \not{q})$
1	-1.259e-05 ± 1.182e-06	-1.387e-05 ± 1.316e-06	-1.663e-05 ± 2.425e-06	-1.820e-05 ± 2.685e-06
2	1.542e-05 ± 1.182e-06	1.702e-05 ± 1.316e-06	1.931e-05 ± 2.425e-06	2.121e-05 ± 2.685e-06
3	5.830e-06 ± 1.020e-06	6.413e-06 ± 1.135e-06	9.567e-06 ± 2.096e-06	1.045e-05 ± 2.321e-06
5	-5.055e-06 ± 1.251e-06	-5.687e-06 ± 1.391e-06	-3.609e-06 ± 2.293e-06	-4.019e-06 ± 2.539e-06
6	1.781e-05 ± 8.405e-07	1.991e-05 ± 9.357e-07	1.617e-05 ± 1.414e-06	1.806e-05 ± 1.567e-06
7	1.346e-07 ± 1.613e-11	1.510e-07 ± 3.085e-11	1.295e-07 ± 2.612e-11	1.453e-07 ± 3.462e-11
8	-2.103e-07 ± 3.935e-11	-2.361e-07 ± 6.439e-11	-2.097e-07 ± 4.496e-11	-2.352e-07 ± 6.966e-11

Table C.5: Imaginary part of the lattice Wilson coefficients C_i^{Lat}, using the 4 different RI intermediate schemes, and perturbatively matched at 1.53 GeV. The NPR matrix is measured on 100 configurations from the 32nt64 ensemble [1].

	$(\gamma_\mu, \gamma_\mu) - (\not{q}, \not{q})$	
	real part	imag part
1	9.008e-02 ± 2.151e-02	5.612e-06 ± 2.523e-06
2	-1.109e-01 ± 2.150e-02	-5.782e-06 ± 2.523e-06
3	-8.574e-02 ± 1.682e-02	-4.617e-06 ± 2.100e-06
5	-1.094e-02 ± 1.588e-02	-1.036e-06 ± 2.205e-06
6	4.279e-03 ± 1.163e-02	-2.556e-07 ± 1.444e-06
7	-9.661e-07 ± 2.596e-09	-1.072e-08 ± 2.970e-11
8	1.981e-06 ± 3.745e-09	2.489e-08 ± 4.679e-11

Table C.6: Jackknifed difference of the lattice Wilson coefficients C_i^{Lat}, using the (γ_μ, γ_μ) and $(\not{q}, \not{q})$ RI intermediate schemes, and perturbatively matched at 1.53 GeV. The NPR matrix is measured on 100 configurations from the 32nt64 ensemble [1].

Appendix D

All-to-all Propagators Compared to Wall Source Propagators

The gauge ensemble used in the comparison is the 16nt32 ensemble as in Ref [2], with the dynamic strange quark mass changed from 0.04 to 0.032. In order to compare these two methods on the same footing, we measured on 200 configurations in both cases. The valence quark masses are chosen as $m_{u/d} = 0.01$ and $m_s = 0.066$, which gives the pion mass $m_\pi \approx 422$MeV and kaon mass $m_K \approx 738$MeV. Boundary conditions are all periodic.

The light quark all-to-all propagators contains 100 low modes. For high mode part we use 1 random hit on each lattice site with time-spin-color dilution. For the strange quark all-to-all propagators, we use the same setup for high mode part as that in the light quark all-to-all propagators, but no low modes are used. Coulomb gauge fixing on each time slice is used to construct gauge invariant pion interpolating operators. The Lanczos algorithm uses the parameters $\alpha = 5.5, \beta = 0.5$ and Chebyshev order $n = 100$. The meson field wave function used for both the kaon and pion is a hydrogen wave function as in Equation 4.38 with radius 2. (More information about meson source used with the all-to-all propagators is given in Chapter 4.)

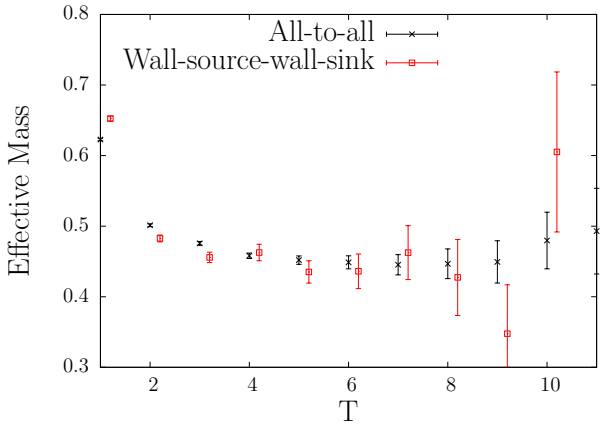

Figure D.1: $\pi\pi$(I=0) effective energy

	$E_{\pi\pi}^{I=0}$
All-to-all	0.449(10)
Wall-source-wall-sink	0.438(25)

Table D.1: $E_{\pi\pi(I=0)}$ energy in lattice unit,

	Wall-source-wall-sink		All-to-all(200 conf)	
i	$Re(A_0)$	$Im(A_0)$	$Re(A_0)$	$Im(A_0)$
1	2.6(97)e-08	0	3.8(33)e-08	0
2	4.8(17)e-07	0	2.1(15)e-07	0
3	-2.0(21)e-09	1.1(11)e-11	4.3(74)e-10	2.4(41)e-12
4	1.35(70)e-08	-4.4(23)e-11	1.6(33)e-09	5(11)e-12
5	-1.2(82)e-10	-6(43)e-13	4.7(29)e-10	2.4(15)e-12
6	-1.41(66)e-08	-8.5(40)e-11	-1.27(29)e-08	-7.6(18)e-11
7	7.0(22)e-11	1.18(36)e-13	8.11(75)e-11	1.36(13)e-13
8	-4.83(78)e-10	-2.35(38)e-12	-4.41(38)e-10	-2.15(19)e-12
9	-4.9(25)e-14	-3.2(16)e-13	9(10)e-15	-6.0(67)e-13
10	-2(17)e-12	0.6(40)e-13	1.46(68)e-11	-3.5(16)e-13
Total	5.1(16)e-07	-5.8(41)e-11	2.4(16)e-07	-6.9(22)e-11

Table D.2: $K \to \pi\pi(I = 0)$ decay amplitude. All numbers are in units of GeV. The contribution from each $\overline{\text{MS}}$ weak operator Q_i is listed as well as the final A_0 result. The results using wall-source-wall-sink propagators and those using all-to-all propagators are both measured on 200 configurations from the 16nt32 ensemble as in Ref [2]

Appendix E

Additional Tables and Figures for the 16nt32 and 24nt32 Ensembles

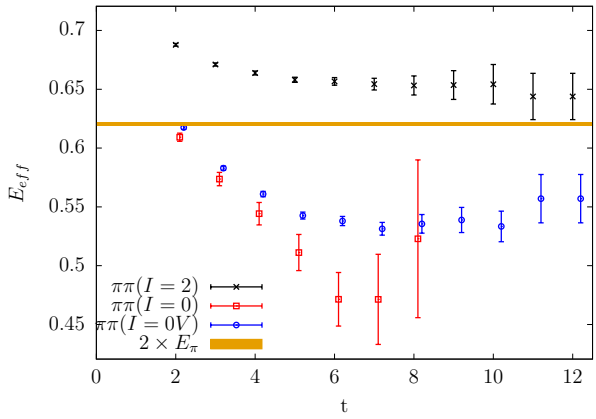

1 G-parity twist

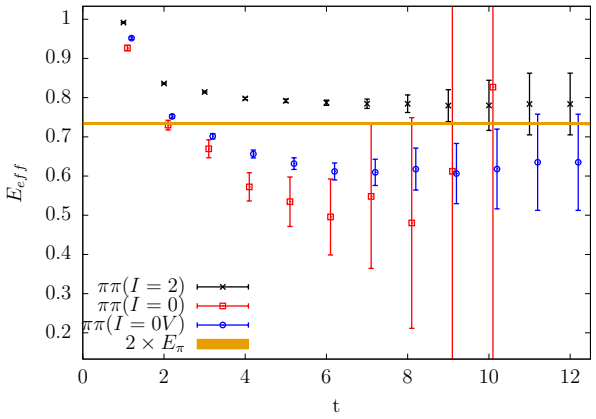

2 G-parity twists

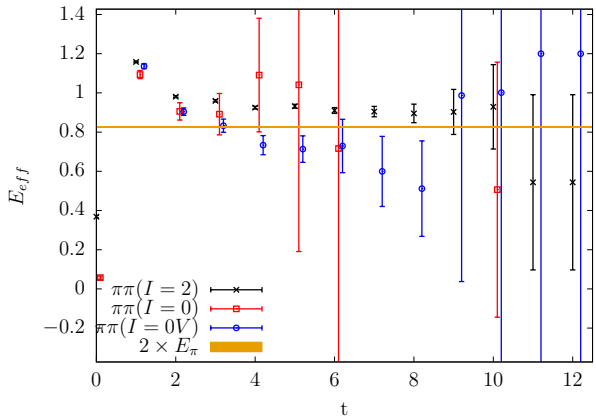

3 G-parity twists

Figure E.1: $\pi\pi$ effective energy plot for states with isospin two(I=2), isospin zero (I=0), isospin zero without vacuum graph(I=0V), and twice the single pion energy.

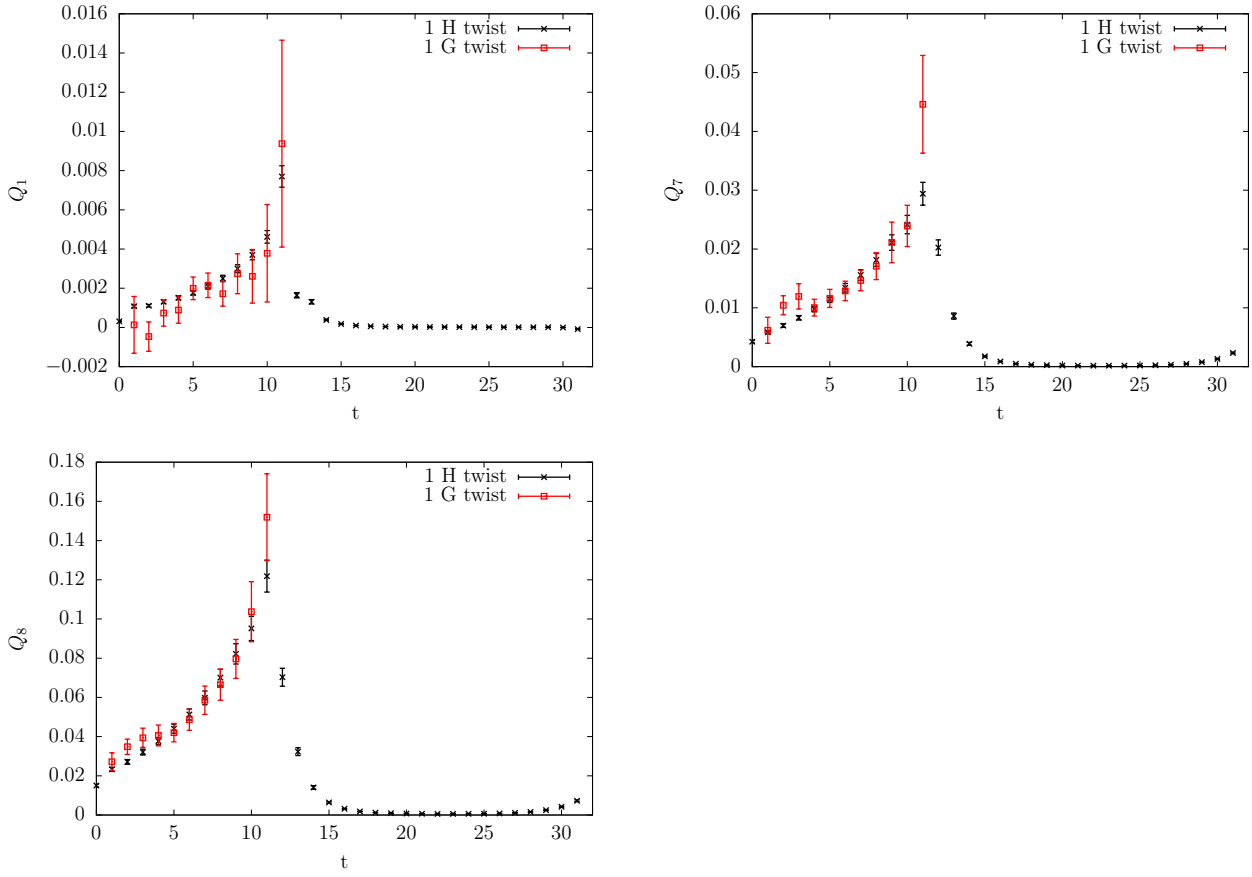

Figure E.2: $K \to \pi\pi(I=2)$ matrix elements $\langle K(t=12)|Q_i(t)|\pi\pi_{I=2}(t=0)\rangle$ (i=1,7,8), the kaon and pipi states are normalized to unity. G-parity boundary conditions and H-boundary conditions are used in one spatial direction. The G-parity correlation functions are only evaluated for $0 < t < 12$.

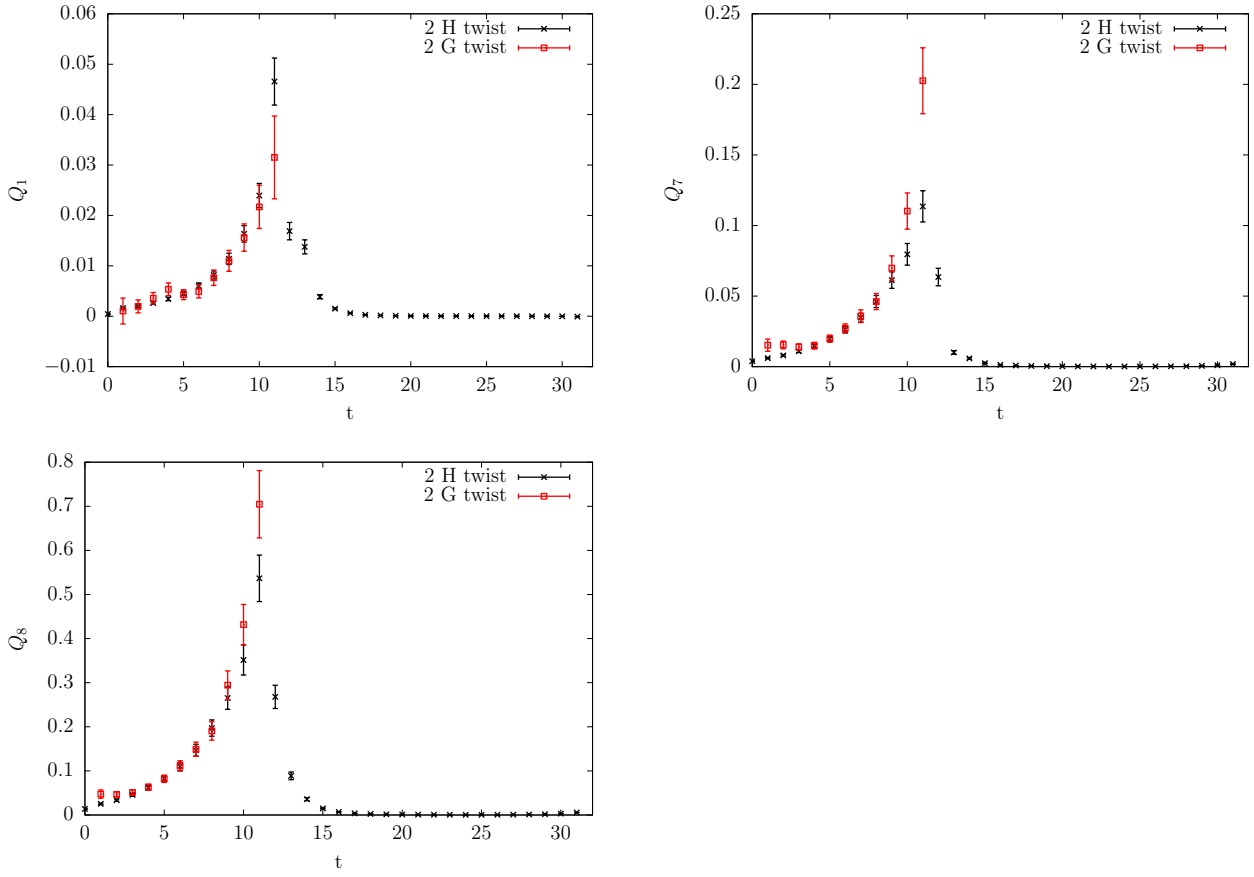

Figure E.3: $K \to \pi\pi(I=2)$ matrix elements $\langle K(t=12)|Q_i(t)|\pi\pi_{I=2}(t=0)\rangle$ (i=1,7,8), the kaon and pipi states are normalized to unity. G-parity boundary conditions and H-boundary conditions are used in two spatial directions. The G-parity correlation functions are only evaluated for $0 < t < 12$.

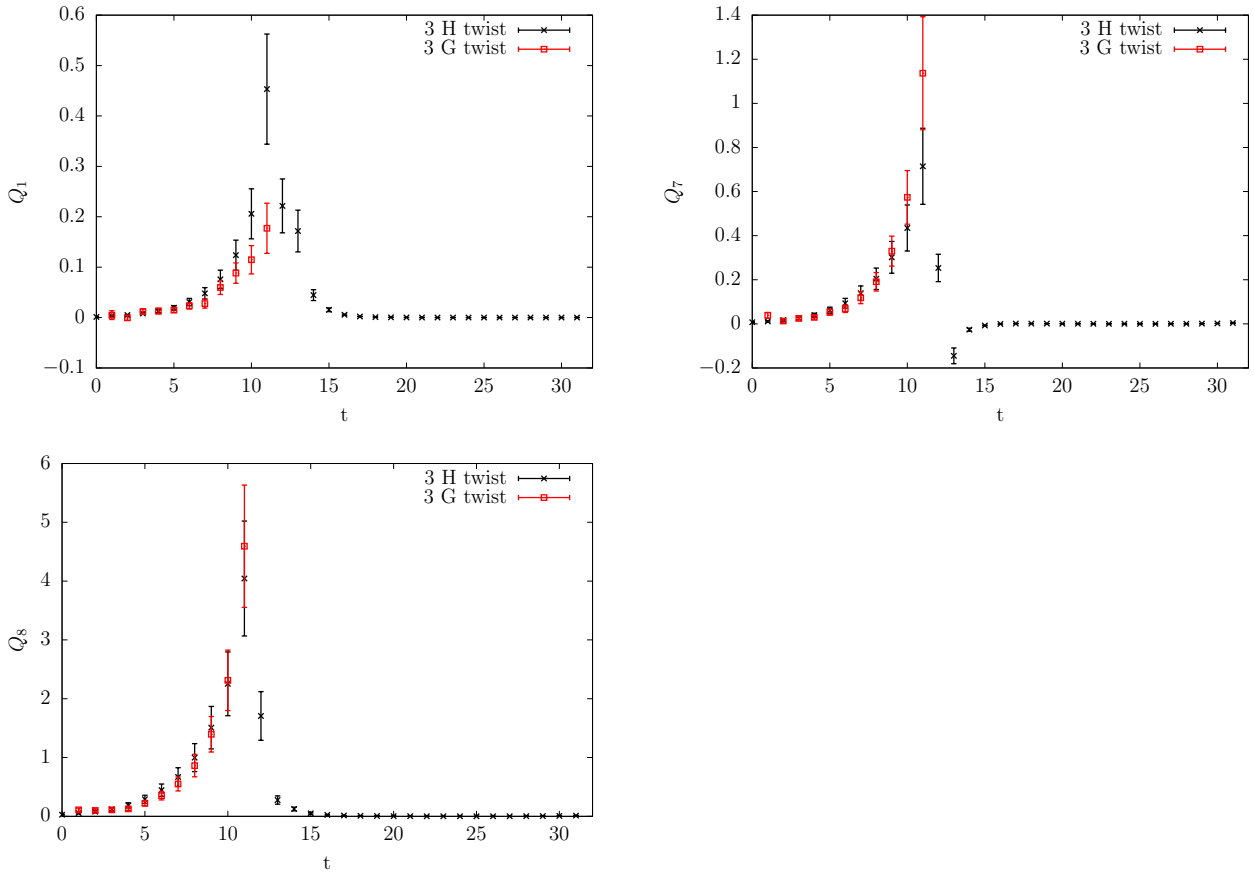

Figure E.4: $K \to \pi\pi(I=2)$ matrix elements $\langle K(t=12)|Q_i(t)|\pi\pi_{I=2}(t=0)\rangle$ (i=1,7,8), the kaon and pipi states are normalized to unity. G-parity boundary conditions and H-boundary conditions are used in three spatial directions. G-parity correlation functions are only evaluated for $0 < t < 12$.

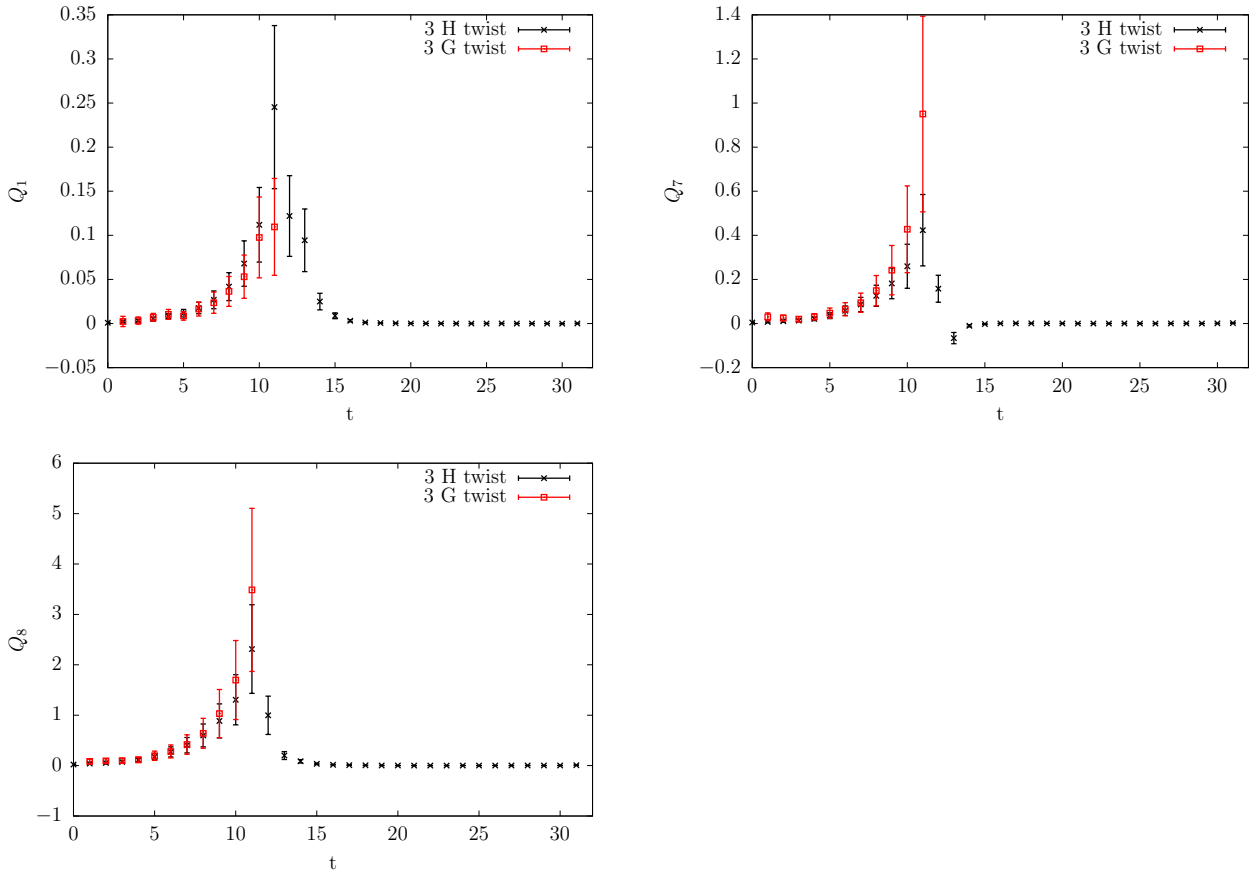

Figure E.5: $K \to \pi\pi(I=2)$ matrix elements $\langle K(t=12)|Q_i(t)|\pi\pi_{I=2}(t=0)\rangle$ (i=1,7,8) using Möbius DWF. The kaon and pipi states are normalized to unity. G-parity boundary conditions and H-boundary conditions are used in three spatial directions. The G-parity correlation functions are only evaluated for $0 < t < 12$.

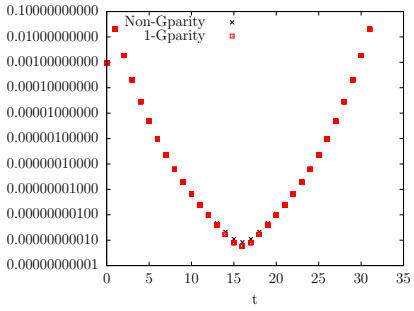

Figure E.6: Single pion correlation function on 16nt32 free field lattice

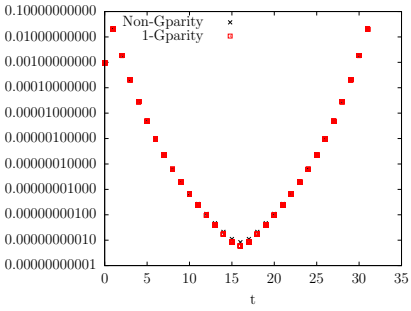

Figure E.7: Single kaon correlation function on 16nt32 free field lattice

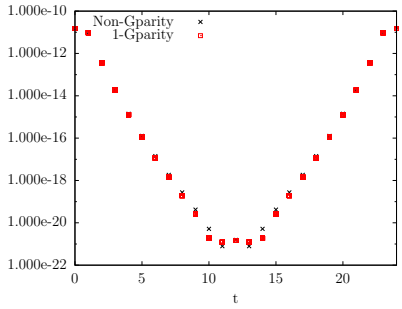

Figure E.8: pi-pi, 'Cross' graph on 16nt32 free field lattice

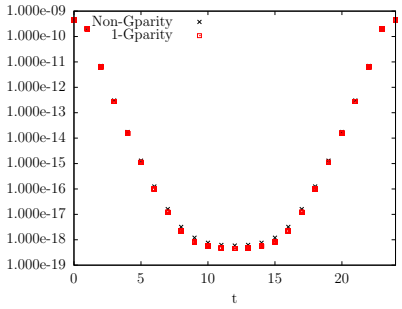

Figure E.9: pi-pi, 'Direct' graph on 16nt32 free field lattice

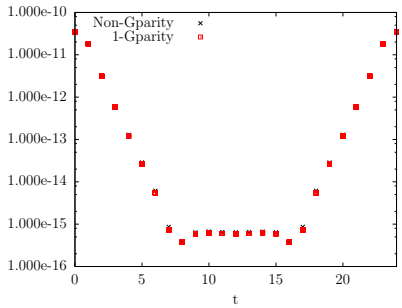

Figure E.10: pi-pi, 'Rectangle' graph on 16nt32 free field lattice

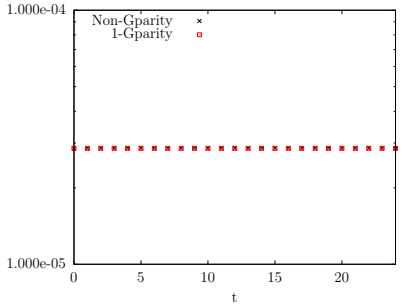

Figure E.11: pi-pi, Vaccum bubble (one of the two disconnected pieces in 'Vacuum' graph) on 16nt32 free field lattice

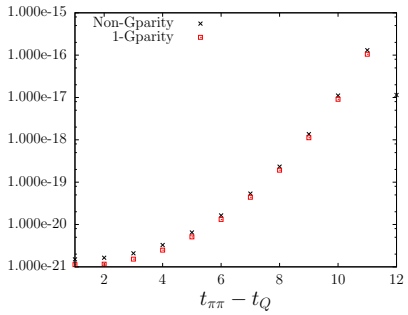

Figure E.12: Q1 in $K \to \pi\pi$(I=0), on 16nt32 free field lattice

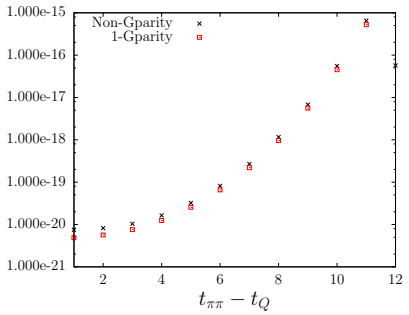

Figure E.13: Q2 in $K \to \pi\pi$(I=0), on 16nt32 free field lattice

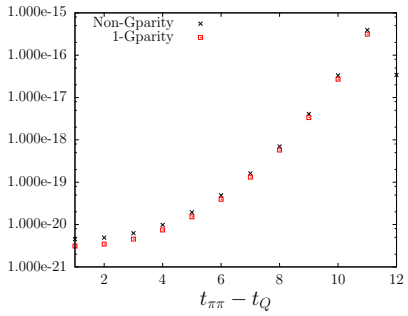

Figure E.14: Q3 in $K \to \pi\pi$(I=0), on 16nt32 free field lattice

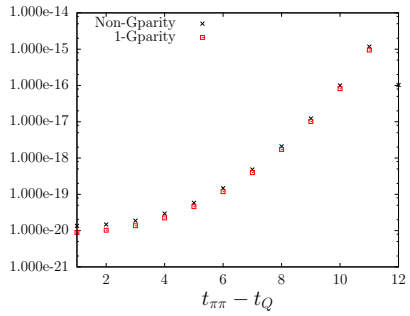

Figure E.15: Q4 in $K \to \pi\pi$(I=0), on 16nt32 free field lattice

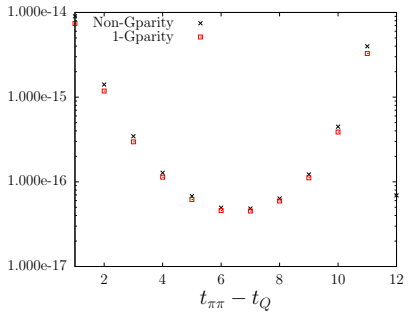

Figure E.16: Q5 in $K \to \pi\pi$(I=0), on 16nt32 free field lattice

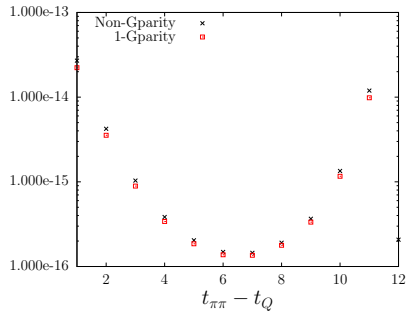

Figure E.17: Q6 in $K \to \pi\pi$(I=0), on 16nt32 free field lattice

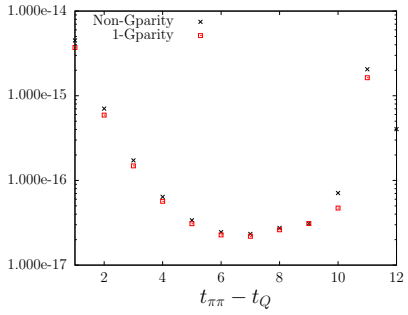

Figure E.18: Q7 in $K \to \pi\pi$(I=0), on 16nt32 free field lattice

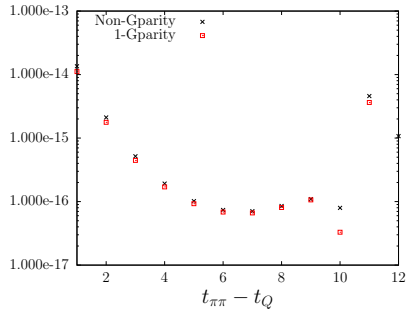

Figure E.19: Q8 in $K \to \pi\pi$(I=0), on 16nt32 free field lattice

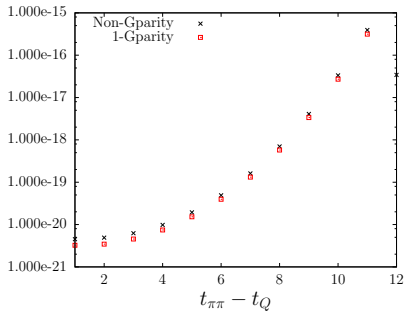

Figure E.20: Q9 in $K \to \pi\pi$(I=0), on 16nt32 free field lattice

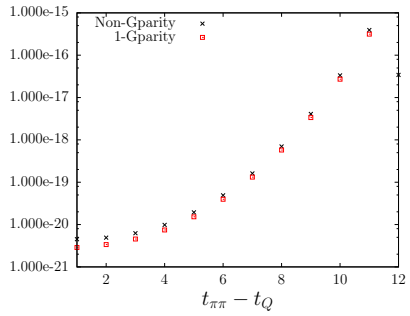

Figure E.21: Q10 in $K \to \pi\pi$(I=0), on 16nt32 free field lattice

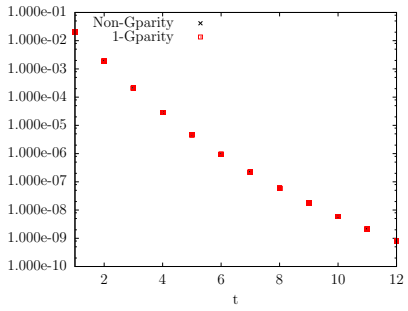

Figure E.22: Single pion correlation function on 24nt32 free field lattice

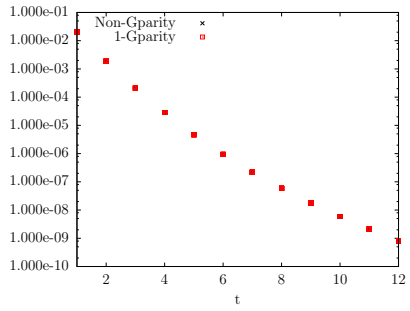

Figure E.23: Single kaon correlation function on 24nt32 free field lattice

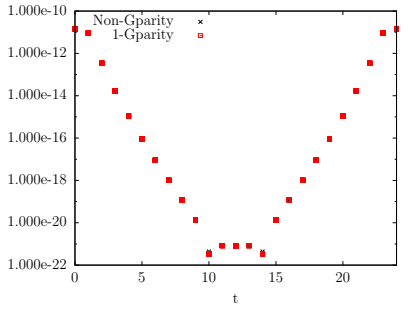

Figure E.24: pi-pi, 'Cross' graph on 24nt32 free field lattice

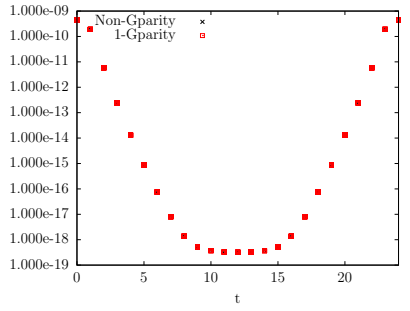

Figure E.25: pi-pi, 'Direct' graph on 24nt32 free field lattice

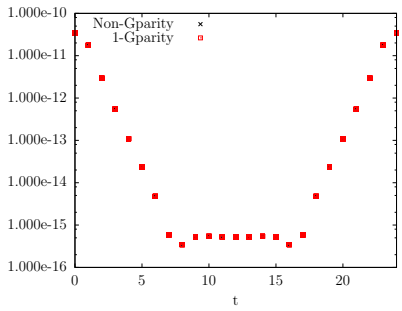

Figure E.26: pi-pi, 'Rectangle' graph on 24nt32 free field lattice

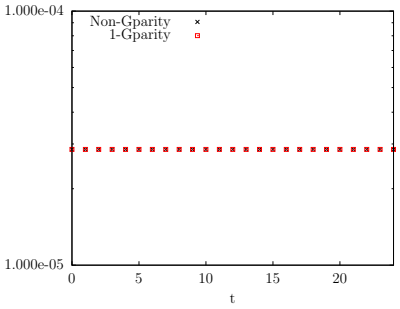

Figure E.27: pi-pi, Vaccum bubble (one of the two disconnected pieces in 'Vacuum' graph) on 24nt32 free field lattice

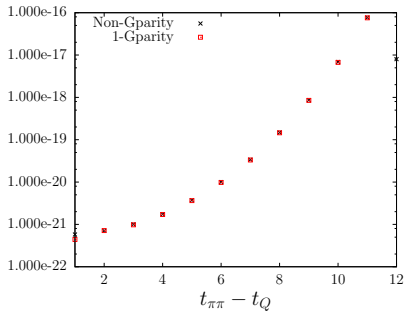

Figure E.28: Q1 in $K \to \pi\pi$(I=0), on 24nt32 free field lattice

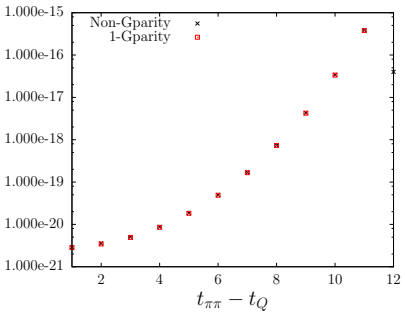

Figure E.29: Q2 in $K \to \pi\pi$(I=0), on 24nt32 free field lattice

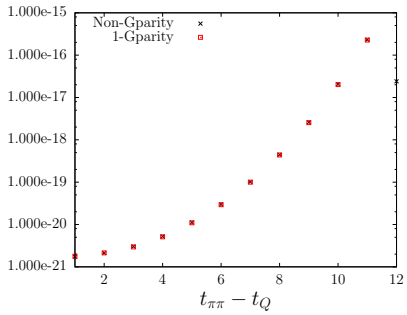

Figure E.30: Q3 in $K \to \pi\pi$(I=0), on 24nt32 free field lattice

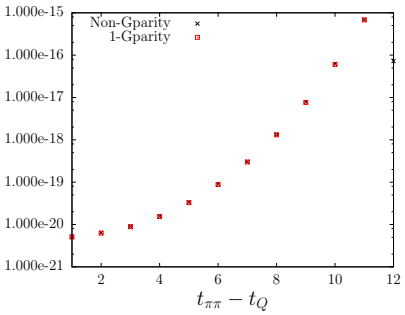

Figure E.31: Q4 in $K \to \pi\pi$(I=0), on 24nt32 free field lattice

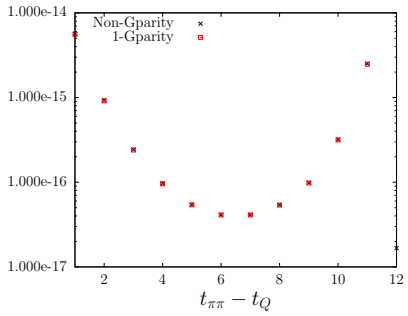

Figure E.32: Q5 in $K \to \pi\pi$(I=0), on 24nt32 free field lattice

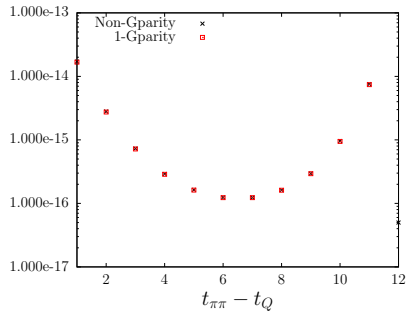

Figure E.33: Q6 in $K \to \pi\pi$(I=0), on 24nt32 free field lattice

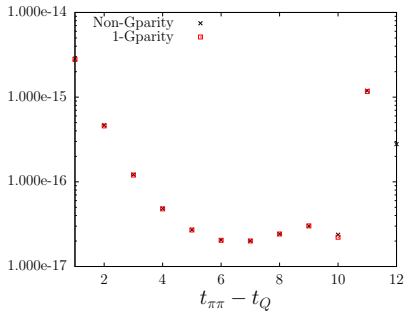

Figure E.34: Q7 in $K \to \pi\pi$(I=0), on 24nt32 free field lattice

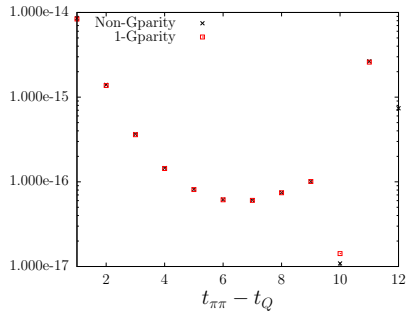

Figure E.35: Q8 in $K \to \pi\pi$(I=0), on 24nt32 free field lattice

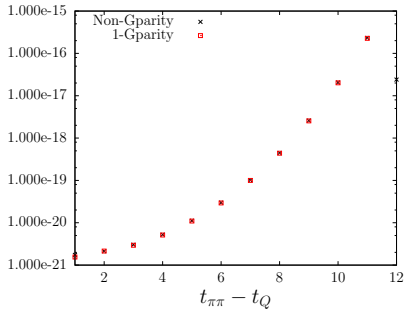

Figure E.36: Q9 in $K \to \pi\pi$(I=0), on 24nt32 free field lattice

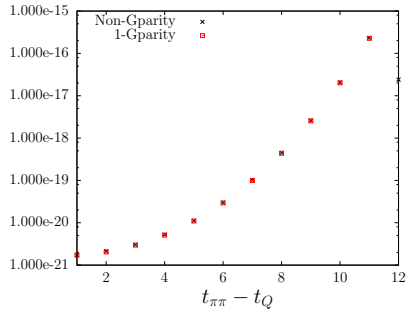

Figure E.37: Q10 in $K \to \pi\pi$(I=0), on 24nt32 free field lattice

Appendix F

Additional Tables and Figures for the 32nt64 Ensemble

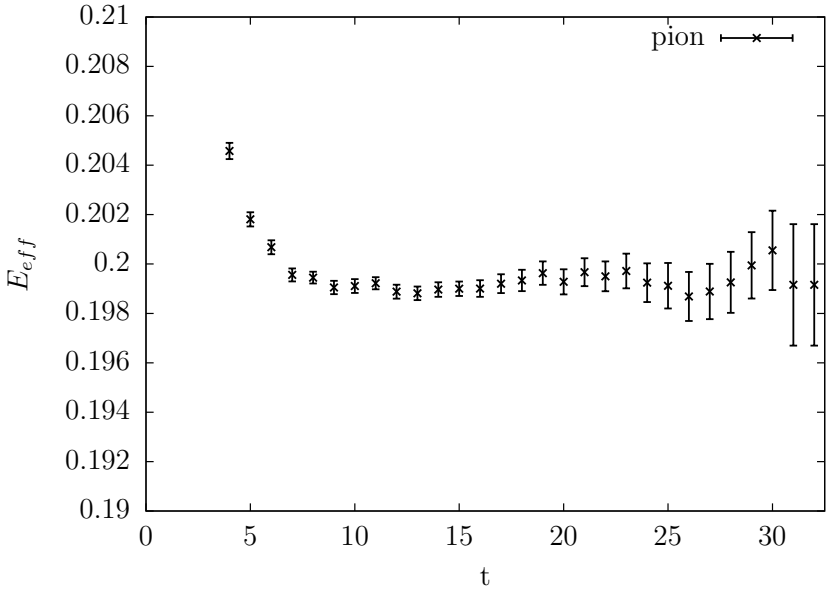

Figure F.1: pion effective energy plot on 32nt64 ensemble.

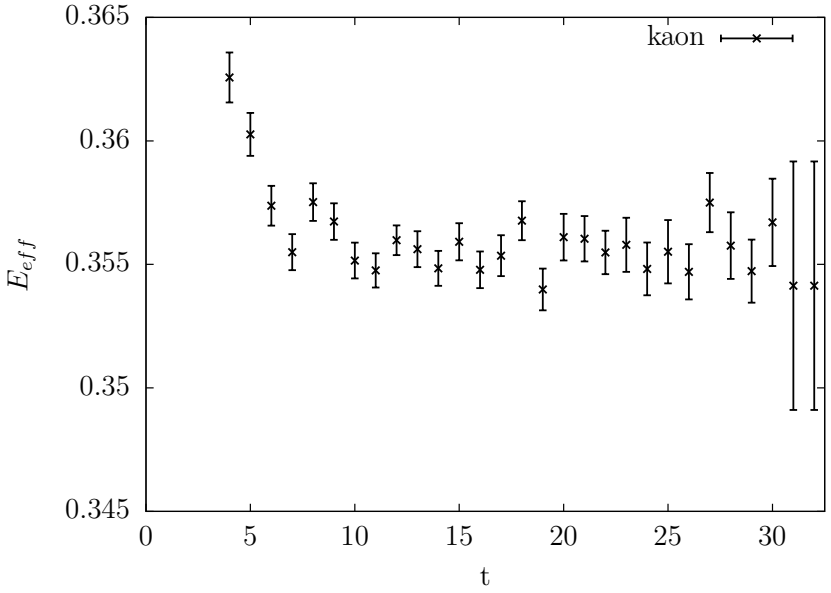

Figure F.2: kaon effective energy plot on 32nt64 ensemble.

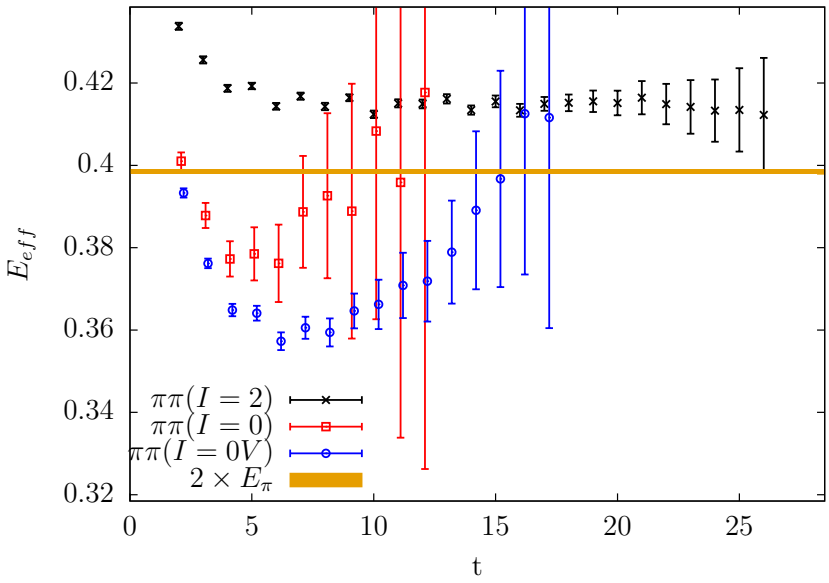

Figure F.3: $\pi\pi$ effective energy plot for states with isospin two(I=2), isospin zero (I=0), isospin zero without vacuum graph(I=0V), and twice the single pion energy.

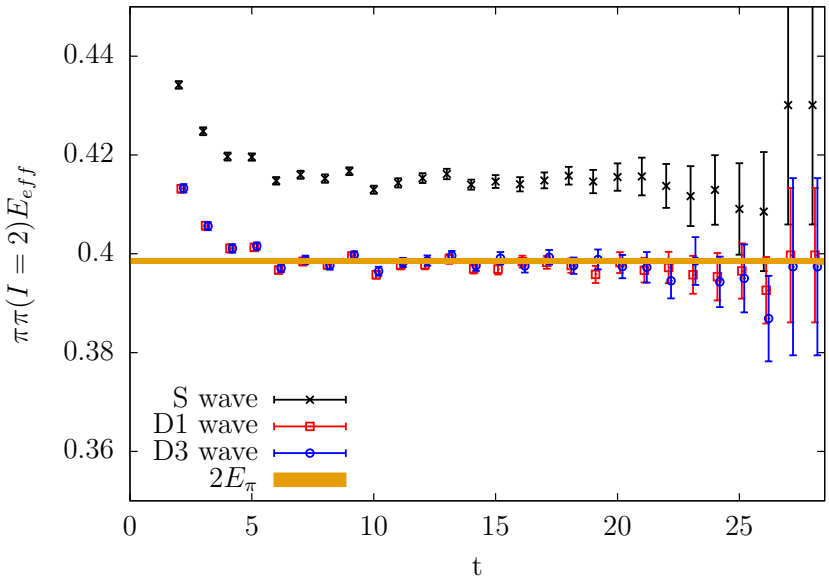

Figure F.4: $\pi\pi(I=2)$ effective energy for $\pi\pi$ states in the A_1 (s-wave) and two T_2 (D1 and D3) representations of the cubic group. For the s-wave case, $E_{\pi\pi}-2E_\pi = 0.0171 \pm 0.0006$ while the two T_2 representations show no effects of interaction, $E_{\pi\pi}-2E_\pi = -0.0005 \pm 0.0006$ and 0.0001 ± 0.0005 respectively.

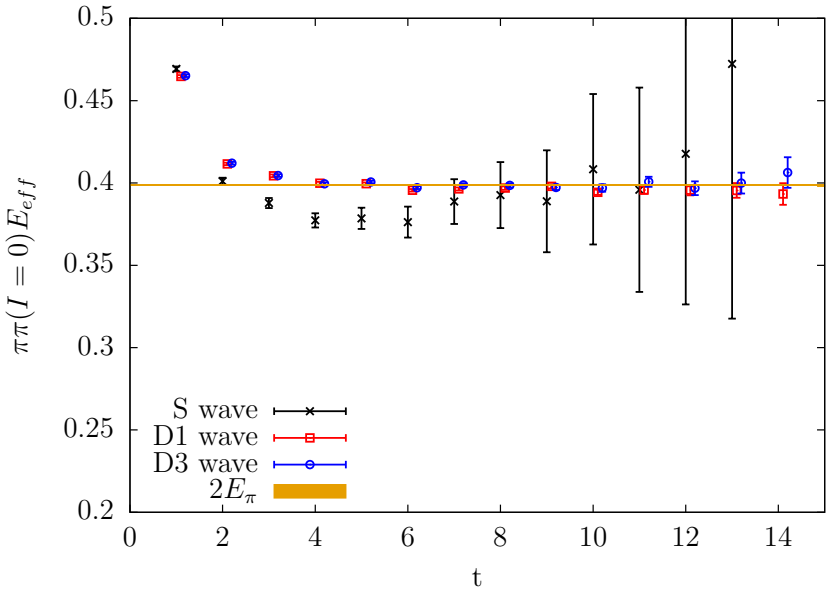

Figure F.5: $\pi\pi(I=0)$ effective energy for $\pi\pi$ states in the A_1 (s-wave) and two T_2 (D1 and D3) representations of the cubic group. For the s-wave case, $E_{\pi\pi} - 2E_\pi = -0.0371 \pm 0.0075$ while the two T_2 representations show no effects of interaction, $E_{\pi\pi} - 2E_\pi = -0.0019 \pm 0.0006$ and -0.0005 ± 0.0007 respectively.

i	bin size = 1	bin size = 2	bin size = 4	bin size = 8
1	-3.850e-03 ± 1.163e-03	-3.696e-03 ± 1.032e-03	-3.749e-03 ± 1.003e-03	-3.665e-03 ± 9.262e-04
2	3.312e-03 ± 1.227e-03	3.197e-03 ± 1.217e-03	3.284e-03 ± 1.237e-03	2.633e-03 ± 1.217e-03
3	-2.130e-03 ± 2.994e-03	-1.543e-03 ± 2.808e-03	-1.664e-03 ± 2.914e-03	-2.308e-03 ± 2.825e-03
4	4.775e-03 ± 3.170e-03	5.173e-03 ± 3.028e-03	4.833e-03 ± 2.971e-03	4.101e-03 ± 2.985e-03
5	-1.073e-02 ± 2.612e-03	-1.063e-02 ± 2.322e-03	-1.114e-02 ± 2.203e-03	-1.171e-02 ± 2.294e-03
6	-2.439e-02 ± 5.152e-03	-2.460e-02 ± 5.314e-03	-2.456e-02 ± 5.033e-03	-2.458e-02 ± 5.225e-03
7	2.210e-02 ± 1.861e-03	2.231e-02 ± 1.960e-03	2.240e-02 ± 1.839e-03	2.279e-02 ± 2.053e-03
8	7.951e-02 ± 4.964e-03	8.022e-02 ± 5.404e-03	8.043e-02 ± 5.986e-03	7.985e-02 ± 5.903e-03
9	-4.817e-03 ± 1.862e-03	-4.795e-03 ± 1.709e-03	-4.758e-03 ± 1.590e-03	-4.394e-03 ± 1.439e-03
10	2.545e-03 ± 1.743e-03	2.617e-03 ± 1.700e-03	2.675e-03 ± 1.649e-03	2.657e-03 ± 1.411e-03

Table F.1: $M_i^{1/2,lat}$ results with different bin sizes. The matrix elements are measured on every 4th configuration, so the effective separations for bin size = 1,2,3,4 are 4,8,12,16 respectively. The results we obtained by combining the $K - \pi\pi$ separations, $T_{\pi\pi} - T_K = 10, 12, ..., 18$, and involve 172 measurements.

i	$y_i^{\overline{\text{MS}}}(\mu, 3f)$	$y_i^{\overline{\text{MS}}}(\mu, 4f)$
1	0	0
2	0	0
3	0.0287243	0.0340292
4	-0.0573151	-0.0732297
5	0.00500764	0.0103125
6	-0.0889116	-0.104826
7	-0.00023089	-0.00017299
8	0.00105509	0.00105509
9	-0.0114666	-0.0114087
10	0.00423782	0.00423782

Table F.2: Wilson coefficients in the (NLO) $\overline{\text{MS}}$ scheme, at energy scale $\mu = 1.3$ GeV, with charm integrated out (3f) and not integrated out (4f). These numbers were provided by Christoph Lehner.

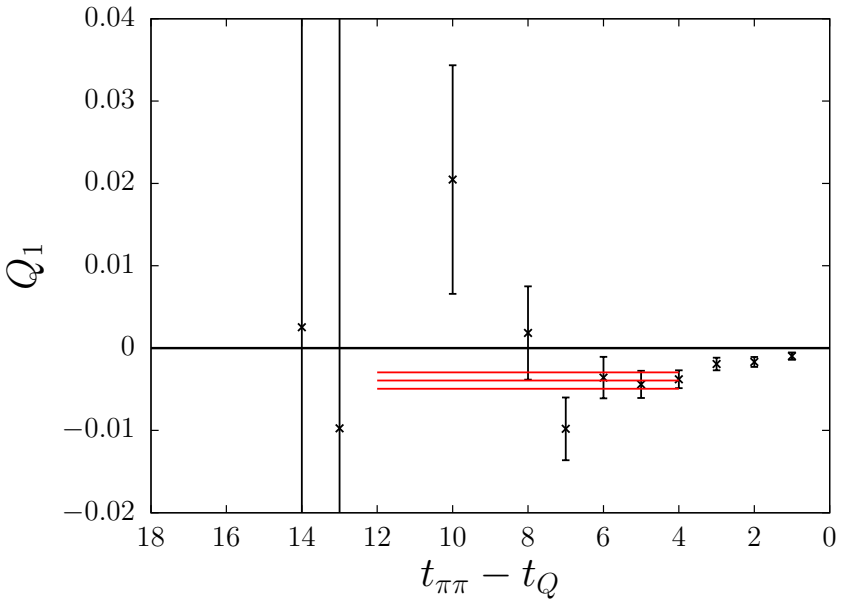

Figure F.6: The error weighted average of the $\langle \pi\pi(I=0)|Q_1|K\rangle$ correlation function, measured on the 32nt64 G-parity ensemble as a function of $t_{\pi\pi} - t_Q$. These used the 3-point function data with a kaon to pipi separations of 10, 12, ..., 18.

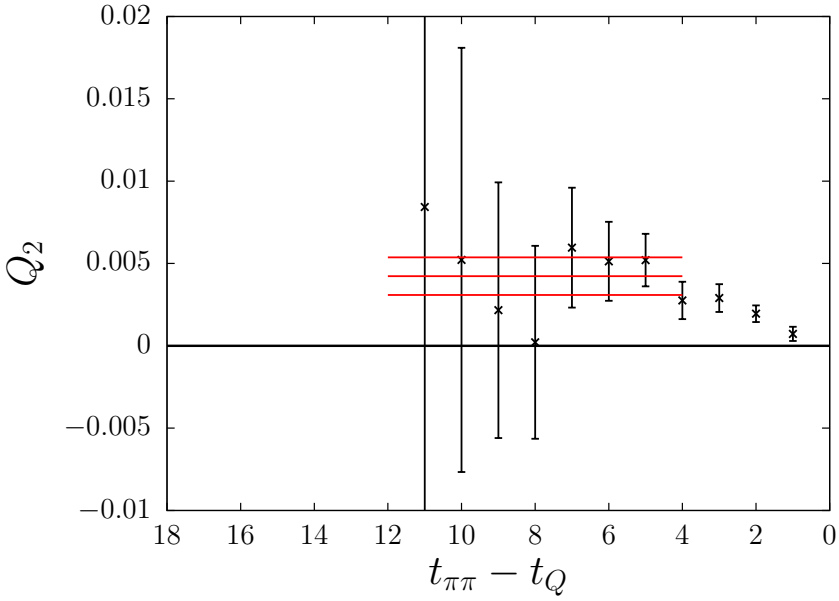

Figure F.7: The error weighted average of the $\langle \pi\pi(I=0)|Q_2|K\rangle$ correlation function, measured on the 32nt64 G-parity ensemble as a function of $t_{\pi\pi} - t_Q$. These used the 3-point function data with a kaon to pipi separations of 10, 12, ..., 18.

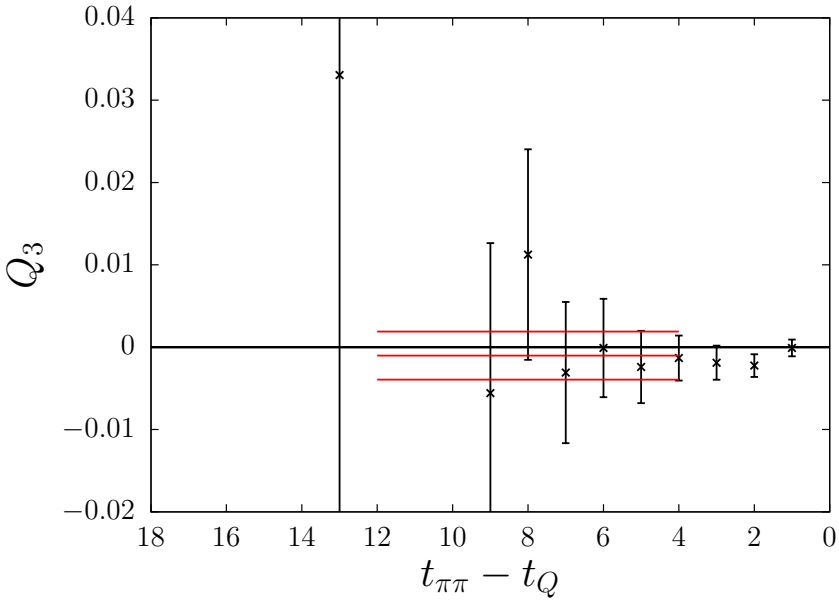

Figure F.8: The error weighted average of the $\langle \pi\pi(I=0)|Q_3|K\rangle$ correlation function, measured on the 32nt64 G-parity ensemble as a function of $t_{\pi\pi} - t_Q$. These used the 3-point function data with a kaon to pipi separations of 10, 12, ..., 18.

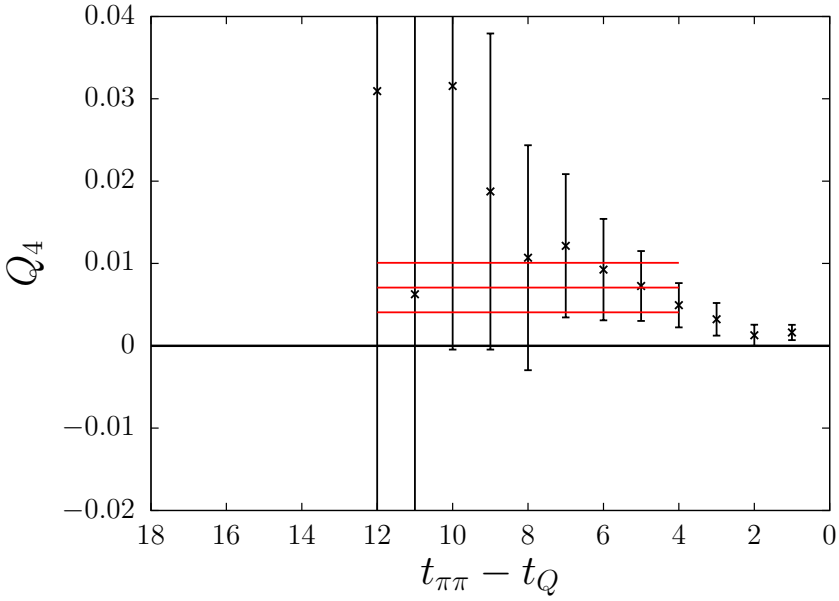

Figure F.9: The error weighted average of the $\langle \pi\pi(I=0)|Q_4|K\rangle$ correlation function, measured on the 32nt64 G-parity ensemble as a function of $t_{\pi\pi} - t_Q$. These used the 3-point function data with a kaon to pipi separations of 10, 12, ..., 18.

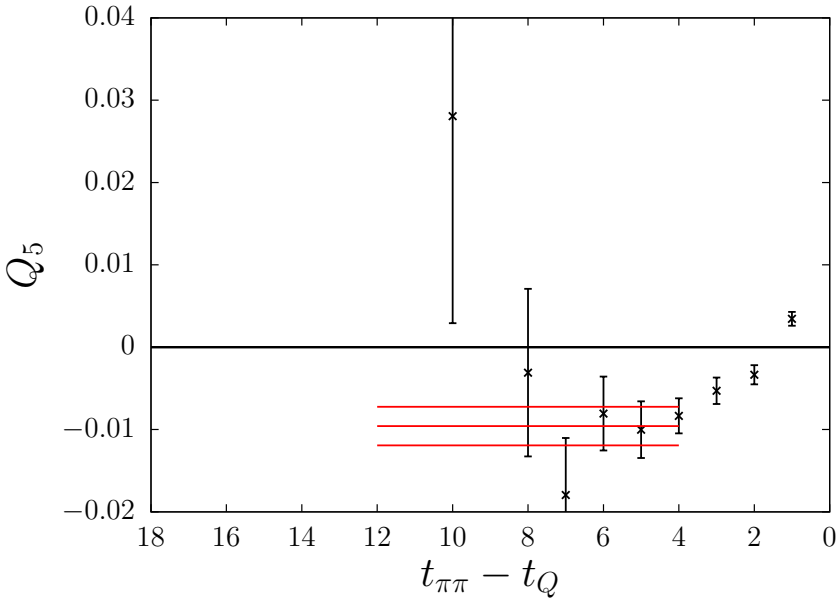

Figure F.10: The error weighted average of the $\langle \pi\pi(I=0)|Q_5|K\rangle$ correlation function, measured on the 32nt64 G-parity ensemble as a function of $t_{\pi\pi} - t_Q$. These used the 3-point function data with a kaon to pipi separations of 10, 12, ..., 18.

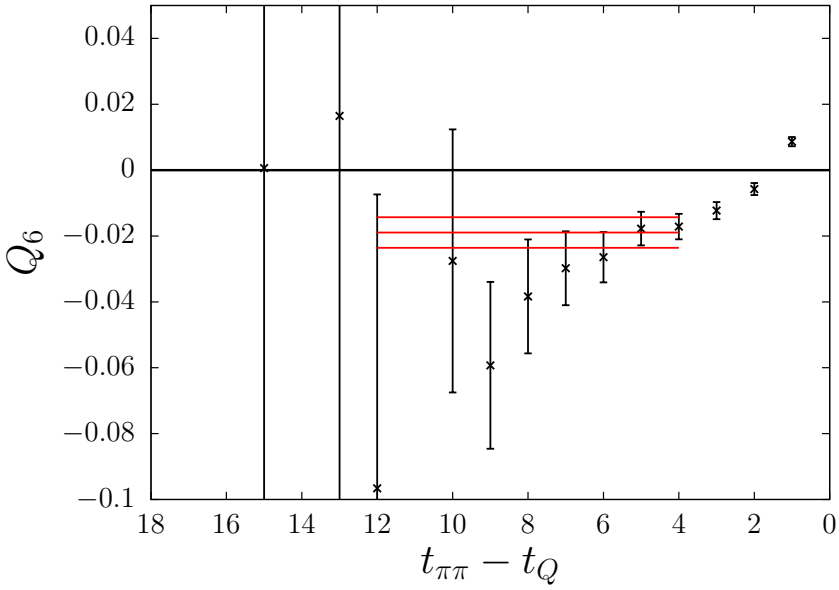

Figure F.11: The error weighted average of the $\langle \pi\pi(I = 0)|Q_6|K\rangle$ correlation function, measured on the 32nt64 G-parity ensemble as a function of $t_{\pi\pi} - t_Q$. These used the 3-point function data with a kaon to pipi separations of 10, 12, ..., 18.

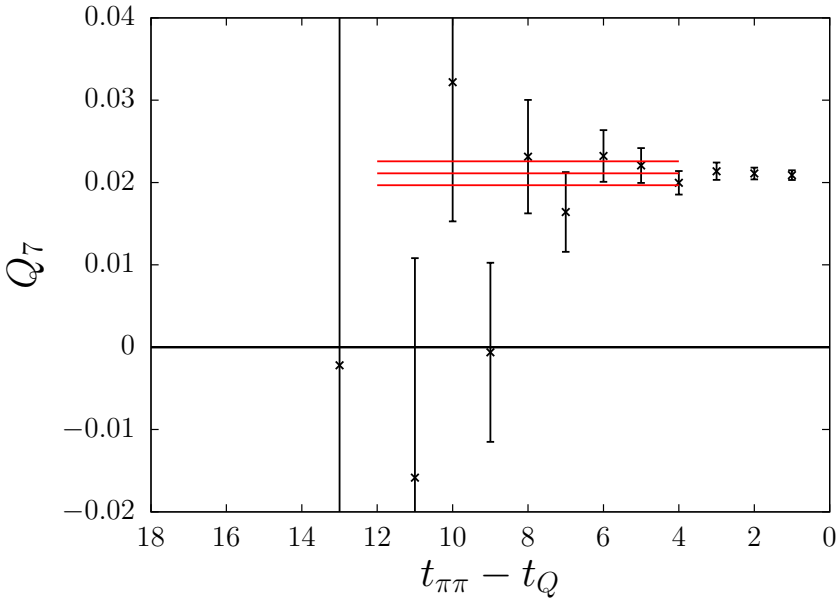

Figure F.12: The error weighted average of the $\langle \pi\pi(I = 0)|Q_7|K\rangle$ correlation function, measured on the 32nt64 G-parity ensemble as a function of $t_{\pi\pi} - t_Q$. These used the 3-point function data with a kaon to pipi separations of 10, 12, ..., 18.

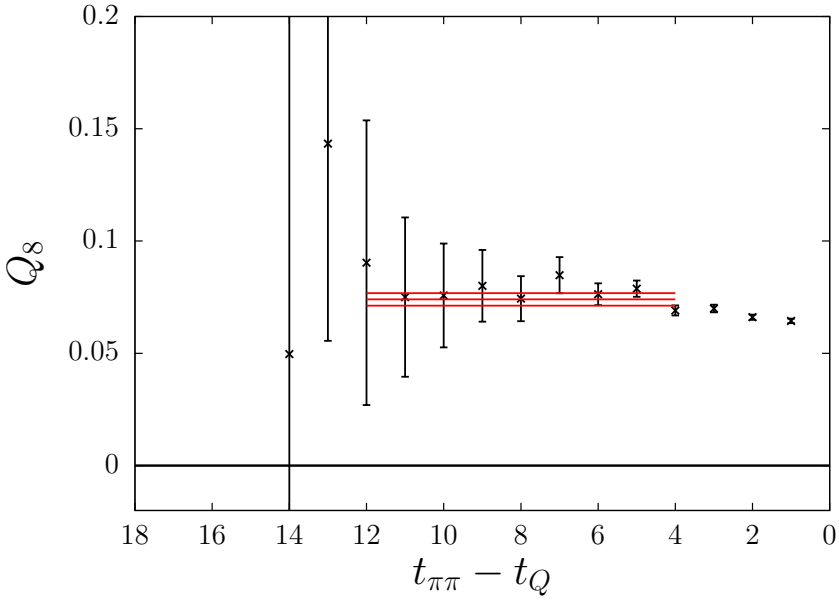

Figure F.13: The error weighted average of the $\langle \pi\pi(I = 0)|Q_8|K\rangle$ correlation function, measured on the 32nt64 G-parity ensemble as a function of $t_{\pi\pi} - t_Q$. These used the 3-point function data with a kaon to pipi separations of 10, 12, ..., 18.

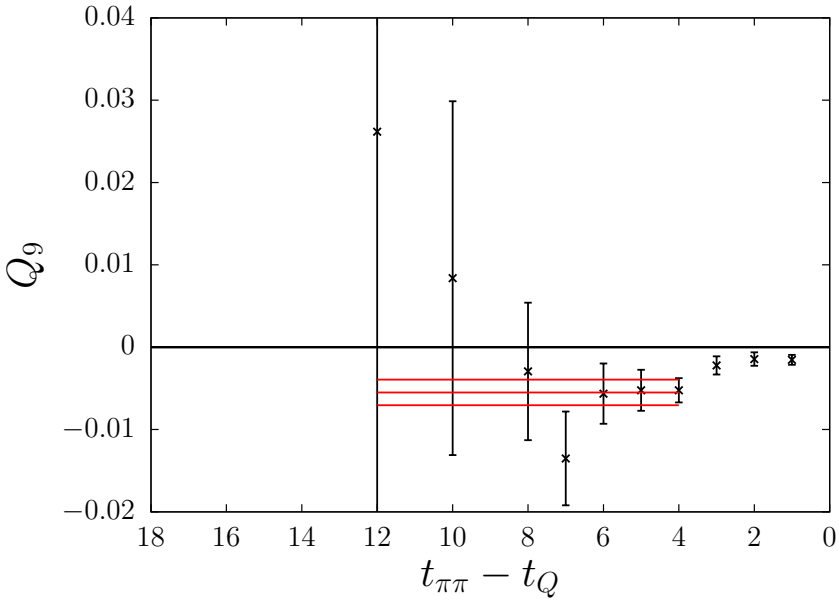

Figure F.14: The error weighted average of the $\langle \pi\pi(I = 0)|Q_9|K\rangle$ correlation function, measured on the 32nt64 G-parity ensemble as a function of $t_{\pi\pi} - t_Q$. These used the 3-point function data with a kaon to pipi separations of 10, 12, ..., 18.

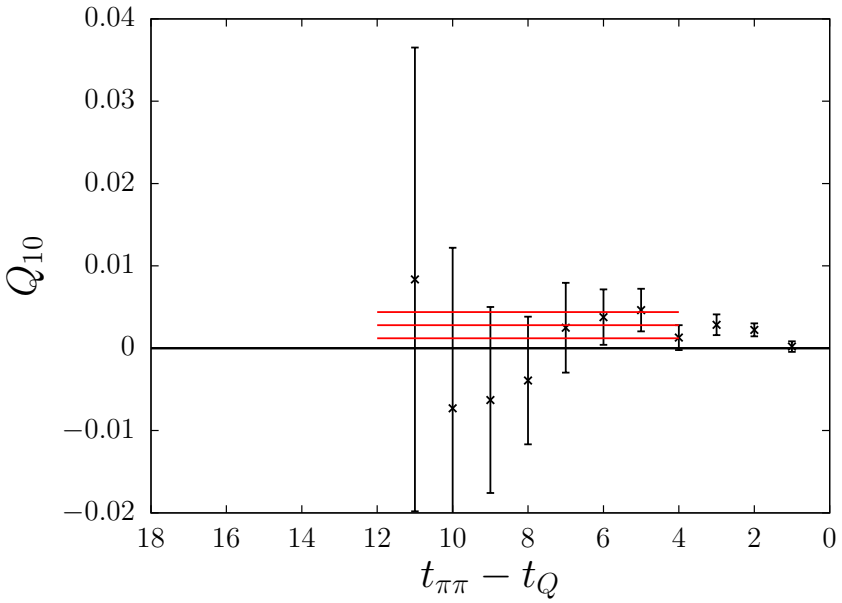

Figure F.15: The error weighted average of the $\langle \pi\pi(I=0)|Q_{10}|K\rangle$ correlation function, measured on the 32nt64 G-parity ensemble as a function of $t_{\pi\pi} - t_Q$. These used the 3-point function data with a kaon to pipi separations of 10, 12, ..., 18.

i	$M_i^{1/2,lat}$ with $m_K^{(0)}$	$M_i^{1/2,lat}$ with $m_K^{(1)}$	$M(m_K^{(1)}) - M(m_K^{(0)})$	$\frac{M(m_K^{(1)}) - M(m_K^{(0)})}{M(m_K^{(0)})}$
1	-9.640e-04 ± 3.082e-03	-9.062e-04 ± 3.214e-03	5.781e-05 ± 2.304e-04	-5.996e-02
2	2.917e-03 ± 2.928e-03	3.126e-03 ± 3.053e-03	2.092e-04 ± 1.902e-04	7.170e-02
3	1.048e-03 ± 6.185e-03	1.484e-03 ± 6.442e-03	4.361e-04 ± 4.841e-04	4.163e-01
4	7.764e-03 ± 6.517e-03	8.384e-03 ± 6.849e-03	6.198e-04 ± 5.124e-04	7.983e-02
5	-7.677e-03 ± 5.111e-03	-7.385e-03 ± 5.313e-03	2.916e-04 ± 4.098e-04	-3.798e-02
6	-2.163e-02 ± 8.827e-03	-2.167e-02 ± 9.044e-03	-3.364e-05 ± 6.148e-04	1.555e-03
7	2.611e-02 ± 4.539e-03	2.589e-02 ± 4.724e-03	-2.230e-04 ± 3.098e-04	-8.539e-03
8	7.641e-02 ± 6.779e-03	7.574e-02 ± 6.942e-03	-6.737e-04 ± 3.927e-04	-8.816e-03
9	-3.593e-03 ± 4.106e-03	-3.784e-03 ± 4.374e-03	-1.906e-04 ± 3.636e-04	5.303e-02
10	1.379e-03 ± 3.662e-03	1.407e-03 ± 3.880e-03	2.811e-05 ± 3.038e-04	2.038e-02

Table F.3: $M_i^{1/2,lat}$ results for two different valence strange quark masses $m_s = 0.045$ (superscript (0)) and $m_s = 0.0495$ (superscript (1)). Using data from $K - \pi\pi$ separations of 10, 12, and 14, and were analysed on 69 configurations.

t	normalized expression 6.13	normalized expression 6.14	full correlator
1	9.2305e-03 ± 2.0891e-03	6.8849e-03 ± 1.8013e-03	4.0621e-02 ± 1.7811e-01
2	6.6341e-03 ± 1.5006e-03	6.3605e-03 ± 1.1376e-03	-1.2313e-02 ± 9.2606e-02
3	5.9011e-03 ± 1.0619e-03	2.3395e-03 ± 8.4813e-04	-4.1902e-02 ± 5.1461e-02
4	4.0494e-03 ± 7.5205e-04	1.8216e-03 ± 6.8875e-04	-1.7756e-03 ± 3.4008e-02
5	2.7282e-03 ± 6.0880e-04	2.1378e-03 ± 5.8850e-04	-4.9095e-02 ± 2.2007e-02
6	2.9705e-03 ± 5.3786e-04	2.6533e-03 ± 4.7434e-04	1.0519e-02 ± 1.5950e-02
7	1.2709e-03 ± 4.5540e-04	2.2297e-03 ± 4.4524e-04	-1.2714e-02 ± 9.8130e-03
8	-1.1525e-03 ± 4.0391e-04	1.6743e-03 ± 4.2331e-04	-1.8283e-02 ± 6.5643e-03
9	-1.6596e-03 ± 3.1749e-04	9.6151e-04 ± 3.5184e-04	-7.3171e-03 ± 4.6764e-03
10	-1.4256e-03 ± 3.7969e-04	4.0559e-04 ± 3.7320e-04	-4.7929e-03 ± 3.3398e-03
11	-2.7597e-03 ± 4.3192e-04	-1.3549e-03± 3.8603e-04	1.1034e-02 ± 2.5307e-03

Table F.4: Comparison of the connected correlation functions that are similar to the charm contribution with the full connected correlation function, for Q_6 in $K \to \pi\pi(I = 0)$. Left two columns: contribution of the light quark, Equation 6.13 and the strange quark, Equation 6.14. Right column: $\langle \pi\pi(t = 12)|Q_6(t)|K(t = 0)\rangle$. All numbers are divided by $e^{-m_K * \Delta_{T_K - T_{\pi\pi}}}$. $\Delta_{T_K - T_{\pi\pi}} = 12$. 't' column is $\Delta_{T_{op} - T_K}$. Analysed on 172 configurations.